Department of Precision and Microsystems Engineering

Design of Non-Mixing Two-Fluid Heat Exchangers with Density-Based Topology Optimization

Kasper Bulstra

Report no	: 2023.026
Coach	: Ir. Maarten Theulings (TU Delft)
Professor	: Dr. Ir. Lise Noël (TU Delft)
Specialisation	: Mechatronic System Design (MSD)
Type of report	: Thesis Report
Date	: 12-05-2023

Delft University of Technology

1 Abstract

The main problem in density-based two-fluid optimization is the fact that the two fluids often mix in optimal designs. Therefore, state-of-the-art two-fluid heat exchanger optimization includes non-mixing constraints. However, the current non-mixing constraints can only impose a constant wall-thickness between the two fluids. Depending on the optimization problem, the forming of a wall with a variable thickness is advantageous for the heat transfer in the heat exchanger. A non-mixing constraint that can only impose a constant wall-thickness cannot further improve the heat transfer objective in such an optimization problem, since a variable wall-thickness cannot be generated. In these optimization problems, a non-mixing constraint that allows a variable wall-thickness to be formed can generate heat exchangers with a higher efficiency. In the proposed optimization method, a non-mixing constraint is provided which guarantees a pre-defined minimum wall-thickness separating the two fluids, and also allows the optimizer to locally increase the wall-thickness above the minimum wall-thickness. The advantage of the proposed non-mixing constraint is that the minimum wall-thickness can be set based on a manufacturing limit, while the optimization algorithm can vary the wall-thickness based on advantageous heat transfer.

In this report a method is proposed for the design of a two-fluid heat exchanger with density-based topology optimization. The density-based topology optimization method has two design variables to distinguish between the two fluids and solid material. The first design variable distinguishes between the fluid and solid material regions and the second design variables distinguishes between the two fluids. The non-mixing constraint relies on a two design variable method combined with a two-step filtering and projection method to generate a variable wall-thickness. The two-step filtering and projection method is applied to the second design variable to guarantee a solid material region with the minimum wall-thickness; the non-mixing region. The first design variable can be used to generate additional solid material regions that are combined with the non-mixing region to form a variable wall-thickness.

The research question is : Can a non-mixing constraint for density-based two-fluid topology optimization be created that guarantees a minimum wall-thickness and also allows for a wall-thickness larger than the minimum implemented within a finite element computational framework?

The optimization problem formulation used in this project is a heat transfer objective that is maximized with two pressure drop constraints, one for each fluid channel. The proposed non-mixing constraint is applied to a variety of 2D optimization problems where different design domains, heat exchanger configurations, materials and parameter settings are used to investigate the influence on the optimization behaviour. The results show that the non-mixing constraint guarantees a pre-defined minimum wall-thickness and also allows for a wall-thickness larger than the minimum wall-thickness. In addition, a method to determine a suitable parameter continuation scheme fine-tuned based on the parameter settings is provided. The proposed optimization method allows for two-fluid heat exchangers with identical and different fluids. A variety of material parameters is used to show the effect on the material interpolation and the optimization behaviour. Depending on the initial design and design domain, the optimization algorithm generates an optimal design with a constant wall-thickness or variable wall-thickness. Finally, to illustrate the possibilities with the proposed non-mixing constraint two 3D optimization problems are computed and one of the optimal designs is post-processed and manufactured.

Contents

2 Introduction

The introduction is subdivided into four sections. The first section gives some general information on two-fluid heat exchangers. In the second section an overview of the state of the art in two-fluid heat exchanger topology optimization is provided. The research question is formulated, based on the gap found in the state of the art. The third section elaborates on the research direction selected for this research project and the contribution of this research direction to the state of the art. The final section provides an outline of the structure of the report.

2.1. Two-Fluid Non-Mixing Heat Exchangers

A classical description of a two-fluid non-mixing heat exchanger is a volume with two inlets and two outlets, one for each fluid. The fluids in the heat exchanger can be identical or different fluids flowing into the volume with different temperatures. Depending on the application one fluid can be used to cool down or heat-up the other fluid. The fluids are separated by a solid material to prevent mixing of the fluids that does allow for heat exchange between the fluids. The performance of a two-fluid non-mixing heat exchanger can be expressed in the heat exchange or temperature change of the fluids with a limited pressure drop or power dissipation. Classical two-fluid heat exchanger can be categorized into the following three configurations: parallel-, counter- and cross-flow, see Fig. 2.2.

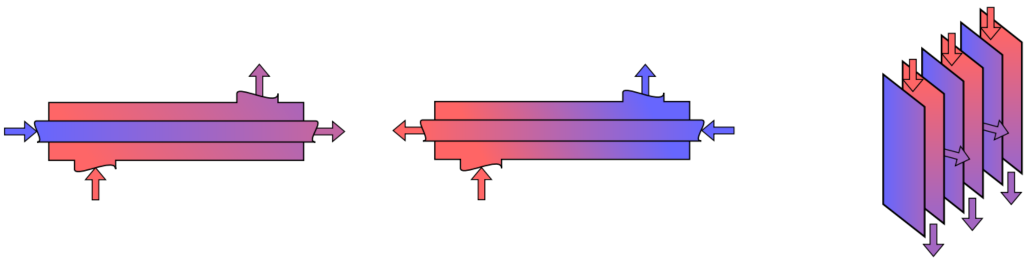

Figure 2.1: Three different basic heat exchange configurations. From left to right: parallel-flow, counter-flow and cross-flow configuration [10].

Apart from different configurations, different types of heat exchangers can be used. Three examples of heat exchanger types are: the shell and tube heat exchanger, the double pipe heat exchanger and the plate heat exchanger [16]. Fig. 2.2 shows the three types of heat exchanger configurations in the order from left to right; shell and tube, double pipe and plate heat exchanger. The shell and tube heat exchanger consists of a large tube, the shell, that is enclosing a collection of smaller tubes. The double pipe configuration consists of a larger tube with a single smaller inner tube. The plate heat exchanger has an outer shell with multiple plates inside the shell separating the two fluids, between every plate the fluids are switched. By changing the locations of the inlet and outlet the types of heat exchangers can be used in parallel-, counter- or cross-flow configuration [16].

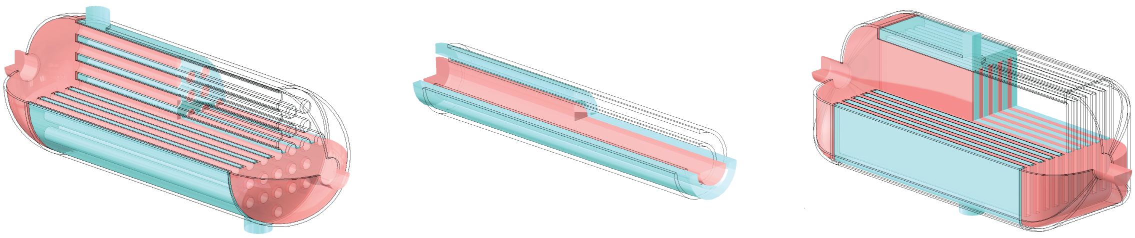

(a) Shell-and-tube two-fluid heat exchanger. (b) Double pipe two-fluid heat exchanger. (c) Plate two-fluid heat exchanger.

Figure 2.2: Conventional two-fluid heat exchanger configurations.

2.2. State of the Art

To provide an overview of the state of the art in two-fluid heat exchanger topology optimization, a selection is made based on the following criteria; the model should have two fluids and do not allow for mixing of the fluids. The state of the art is subdivided into two categories; density-based and level-set topology optimization. Fig. 2.3 shows optimal designs generated with a density-based method. A design and validation process of a two-fluid heat exchanger with topology optimization was conducted in [15]. However, the details of the optimization model are not provided in this article and the properties can therefore not be investigated.

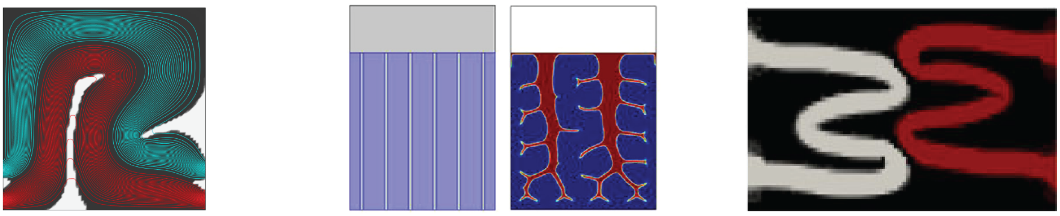

(a) Result of a 2D two-fluid heat exchanger topology optimization [14]. (b) Result of a 2D two-fluid heat exchanger topology optimization [9]. (c) Result of a 2D two-fluid heat exchanger topology optimization [18].

(d) Result of a 3D two-fluid heat exchanger topology optimization [10]. (e) Result of a 3D two-fluid heat exchanger topology optimization [11].

Figure 2.3: Optimal designs generated with density-based topology optimization.

The goal of this project is to create a non-mixing constraint that allows for a variable wall-thickness. The state of the art articles on density-based two-fluid heat exchanger topology optimization are analysed to determine if and what type of non-mixing constraints are used. An earlier two-fluid heat exchanger topology optimization approach is introduced in [14], see Fig. 2.3a. The non-mixing constraint used here penalizes the flow of one fluid in the region of the other fluid and vice-versa. However, no solid region is guaranteed between the two fluids allowing for a zero wall-thickness. The non-mixing constraint used in both [9] and [10] is a two-step filtering projection scheme guaranteeing a wall with a fixed thickness between the two-fluids, see Fig. 2.3b and 2.3d. The non-mixing constraint used in [18] has a minimum wall-thickness and allows the wall-thickness to vary, see Fig. 2.3c. The discretization method used in this article is a finite volume method (FVM). To guarantee a minimum wall-thickness, but allow for thicker walls a penalty function in the objective function is used. This function does not allow for the existence of both fluids in a cell and the two neighbouring cells. In [11] the non-mixing constraint consists of a peak-function interpolation that guarantees a wall with a fixed thickness, see Fig. 2.3e.

Since [18] is the only density-based two-fluid heat exchanger optimization approach that allows for a variable wall-thickness, their non-mixing constraint is further investigated. The non-mixing constraint enforces a minimum wall-thickness is by adding a penalization term to their objective function. This penalization term is a continuity function that prevents two adjacent cells from containing different fluids. The continuity function is scaled within the objective function for smooth convergence. The fine-tuning required for the selection of this scaling parameter and the influence on the convergence behaviour is unknown. It could be that their method can also be implemented within a finite element computational framework by searching in elements instead of cells. The topic was not further investigated, since it is not in the scope of this project. All other density-based articles make use a finite element method (FEM) to discretize the design domain. A density-based non-mixing constraint that allows for a variable wall-thickness and guarantees a minimum wall-thickness has not been implemented within a finite element computational framework, leaving a gap for further research. In this project the implementation of a FEM non-mixing constraint with a minimum wall-thickness is investigated.

The other state of the art two-fluid heat exchanger topology optimization method investigated is level-set based topology optimization. The two level-set based articles available are from the same author, [8] and [7]. In both articles the same non-mixing constraint formulation is used to guarantee a minimum wall-thickness and allow for a variable wall-thickness. Two optimal designs generated with this level-set based non-mixing constraint are provided in Fig. 2.4a and 2.4b.

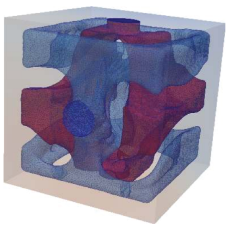

(a) Result of a 3D two-fluid heat exchanger topology optimization [8].

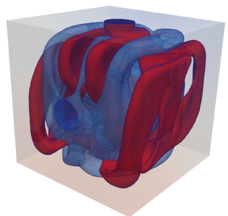

(b) Result of a 3D two-fluid heat exchanger topology optimization [7].

Figure 2.4: optimal designs generated with level-set topology optimization.

The minimum wall-thickness is guaranteed by computing the distance between the solid boundary interfaces and formulating this in an inequality constraint. In the inequality constraint the minimum wall-thickness is defined, which forces the optimizer to generate a wall-thickness equal or larger than the pre-defined minimum wall-thickness. A non-mixing constraint that guarantees a minimum wall-thickness and allows for the forming of a variable wall-thickness does already exist in level-set based topology optimization. However, such a non-mixing constraint does not exist in density-based topology optimization. A non-mixing constraint with similar properties in a density-based topology optimization method would constitute a contribution to science. Based on this gap found in literature, the following research question is formulated:

> *Can a non-mixing constraint for density-based two-fluid topology optimization be created that guarantees a minimum wall-thickness and also allows for a wall-thickness larger than the minimum implemented within a finite element computational framework?*

2.3. Contribution

The contribution to the state of the art in density-based two-fluid heat exchanger optimization is an optimization model with a non-mixing constraint that allows for the forming of a variable wall-thickness and guarantees a minimum wall-thickness. The proposed model can handle two different fluids. The optimization model works for both two dimensional (2D) and three dimensional (3D) optimization scenarios. To allow for an optimization model that can generate a variable wall-thickness, the two design variable approach introduced in [14] is extended. The same two design variable definition is used to separate the solid and two fluid regions. However, the interpolation functions are extended to prevent the forming of a zero thickness wall and in addition two fluids with different material properties can be used.

2.4. Report Outline

Apart from the abstract and introduction, this report consists of five chapters on the investigation of the non-mixing constraint, a discussion and a conclusion. In Chapter 3 all methods used in the optimization model are provided. This chapter is subdivided into four sections; the physics, density-based topology optimization, the non-mixing constraint and the optimization set-up. In Chapter 4 the behaviour and performance of the non-mixing constraint is investigated. In Chapter 5 the extended interpolation functions are compared to the original interpolation functions from literature [14] to determine the difference in optimization behaviour. Chapter 6 is dedicated to determining the influence of different material parameters on the interpolation and optimization behaviour. In Chapter 7 the 2D optimization model is extended to 3D and used in two different 3D optimization scenarios. In the discussion in Chapter 8 the limitations of the optimization model and topics for further investigation are elaborated on. The conclusion in Chapter 9 provides a brief summary of the numerical experiments on the performance of the optimization model.

3
Methods

In this chapter the different methods used in the optimization model are elaborated on. The chapter is divided into three sections. In Section 3.1 the physics of the heat exchanger and the coupling to the design field are explained. In Section 3.3 the design variables, filtering functions, projection functions and interpolation functions used to guarantee a non-mixing region are provided. In Section 3.4 a general formulation for the design domain, the boundary conditions, passive regions, material parameters and parameter continuation scheme are provided. In addition the objective functions, constraint functions and update algorithm used to improve the design are elaborated on.

3.1. Physics

In this section the physics used to describe the behaviour of a two-fluid heat exchanger are elaborated on. The heat exchanger in this optimization model uses the following physics: fluid mechanics and heat transfer.

3.1.1. Fluid Flow

Both fluids in the heat exchanger are assumed to be Newtonian, have a laminar flow characteristic and are governed by the Navier-Stokes equations. The momentum and continuity equation of the Navier-Stokes equations are shown in Eq. 3.1 and 3.2.

$$\rho(\frac{\partial \mathbf{u}}{\partial t} + \mathbf{u}\nabla\mathbf{u}) = -p + \mu\nabla^2\mathbf{u} + \mathbf{f} + \rho\mathbf{g}, \tag{3.1}$$

$$\nabla\mathbf{u} = 0, \tag{3.2}$$

where ρ is the density of the fluid, u is the velocity field, t is the time, p is the pressure field, μ is the viscosity of the fluid, f is a body forces term and g is gravity. The physics are solved for the steady-state solution, which means that the time dependent term drops out of the momentum equation. Furthermore, gravity is not taken into account in this optimization problem and is also excluded from the momentum equation, resulting in:

$$\rho(\mathbf{u}\nabla\mathbf{u}) = -p + \mu\nabla^2\mathbf{u} + \mathbf{f}. \tag{3.3}$$

Within the framework of topology optimization for fluid problems the term $\mathbf{f}$ is used as a friction term to penalize the fluid flow in the solid regions [4]. The body forces term is set equal to minus the inverse permeability (α) multiplied with the flow velocity:

$$\mathbf{f} = -\alpha\mathbf{u}, \tag{3.4}$$

where α is the inverse permeability, which is used to scale the magnitude of the friction in the solid domain. When α is equal to zero the fluid can flow freely (no penalization) and when α is equal to infinity the fluid is stagnant, inverse permeability α is thus used to divide the design domain into a fluid (α = 0) and solid ($\alpha \to \infty$) part. The maximum value for α is not set to ∞, but is set to a value to sufficiently penalize and inhibit flow in solid material regions. Substituting the body forces term in Eq. 3.3 will lead to the following momentum equation:

$$\rho(\mathbf{u}\nabla\mathbf{u}) = -p + \mu\nabla^2\mathbf{u} - \alpha\mathbf{u}. \tag{3.5}$$

The maximum value for α is chosen depending on the element length of the mesh h, the viscosity of the fluid μ and a scaling term C_1 (penalization scaling parameter). Eq. 3.6 shows the function used to determine the maximum value for α:

$$\alpha_{max} = C_1\mu\frac{1}{h^2}. \tag{3.6}$$

In the optimization model two sets of Navier-Stokes equations are used. A different set of Navier-Stokes equations is used for each fluid, since the optimization model must be able to handle two fluids with different material properties.

3.1.2. Heat Transfer

The governing equation used for the heat transfer is the convection-diffusion equation:

$$\rho c_p\frac{\partial T}{\partial t} + \rho c_p\mathbf{u}\nabla T + f_t = k\nabla^2 T, \tag{3.7}$$

where c_p is the heat capacity of the fluid, T is the temperature field, f_t is a heat source term and k is the thermal conductivity of the material. The governing equations are solved for steady state, therefore the time dependent term drops out. No external heat source is used in the heat exchanger designs, so f_t also drops out of the equation resulting in:

$$\rho c_p\mathbf{u}\nabla T = k\nabla^2 T. \tag{3.8}$$

The value for k is interpolated between the thermal conductivity of the two fluids and solid material regions, since all material regions conduct heat. The governing equations are one-way coupled, so the temperature field depends on the flow velocity field only and not vice versa.

3.2. Density-Based Topology Optimization

The non-mixing constraint is implemented in a density-based topology optimization method. The density-based topology optimization method used is a material interpolation method, since it allows for multi-material topology optimization. The material interpolation method makes use of a design or density variable which interpolates material properties, and consequently distinguishes between phases (solid material and fluids). The design variable has a lower and upper limit, the lower limit is 0 or $\rightarrow 0$ and the upper limit is 1. Depending on the material interpolation function used, the function interpolates between two or more materials or phases. A commonly used material interpolation method is the Simplified Isotropic Material with Penalization (SIMP) method [3]. Their SIMP method makes use of the power law to couple the density variable to the material stiffness:

$$E(\rho) = \rho^p E_0, \tag{3.9}$$

where ρ is the density (or design) variable, E_0 the stiffness of the solid material and p the coefficient used to alter the shape of the interpolation function. The coefficient p can be increased to further penalize the intermediate density states ($\rho \approx 0.5$) to converge to a more discrete solution. By increasing the coefficient p the interpolation function becomes more concave, but increasing p can lead to a poor convergence behaviour. Their interpolation function is used in a void-solid topology optimization scenario, where the material stiffness is interpolated between the void where $\rho \rightarrow 0$ and solid where $\rho = 1$. In density-based topology optimization a design variable can be used directly or indirectly in an interpolation function. When the design variable is used directly, the design variable is substituted in the interpolation function without additional filtering and projection. When the design variable is used indirectly (blurring-) filters and projection functions [13] are used. In the classical density-based topology optimization only an interpolation function was used to parametrize the design domain. The interpolation function directly interpolated the density variable (ρ) and restrictions are placed directly on this variable. However, optimal design generated with only an interpolation function can have large regions with intermediate densities ($\rho \approx 0.5$). These diffuse regions are undesirable and to reduce the size of these regions, filtering and projection functions are used. A density filter creates a new filtered density variable $\bar{\rho}$ from the original density variable ρ. The filtering operation makes the density at the elements depending on the density values of the neighbouring elements. For the filtering operation usually a Helmholtz type differential equation [12] is used:

$$-R^2\nabla^2\bar{\rho} + \bar{\rho} = \rho, \tag{3.10}$$

where R is the length parameter for the filter size, ρ the density variable and $\bar{\rho}$ the filtered density variable. A projection function is often combined with a Helmholtz-type filter to project the filtered density variable $\bar{\rho}$ to the lower bound (0) and upper bound (1). A projection function commonly used is the smoothed Heaviside projection function [27]:

$$\hat{\bar{\rho}} = \frac{tanh(\beta\eta) + tanh(\beta(\bar{\rho} - \eta))}{tanh(\beta\eta) + tanh(\beta(1 - \eta))}, \tag{3.11}$$

where β is the slope parameter, η the projection threshold, $\bar{\rho}$ the filtered density variable and $\hat{\bar{\rho}}$ the projected density variable. The slope parameter β increases the slope of the Heaviside function to make the projection more discrete. During the optimization process a continuation on the slope parameter β can be used to further reduce the region with intermediate densities.

In two-fluid heat exchanger topology optimization the design variable is not used to interpolate between the void and solid material, but between solid material and fluids. The distinction between solid and fluid is enforced with a body forces term added to the Navier-Stokes equations as introduced in Eq. 3.1. In two-fluid heat exchanger topology optimization, interpolation functions are used to interpolate the inverse permeability α in the body forces term in Eq. 3.4.

3.3. Non-Mixing Constraint

In this section the design variables and the coupling to the physics as shown in Section 3.1 are introduced. To guarantee a wall between the fluids that can vary in thickness a novel non-mixing constraint is proposed.

3.3.1. Non-Mixing Variable

To guarantee a minimum wall-thickness and allow for the forming of a variable wall-thickness, the multi design variable approach from [14] is applied. Since, in this approach two design variables can be used to define the material regions in the design domain. The first design variable, θ_1, interpolates between the fluid regions and solid regions. The second design variable, θ_2, interpolates between the different fluids. Table 3.1 shows the definition of the interpolation values.

	θ_1	θ_2
0	fluid region (fluid 1 and fluid 2 combined)	fluid 1
1	solid region	fluid 2

Table 3.1: Values of the design variables corresponding to the material regions.

To guarantee a non-mixing constraint with a minimum wall-thickness that allows the wall-thickness to vary, the two design variable approach [14] is combined with the two-step filtering and projection method [5]. In their two-step filtering and projection method a single design variable is used, to impose a material region with a fixed thickness at the material interface. The material region imposed at the interface can be used to guarantee a minimum wall-thickness between the two fluids as used in [9] and [10]. In the proposed non-mixing constraint, θ_1 is blurred using a Helmholtz-type filter (Eq. 3.12) and than projected with a smoothed Heaviside function (Eq. 3.13). First. we introduce some notation conventions. A filtered design variable is denoted with a bar ($\bar{\theta}$) and a projected design variable is denoted with a hat ($\hat{\theta}$).

$$\bar{\theta} = B(\theta, R) = \theta - R^2\nabla^2\bar{\theta}, \tag{3.12}$$

where R is the filter radius, θ the design variable and $\bar{\theta}$ the filtered design variable. All projection operations performed make use of a smoothed Heaviside function denoted with P, as provided in Eq. 3.13.

$$\hat{\bar{\theta}} = P(\bar{\theta}, \beta, \eta) = \frac{tanh(\beta\eta) + tanh(\beta(\bar{\theta} - \eta))}{tanh(\beta\eta) + tanh(\beta(1 - \eta))}, \tag{3.13}$$

where β is the projection slope parameter, η the projection threshold, $\bar{\theta}$ the previously filtered design variable and $\hat{\bar{\theta}}$ the filtered and projected design variable. The region where the non-mixing constraint should be active is in the region between the two fluids, where θ_2 switches from 0 to 1. Since θ_2 interpolates between the two fluids it defines the region where the two fluids touch and the non-mixing constraint should be active. The minimum wall-thickness between the two fluids can be guaranteed with the two-step filtering and projection method [5] applied to θ_2. In the first step of the two-step method, the design variable is blurred using a Helmholtz-type filter (Eq. 3.12) and than projected with a smoothed Heaviside function (Eq. 3.13). The first step is used to separate the two different fluids, $\hat{\bar{\theta}}_2 = 0$ (fluid 1) and $\hat{\bar{\theta}}_2 = 1$ (fluid 2). Two Helmholtz-type filters are used for θ_1 and θ_2, and two projection functions are used on the filtered design variables $\bar{\theta}_1$ and $\bar{\theta}_2$. The first filtering and projection operations are denoted in the following manner:

$$
\begin{aligned}
\hat{\bar{\theta}}_1 &= P(B(\theta_1, R_1), \beta_1, \eta_1),\\
\hat{\bar{\theta}}_2 &= P(B(\theta_2, R_2), \beta_2, \eta_2).
\end{aligned}
\tag{3.14}
$$

After the first filtering and projection step applied to θ_2, $\hat{\bar{\theta}}_2$ is renamed as θ_3 (non-mixing variable) for convenience of the derivation. In the second step of the two-step method, θ_3 is blurred with a Helmholtz-type filter (Eq. 3.12) and then projected with a bandpass projection function (Eq. 3.15) to impose a wall of fixed thickness on the two fluid interface defined with θ_2. This bandpass projection function consists of two smoothed Heaviside functions that are subtracted.

$$
\hat{\bar{\theta}}_3 = P(B(\theta_3, R_3), \beta_3, \eta_3) - P(B(\theta_3, R_3), \beta_3, \eta_4). \tag{3.15}
$$

To impose the wall, an equal amount of material is eroded from the two fluid domains at the interface between the two fluids. Material is eroded by using $\hat{\bar{\theta}}_2$ to define a "new" design field θ_3 which only adds a solid wall at the fluid interface. The symmetrical erosion behaviour of the non-mixing filter is enforced by blurring $\bar{\theta}_3 = B(\theta_3, R_3)$, which creates a region of intermediate material at the fluid interface ($\bar{\theta}_3 \approx 0.5$). The blurred design is put through the bandpass projection function, which projects the intermediate material region to a new solid material region defined with $\hat{\bar{\theta}}_3 = 1$. The new solid material region or non-mixing region is the minimum wall-thickness between the two fluids. In both smoothed Heaviside function the same slope control parameter (β_3) is used to ensure a symmetrical projection behaviour. Fig. 3.1a shows the contribution of $P(\bar{\theta}_3, \beta_3, \eta_3)$ and Fig. 3.1b shows the contribution of $P(\bar{\theta}_3, \beta_3, \eta_4)$ to the bandpass projection function. The complete bandpass projection function is shown in Fig. 3.1c.

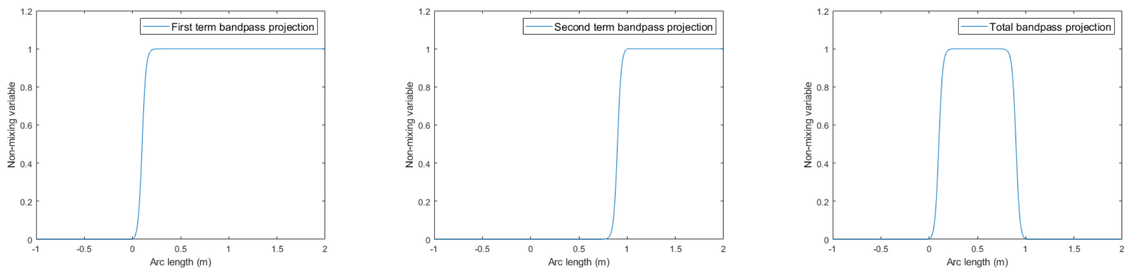

(a) A smooth Heaviside projection function is used with threshold value $\eta_3 = 0.1$ and $\beta_3 = 25$.

(b) A smooth Heaviside projection function is used with threshold value $\eta_4 = 0.9$ and $\beta_3 = 25$.

(c) The second projection function is subtracted from the first projection function to get a bandpass-filter.

Figure 3.1: Second projection operation.

For lower β_3 values the bandpass-projection filter does not interpolate between 0 and 1. This means that for lower β_3 values the projection step will give intermediate values in the non-mixing region. Fig. 3.2 shows the shape of the interpolation function for the β_3 values 3, 8 and 25. With $\eta_3 = 0.1$ and $\eta_4 = 0.9$, the bandpass projection function interpolates between 0 and 1 from $\beta_3 \geq 8$.

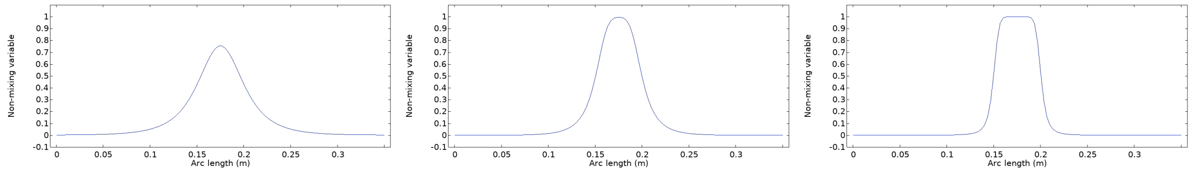

(a) $\beta_3 = 3$. (b) $\beta_3 = 8$. (c) $\beta_3 = 25$.

Figure 3.2: Plot of the non-mixing function for the slope parameter β_3 is 3, 8 and 25. For values lower as 8 the function does not interpolate between the values 0 and 1.

Fig. 3.3 illustrates the order of the filtering and projection steps applied to each design variable and the use of the filtered and projected design variables in defining the different materials. The first design variable θ_1 only defines the solid material region and inhibits the flow in these regions. The second design variable θ_2 separates the two different fluids in the first step of the two-step filtering and projection method and inhibits the flow of the first fluid in the region of the second fluid and vice versa. In the second step of the two-step filtering and projection method the non-mixing region is defined with $\hat{\bar{\theta}}_3$, which inhibits the flow in the non-mixing region.

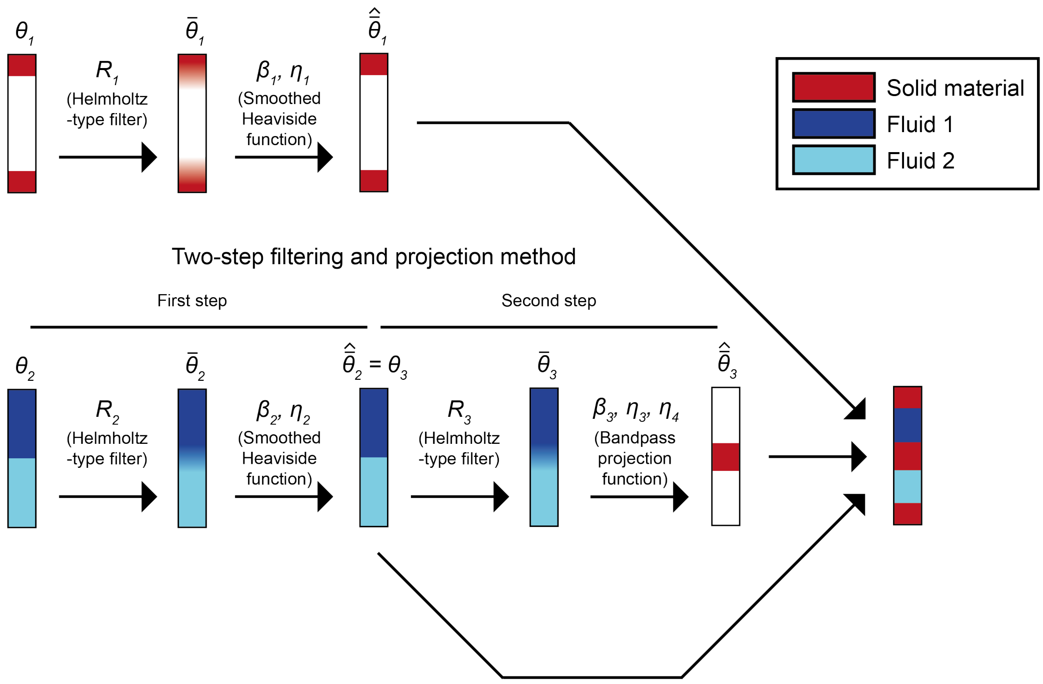

Figure 3.3: Filtering and projection steps used to separate the two different fluids and solid material and guarantee a non-mixing region.

An overview of the parameters and their description is provided in Table 3.2.

Design variable	Parameter	Description
θ_1	R_1	Filter radius first design variable
	β_1	Slope control parameter first design variable
	η_1	Projection threshold value first design variable
θ_2 (first step)	R_2	Filter radius second design variable
	β_2	Slope control parameter second design variable
	η_2	Projection threshold value second design variable
θ_2 (non-mixing filter)	R_3	Filter radius second design variable
	β_3	Slope control parameter second design variable
	η_3	Lower threshold bandpass filter
	η_4	Upper threshold bandpass filter

Table 3.2: The parameters used in the filtering and projection scheme.

The threshold values of η_1, η_2, η_3 and η_4 are fixed at 0.5 (to guarantee symmetry), 0.5 (to guarantee symmetry), 0.1 and 0.9. Depending on the optimization scenario used, the filter radii and slope control parameters are adjusted. A table with the value used for each parameter is provided with every optimization scenario. The thickness of the non-mixing filter can be expressed as a function of the parameters used in the two-step filtering and projection method. Since the projection threshold values (η) used have constant values, the contribution to the minimum wall-thickness is identical in each optimization scenario. To verify the dependence of the wall-thickness on the first filter radius (R_2), the wall-thickness is computed for three different values of R_2: 20 [mm], 40 [mm] and 60 [mm]. The other parameters have fixed values and are set to: $\beta_2 = 8$, $R_3 = 15$ [mm], $\beta_3 = 100$. This set-up has the following filter radius relations: $R_2 > R_3$ for all scenarios. Fig. 3.4 shows the plots of the wall-thickness for the different values of R_2.

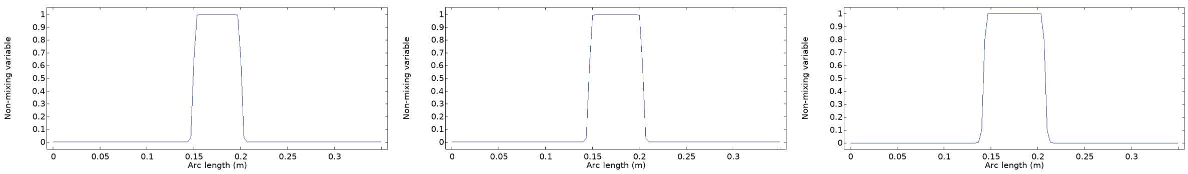

(a) $R_2 = 20$ [mm]. (b) $R_2 = 40$ [mm]. (c) $R_2 = 60$ [mm].

Figure 3.4: Influence of the filter size R_2 on the wall-thickness with a low β_2 value. $R_3 = 15$ [mm] ($R_2 > R_3$), $\beta_2 = 8$ and $\beta_3 = 100$.

The plots show that the size of the minimum wall-thickness depends on the filter radius size of R_2 for lower β_2 values. To investigate if the contribution of the filter radius size R_2 on the minimum wall-thickness diminishes for higher β_2 values, the following three filter radii relations are investigated: $R_2 < R_3$, $R_2 = R_3$ and $R_2 > R_3$. The value for β_2 is increased from 8 to 100, while the value of β_3 is kept at 100. The filter radius R_3 is set 25 [mm], while a parameter sweep is performed on R_2 with the values 10 [mm], 25 [mm] and 40 [mm]. Fig. 3.5 shows the plots of the minimum wall-thickness for the three scenarios now with $\beta_2 = 100$ and R_2 is 10 [mm], 25 [mm] and 40 [mm].

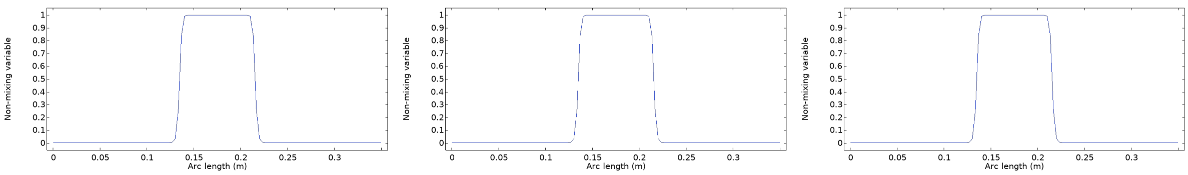

(a) $R_2 = 10$ [mm]. (b) $R_2 = 25$ [mm]. (c) $R_2 = 40$ [mm].

Figure 3.5: Influence of the filter size R_2 on the wall-thickness with a high β_2 value. $R_3 = 25$ [mm] ($R_2 > R_3$) and $\beta_2 = \beta_3 = 100$.

The plotted results show an identical wall-thickness regardless of R_2. In other word, for a sufficiently high β_2 value the wall-thickness is independent of filter radius R_2. The contribution of β_2 and β_3 to the minimum wall-thickness is negligible for sufficiently high β_2 and β_3 values, since for higher β values the slope of the projection functions approaches infinity. The threshold value of η_2 is fixed at 0.5, which is at the center line of the transition between the two fluids and therefore does not contribute to the minimum wall-thickness formed by the non-mixing filter. For sufficiently high β values the minimum wall-thickness depends only on R_3, η_3 and η_4. For sufficiently high β values the minimum wall-thickness can be approximated with the following equation:

$$\begin{gathered} t_{min}(R_3,\eta_3,\eta_4) \approx -2\cdot R_3 \ln(\eta_3+(1-\eta_4)), \\ 0<\eta_3<1, \\ 0<\eta_4<1, \\ \eta_3<\eta_4, \\ (\eta_3=1-\eta_4). \end{gathered} \tag{3.16}$$

The approximation of the minimum wall-thickness provided in Eq. 3.16 is valid for the parameter conditions provided with the equation. The last condition provided in Eq. 3.16 is the symmetry condition used for a symmetrical erosion behaviour. The minimum wall-thickness t_{min} has to be used as an input to express the filter radius R_3. R_3 is expressed as a function of t_{min}, η_3 and η_4 for sufficiently high β values in the following equation:

$$\begin{gathered} R_3(t_{min},\eta_3,\eta_4) = -\frac{t_{min}}{2\cdot \ln(\eta_3+(1-\eta_4))}, \\ 0<\eta_3<1, \\ 0<\eta_4<1, \\ \eta_3<\eta_4, \\ (\eta_3=1-\eta_4). \end{gathered} \tag{3.17}$$

The parameters η_3 and η_4 have constant values of $\eta_3 = 0.1$ and $\eta_4 = 0.9$ in all optimization scenarios, therefore the expression of the filter radius R_3 can be simplified to Eq. 3.18 for sufficiently high β values.

$$\begin{gathered} R_3(t_{min}) = -\frac{t_{min}}{2\cdot \ln(0.1+(1-0.9))} \approx \frac{t_{min}}{3.2}, \\ \eta_3=0.1, \\ \eta_4=0.9. \end{gathered} \tag{3.18}$$

The minimum wall-thickness is defined as the distance between the points evaluated at $\theta_3 = 0.5$, see Fig. 3.6.

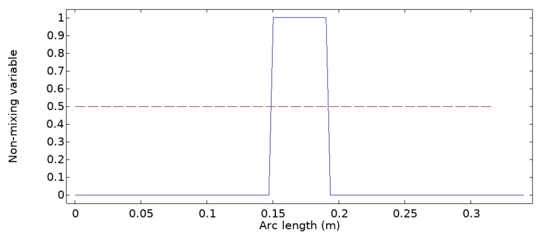

Figure 3.6: Plot of the non-mixing region separating the two fluids. The red dashed line at θ_3 = 0.5 is the distance evaluation value and the red solid region is the wall-thickness.

It has to be mentioned that the value for t_{min} has to be selected larger than the mesh size (h). The reason for this is the shape function and element order of the shape funtion used, these two properties determine if a certain shape can be accurately represented within a mesh element. The type of shape function used is Lagrange shape functions with a quadratic element order, therefore the bandwidth projection can not be accurately represented within a single mesh element. Fig. 3.7 shows the interpolation shapes for different t_{min} values, while the other parameter values are fixed.

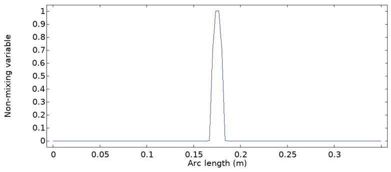

(a) $t_{min} = 0.01$[m].

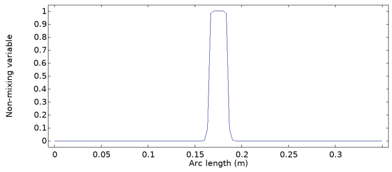

(b) $t_{min} = 0.02$[m].

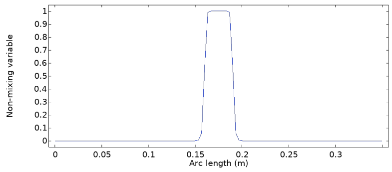

(c) $t_{min} = 0.03$[m].

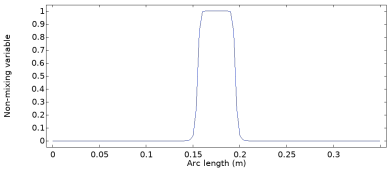

(d) $t_{min} = 0.04$[m].

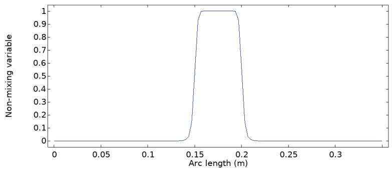

(e) $t_{min} = 0.05$[m].

Figure 3.7: Plots of the interpolated minimum wall-thickness for different t_{min} values, with $h = 0.01$[m] and $\beta = 50$.

The mesh size (h) used here has a fixed value of 0.01[m], the filter radii have fixed values of $R_1 = R_2 = 0.02$[m] and the value for all β parameters is set to 50. For t_{min} values lower than or equal to the mesh size, the projection shape becomes poorly approximated within a mesh element and the overall shape of the non-mixing region becomes discontinuous. It is therefore recommended to select a t_{min} value larger than the mesh size. The higher the number of elements used to approximate the bandwidth projection the more accurate the projection shape is represented.

3.3.2. Interpolation Functions

Two sets of Navier-Stokes equations are used to separate the two different fluids. Each fluid has its own set of Navier-Stokes equations to define the different material properties if the fluids are not identical. To prevent both fluids from flowing in the same region, the flow penalization α in Eq. 3.5 is used. Each fluid has a different flow penalization, α_1 for fluid 1 and α_2 for fluid 2. Thus two different interpolation functions are used for α_1 and α_2. The interpolation functions used for α_1 and α_2 are provided in Eq. 3.19 and 3.20. The maximum penalization value α_{max} used in the interpolation functions is set with Eq. 3.6. In the interpolation functions the filtered and projected design variables $\hat{\hat{\theta}}_1$, $\hat{\hat{\theta}}_2$ and $\hat{\hat{\theta}}_3$, which imposes the wall at the fluid interface, are used. The exponents in the interpolation functions are all denoted with p. The exponent in an interpolation function is used to adjust the interpolation shape. The higher the value of an exponent, the more concave the shape of the interpolation function becomes and the smaller the region with intermediate values ($\theta \approx 0.5$) becomes. The exponents all have the same value of $p = 3$. The exponents all have the same value to ensure an identical interpolation shape with each filtered and projected design variable.

$$\alpha_1(\hat{\hat{\theta}}_1,\hat{\hat{\theta}}_2,\hat{\hat{\theta}}_3) = \alpha_{1,max}\left(1-(1-\hat{\hat{\theta}}_1^p)(1-\hat{\hat{\theta}}_2^p)\right) + \alpha_{1,max}\left((1-\hat{\hat{\theta}}_1^p)(1-\hat{\hat{\theta}}_2^p)\hat{\hat{\theta}}_3^p\right). \tag{3.19}$$

$$\alpha_2(\hat{\hat{\theta}}_1,\hat{\hat{\theta}}_2,\hat{\hat{\theta}}_3) = \alpha_{2,max}\left(1-(1-\hat{\hat{\theta}}_1^p)(1-(1-\hat{\hat{\theta}}_2)^p)\right) + \alpha_{2,max}\left((1-\hat{\hat{\theta}}_1^p)(1-(1-\hat{\hat{\theta}}_2)^p)\hat{\hat{\theta}}_3^p\right). \tag{3.20}$$

The first term of each interpolation function is identical to the interpolation function used in [14]. The first term in each interpolation function has two properties. The first property is penalizing the fluid flow in the solid material regions, which is performed with $(1-\hat{\hat{\theta}}_1^p)$ in both interpolation functions. The second property is penalizing the fluid flow in the region of the other fluid. The flow velocity of fluid 2 has to be penalized in the region of fluid 1, which is performed with $(1-\hat{\hat{\theta}}_2^p)$ in Eq. 3.19. The flow velocity of fluid 1 has to be penalized in the region of fluid 2, which is performed with $(1-(1-\hat{\hat{\theta}}_2)^p)$ in Eq. 3.20. The second term (non-mixing term) in each interpolation function has a single property, to penalize the fluid flow in the non-mixing region. The second term has to be inactive when the first term is already active to prevent both terms from contributing to the flow penalization in the overlapping material regions. If the second term is not inactive when the first term is active the penalization values can be increased up to twice a_{max}, since both terms in each interpolation function are multiplied with the maximum penalization value a_{max}. If the first term is already active with $(1-\hat{\hat{\theta}}_1^p)(1-\hat{\hat{\theta}}_2^p)$, the second term in Eq. 3.19 is set to 0. $(1-\hat{\hat{\theta}}_1^p)$ prevents the second term from also penalizing the fluid flow in the solid material region and $(1-\hat{\hat{\theta}}_2^p)$ prevents the second term from also penalizing the fluid flow in the region of the other fluid. If the first term is already active with $(1-\hat{\hat{\theta}}_1^p)(1-(1-\hat{\hat{\theta}}_2)^p)$, the second term in Eq. 3.20 is set to 0. $(1-\hat{\hat{\theta}}_1^p)$ prevents the second term from also penalizing the fluid flow in the solid material region and $(1-(1-\hat{\hat{\theta}}_2)^p)$ prevents the second term from also penalizing the fluid flow in the region of the other fluid. The interpolation functions can be simplified to the following equations:

$$\alpha_1(\hat{\hat{\theta}}_1,\hat{\hat{\theta}}_2,\hat{\hat{\theta}}_3) = \alpha_{1,max}\left(1-(1-\hat{\hat{\theta}}_1^p)(1-\hat{\hat{\theta}}_2^p)(1-\hat{\hat{\theta}}_3^p)\right). \tag{3.21}$$

$$\alpha_2(\hat{\hat{\theta}}_1,\hat{\hat{\theta}}_2,\hat{\hat{\theta}}_3) = \alpha_{2,max}\left(1-(1-\hat{\hat{\theta}}_1^p)(1-(1-\hat{\hat{\theta}}_2)^p)(1-\hat{\hat{\theta}}_3^p)\right). \tag{3.22}$$

The interpolation functions have one undesirable property; in the region behind the non-mixing region the penalization values are slightly lower than α_{max}. Fig. 3.8a shows an initial design with two straight channels. The bottom channel corresponds to fluid 1 and the top channel corresponds to fluid 2. The corresponding normalized flow penalization field of α_1 is shown in Fig. 3.8b. The field of α_1 is normalized with the maximum penalization value α_{max}. The flow penalization field shows the region with lowered penalization values in the middle of the design domain, the horizontal light red line between the two fluid channels. The filter parameters used are $R_1 = R_2 = 0.03$ [m], $R_3 = 0.02$ [m] and $\beta_1 = \beta_2 = \beta_3 = 10$.

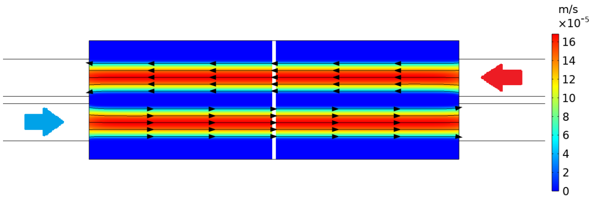

(a) Velocity field of an initial design with two straight fluid channels.

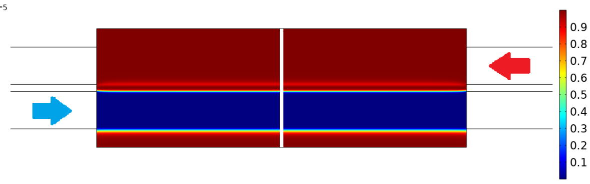

(b) Normalized flow penalization $\alpha_1/\alpha_{1,max}$ corresponding to the initial design in Fig. 3.8a.

Figure 3.8: Undesired property of interpolation functions.

The region with slightly lowered penalization values originates from the difference in effective Helmholtz type filter size. The filter size depends on the filter radius value selected for R_1, R_2 and R_3. Fig. 3.9 shows a plot of the normalized flow penalization values evaluated at the white line in Fig. 3.8b. The normalized maximum flow penalization value α_{max} is also plotted as a horizontal dashed line. The bounds of the region with slightly lowered penalization values are indicated with two vertical lines.

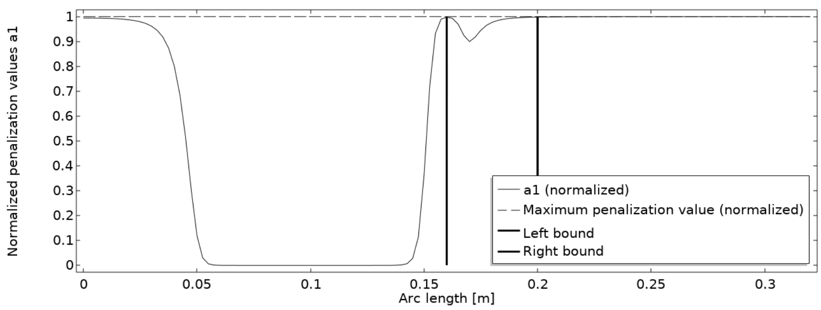

Figure 3.9: The plot shows the normalized flow penalization values corresponding to interpolation function α_1. The normalized maximum penalization value is provided as a dashed horizontal line. The left and right bound of the region with slightly lowered penalization values are provided as two black vertical lines.

The region with lowered penalization values is the region where the second Helmholtz type filter (R_2) is active and the non-mixing filter (R_3) is inactive. Fig. 3.10 shows the effective region of the second Helmholtz type filter and the non-mixing filter. Fig. 3.10a shows the contribution of the first term in Eq. 3.19 to α_1. The left- and right-bound indicate the boundaries of the intermediate material region originating from the first filtering (R_2) and projection (β_2 and η_2) step. The left- and right-bound are at approximately 0.15 [m] and 0.2 [m]. Fig. 3.10b shows the contribution of the second term in Eq. 3.19 to α_1. The left- and right-bound indicate the boundaries of the intermediate material region originating from the second filtering (R_3) and projection (β_3, η_3 and η_4) step. The left- and right-bound are at approximately 0.14 [m] and 0.18 [m]. The distance between the left and right bound depends on the size of the filter radii.

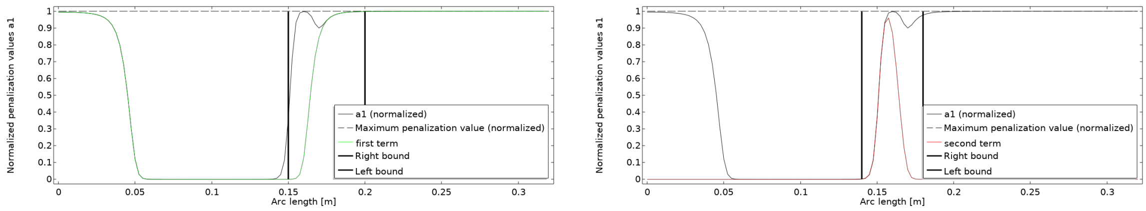

(a) Normalized flow penalization $\alpha_1/\alpha_{1,max}$ originating from the first term in Eq. 3.19.

(b) Normalized flow penalization $\alpha_1/\alpha_{1,max}$ originating from the second term (non-mixing term) in Eq. 3.19.

Figure 3.10: Contribution of both flow penalization terms in Eq. 3.19 to α_1.

The size of the filter radius R_2 is selected based on the desired gradient region needed to improve the design, while the size of the filter radius R_3 is set with t_{min} based on a preferred minimum wall-thickness. The region with sligthly lowered penalization values is negligable for the parameter relation $R_2 \leq t_{min}$. The region with sligthly lowered penalization values becomes more dominant, increased devaition from α_{max} and width, the larger the difference for the relation $R_2 > t_{min}$. Since the size of R_2 and t_{min} are set based on the optimization scenario selected, optimization scenarios with the parameter relation $R_2 > t_{min}$ can occur. The size of the region with lowered penalization values decreases with β increments, since increased β values reduce the intermediate material regions. Fig. 3.11 shows the normalized penalization values of α_1 evaluated at the white line in Fig. 3.8b for a β sweep from 10 to 40. All β parameters have an identical value in every β increment, thus $\beta_1 = \beta_2 = \beta_3$.

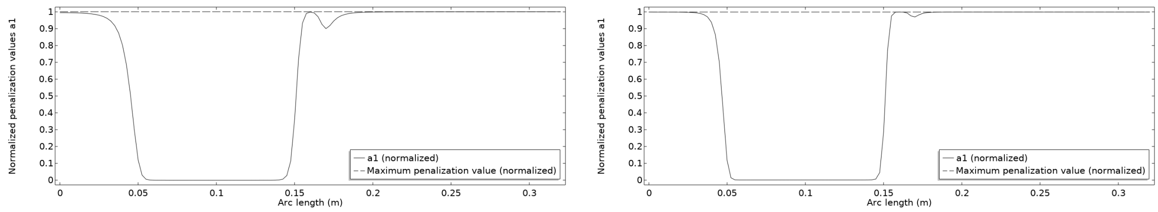

(a) Normalized flow penalization $\alpha_1/\alpha_{1,max}$ with $\beta_1 = \beta_2 = \beta_3 = 10$.

(b) Normalized flow penalization $\alpha_1/\alpha_{1,max}$ with $\beta_1 = \beta_2 = \beta_3 = 15$.

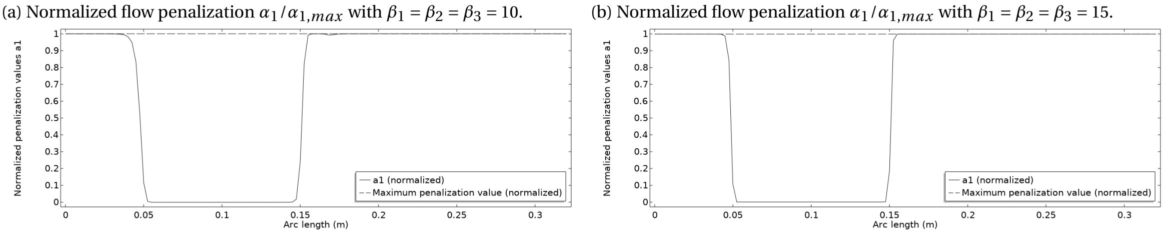

(c) Normalized flow penalization $\alpha_1/\alpha_{1,max}$ with $\beta_1 = \beta_2 = \beta_3 = 20$.

(d) Normalized flow penalization $\alpha_1/\alpha_{1,max}$ with $\beta_1 = \beta_2 = \beta_3 = 40$.

Figure 3.11: Normalized penalization values for β sweep from $\beta_1 = \beta_2 = \beta_3 = 10$ to $\beta_1 = \beta_2 = \beta_3 = 40$. The normalized penalization values are evaluated at the white line in Fig. 3.8b.

This undesirable interpolation behaviour does not have a negative side-effect on the optimal design generated when a sufficiently high α_{max} value is selected and the β parameters are increased sufficiently. Selecting appropriate values for α_{max} and β_{max} requires fine-tuning and will depend on the optimzation scenario selected. An appropriate β_{max} value can be found by performing a β sweep on the concerning initial design and select a β value where the region with lowered penalization values is diminished sufficiently. It could be argued that this undesirable interpolation behaviour might not have an significant effect on the flow penalization, since the penalization values are only slightly lowered. A parameter continuation on the β parameters is recommended anyways to reduce the intermediate material regions.

To interpolate the thermal properties of the fluids an additional interpolation function is used. The interpolation function for the thermal conductivity as provided in Eq. 3.23 consists of four terms. The first term is the thermal conductivity of the first fluid k_1. The second term interpolates between the thermal conductivity of the first fluid and the thermal conductivity of the solid material k_s. The first two terms are similar to the interpolation function used in [14], the only difference is that the second term adds the difference in thermal conductivity of the first fluid and solid material. Since contrarily to [14] two different fluids are used, this term is needed to interpolate to the correct thermal conductivity value. The third term is used to interpolate the thermal conductivity of the solid material defined by the non-mixing filter. The fourth term is used to interpolate the thermal conductivity to the second fluid k_2.

$$k(\hat{\hat{\theta}}_1,\hat{\hat{\theta}}_2,\hat{\hat{\theta}}_3) = k_1 + (k_s - k_1)\hat{\hat{\theta}}_1^p + (k_s - k_1)(1-\hat{\hat{\theta}}_1^p)\hat{\hat{\theta}}_3^p + (k_2 - k_1)(1-\hat{\hat{\theta}}_1^p)(1-\hat{\hat{\theta}}_3^p)\hat{\hat{\theta}}_2^p. \tag{3.23}$$

Each term in the interpolation function used for the thermal conductivity has the same exponent, which has the same value as the exponents in the interpolation functions of the flow penalization and is therefore also denoted with p. To show that the interpolation function correctly matches the material properties with the corresponding material regions, a cross section of an initial design with two straight channels is analysed. The same initial design is used as shown in Fig. 3.8a. The location where the thermal conductivity is evaluated is at the white line shown in Fig. 3.12a. The thermal conductivity at the evaluation line is plotted in Fig. 3.12b. The thermal conductivity values used are $k_1 = 0.6$ [W/(mK)] for fluid 1, $k_2 = 0.1233$ [W/(mK)] for fluid 2 and $k_s = 238$ [W/(mK)] for the solid material. A logarithmic y-axis scale is used to depict the different thermal conductivities of the fluids. The left valley corresponds to the bottom channel and the right valley to the top channel. The plot shows that the interpolation functions correctly defines the materials in the non-mixing region and interpolates correctly between the two different fluids.

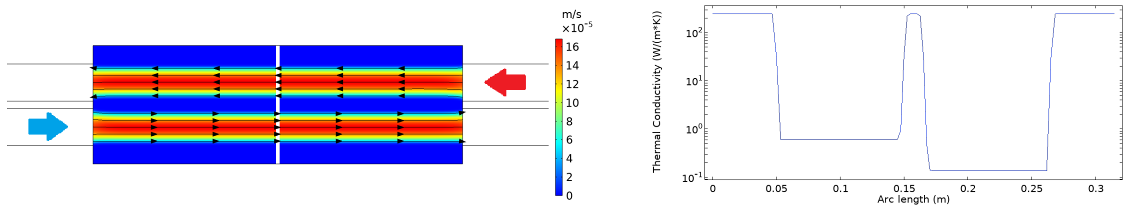

(a) Velocity field of an initial design with two straight fluid channels.

(b) Plot of the thermal conductivity evaluated at the white line in Fig. 3.12a.

Figure 3.12: Plot used to show the interpolation between the different material regions in a design with two different fluids.

When two identical fluids are used the fourth term drops out automatically, since for $k_1 = k_2$ this term is multiplied with 0 and the interpolation function simplifies to:

$$k(\hat{\hat{\theta}}_1,\hat{\hat{\theta}}_3) = k_1 + (k_s - k_1)\hat{\hat{\theta}}_1^p + (k_s - k_1)(1-\hat{\hat{\theta}}_1^p)\hat{\hat{\theta}}_3^p. \tag{3.24}$$

To show the contribution of each operation in the two-step method, the effect of each operation on the thermal conductivity field is plotted in Fig. 3.13. The thermal conductivity is here also used, since it distinguishes between all material regions. The same initial design is used as shown in Fig. 3.12a, all operations are evaluated at the white also shown in Fig. 3.12a.

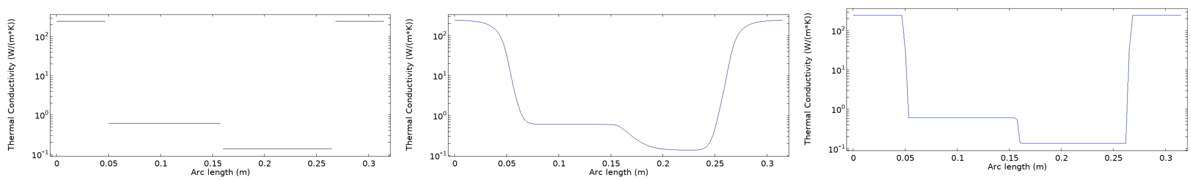

(a) Material regions defined with the discrete fields of the design variables θ_1 and θ_2.

(b) Material regions defined after the first two helmholtz filters ($R_1 = R_2 = 10$ [mm]) applied to the design variables to create $\tilde{\theta}_1$ and $\tilde{\theta}_2$.

(c) Material regions defined after projection of $\tilde{\theta}_1$ and $\tilde{\theta}_2$ with two separate Heaviside projection filters ($\beta_1 = 25, \eta_1 = 0.5, \beta_2 = 25 and \eta_2 = 0.5$) to create $\hat{\theta}_1$ and $\hat{\theta}_2$.

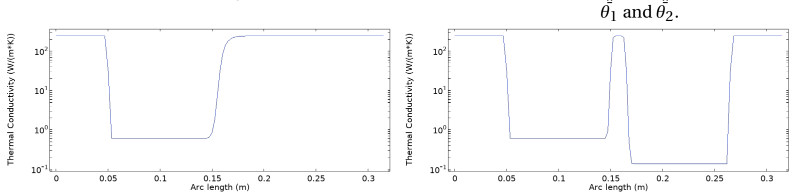

(d) Material regions defined after the third helmholtz-filter (t_{min} = 15 [mm]) applied to $\hat{\theta}_2 = \theta_3$ to create $\tilde{\theta}_3$.

(e) Material regions defined after the projection of $\tilde{\theta}_3$ with the bandpass projection filter ($\beta_3 = 25, \eta_3 = 0.1$ and $\eta_4 = 0.9$) to create $\hat{\hat{\theta}}_3$.

Figure 3.13: The influence of each operation in the two-step method on the material regions defined with the thermal conductivity. The optimization set-up used has two different fluids, which can be derived from the different thermal conductivity values in the two fluid channel regions.

It has to be mentioned that in optimization scenarios where two identical fluids are used still two separate fluid simulations are computed (two different sets of Navier-Stokes equations are solved). The reason for this is that the goal is to create a non-mixing constraint that can handle two different fluids. It is possible to alter the interpolation functions to be applied to a two-fluid heat exchanger optimization with identical fluids and a single fluid simulation. Using a single fluid simulation would significantly decrease the computation time of the physics and could, if an identical fluids scenario is selected be favourable. Since this is an interesting research direction an outline of the implementation is provided. To make the optimization model perform in a similar manner with a single fluid simulation set-up, the response functions and interpolation functions have to be altered. If the boundary objective function is used, the in- and outflow boundaries all correspond to the same fluid field and the in- and outflow boundary corresponding to the to be cooled fluid have to be selected. With a domain objective function the objective function can still be evaluated in the same design domain. The two pressure drop constraints used for each fluid channel will both be evaluated in the same fluid field. Instead of two interpolation functions for the flow penalization a single interpolation function is needed, as provided here:

$$\alpha_1(\hat{\hat{\theta}}_1, \hat{\hat{\theta}}_3) = a_{1,max}\left(1 - (1 - \hat{\hat{\theta}}_1^p)(1 - \hat{\hat{\theta}}_3^p)\right). \tag{3.25}$$

Eq. 3.25 is derived from Eq. 3.21, where the term $(1 - \hat{\hat{\theta}}_2^p)$ drops out. This term drops out since $\hat{\hat{\theta}}_2$ is used to make a distinction between the two fluids, but when a single fluid field is used the fluid flow only has to be penalized in the solid regions (including the non-mixing region). The single fluid field inverse permeability interpolation function can still generate a variable wall-thickness by using the term $(1 - \hat{\hat{\theta}}_3^p)$ to guarantee a minimum wall-thickness, while the term $(1 - \hat{\hat{\theta}}_1^p)$ can form solid regions around the non-mixing region. The interpolation function for the thermal conductivity, provided in Eq. 3.24, can also be used for this single fluid field optimization model. The single fluid simulation optimization model could have a significantly different optimization behaviour, since different field information is taken into account. A single fluid simulation optimization model is not further investigated in this thesis project, because it is preferred for the optimization model to distinguish between two different fluids.

3.4. Optimization Set-Up

In this section the set-up of the optimization algorithm is elaborated on. A template is provided which shows the size of the design domain and locations of the in- and outlets. The boundary conditions and the passive regions used to prevent mixing at the in- and outflow regions are elaborated on. A small investigation into realistic material properties is conducted. A continuation scheme for the optimization parameters is suggested with suitable lower and upper values for β. The objective and constraint functions used with their formulations are provided. The final section is dedicated to the sensitivities and the update method used in the optimization algorithm.

3.4.1. Design Domain

To provide a complete overview of the different design domains a template is created. Since most of the design domains are 2D, only a template is provided for the 2D design domains. In Chapter 7 a 3D design domain and separate optimization set-up are provided. Fig. 3.14 shows this template for the 2D designs. With every new optimization scenario a table is provided with the dimensions of the design domain (dimensional parameters). All four in- and outflow regions have the same height (L4) and length (L6). The in- and outflow regions are mirrored over the vertical center-line of the design domain. Two different types of design domains are used. The first type of design domain is provided on the left side in Fig. 3.14, this type of design domain has passive in- and outflow regions as further elaborated on in Section 3.4.3. The second type of design domain has an additional passive region surrounding the active part of the design domain, while the other dimensional parameters are defined in the same manner as the first type of design domain. The surrounding passive regions have a constant thickness denoted with L7, as shown on the right side in Fig. 3.14. The first type of design domain is used in Chapter 6, Chapter 7, Appendix B, Appendix C and Appendix D. The second type of design domain is used in Chapter 4 and 5.

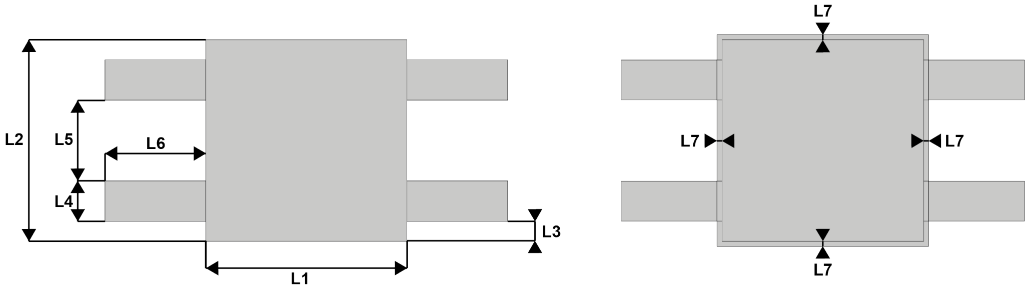

Figure 3.14: Length parameters used to define the size of the design domain.

For the meshing of the design domain a structured mesh is used with a square element shape, see Fig. 3.15. A structured mesh is used to ensure the physics are represented in the same manner within each mesh element. Since the element has a square shape the mesh size can be set with a single meshing parameter, h. The value in the optimization algorithm used for h is provided for every optimization scenario.

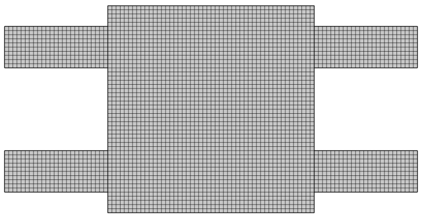

Figure 3.15: Example of a structured mesh used in the optimization algorithm.

3.4.2. Boundary Conditions

The heat exchanger has four open boundaries, two inflow and two outflow boundaries connected with in- and outflow regions to the design domain. The left image in Fig. 3.16 shows the in- and ouflow regions. In this report almost all 2D optimization scenarios the two upper open boundaries correspond to the to be cooled fluid and are marked in red, while the two bottom open boundaries correspond to the coolant and are marked in blue. The only exceptions are the 3D optimization scenario and the crossing channels heat exchanger scenario, see Chapter 7 and Appendix B. Since parallel- and counter-flow heat exchanger configurations are used, the in- and outflow locations can be switched from left to right and vice versa. The remaining outer boundaries as marked in black on the right side in Fig. 3.16 have a no-slip condition and are adiabatic.

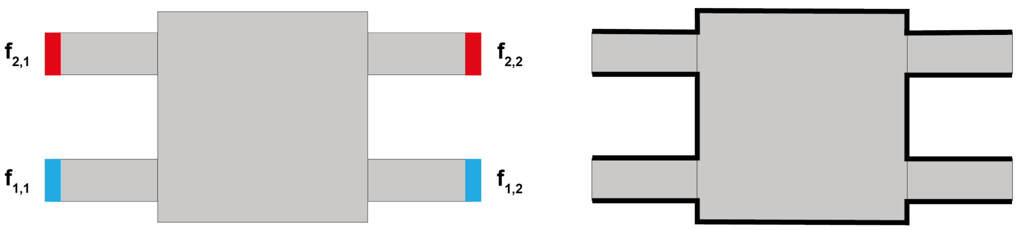

Figure 3.16: Boundaries to which the boundary conditions are applied. The boundaries $t_{1,1}$, $t_{1,2}$, $t_{2,1}$ and $t_{2,2}$ marked on the left side are the in- and outflow boundaries. The black lines marked on the right side have the no-slip conditions and are adiabatic.

The flow conditions at the inflow boundaries are defined as the average normal flow velocity (u_{in}) with a constant flow profile set with the Reynolds number:

$$u_{in} = \frac{Re_L \mu}{\rho L_{inlet}}, \tag{3.26}$$

where L_{inlet} is the characteristic length (inlet diameter) and Re_L the predefined Reynolds number. The inflow velocities for each fluid can be adjusted separately by altering the Reynolds number, so two different inflow velocity equations are used one for each fluid. The outflow conditions for each fluid are defined identically with a normal outflow conditions and no back-flow is allowed. The performance of the heat exchanger can be expressed as an efficiency. The efficiency here is expressed as the absolute value of the average temperature drop of the to be cooled fluid evaluated at the in- and outflow boundaries divided by the maximum possible temperature drop, this ratio is multiplied with 100 to express the efficiency as a percentage:

$$Eff = \frac{|T_{f2,1} - T_{f2,2}|}{T_{hot} - T_{cold}} \cdot 100, \tag{3.27}$$

where the average temperature drop of the to be cooled fluid is evaluated at $T_{f2,1}$ and $T_{f2,2}$ as shown on the left side in Fig. 3.16. The maximum temperature drop is expressed as inflow temperature of the coolant T_{cold} subtracted from the inflow temperature of the to be cooled fluid T_{hot}.

3.4.3. Passive Regions

The optimization model must have passive in- and outflow regions to ensure the non-mixing constraint guarantees a non-mixing region in the entire design domain. Fig. 3.17 shows the passive regions for each design domain type as introduced in Section 3.4.1.

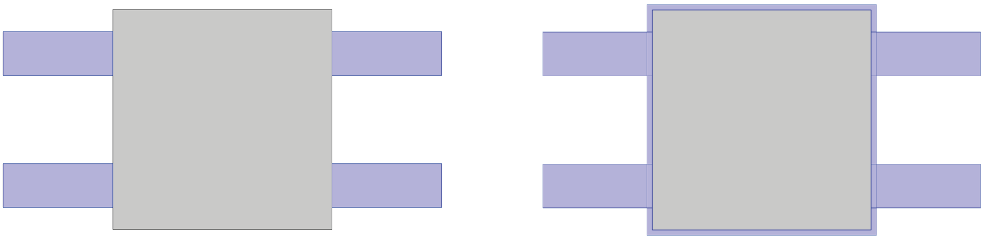

Figure 3.17: Passive material regions used in each design domain type.

If the passive regions are not used, the optimizer can generate fluid material regions in the in- and outflow regions of the other fluid up to the open boundaries. The non-mixing filter can not generate a non-mixing region between the fluids at the open boundary, since the design variables are not defined past the open boundaries leading to a mixing design. To ensure the fluid flow is penalized correctly for a design with fluid 1 in the bottom channel, the design variables in the passive regions have to be specified as provided in Fig. 3.18. The transition between $\theta_2 = 0$ and $\theta_2 = 1$ on the right side in Fig. 3.18b is centered between the in- and outflow regions in all optimization scenarios.

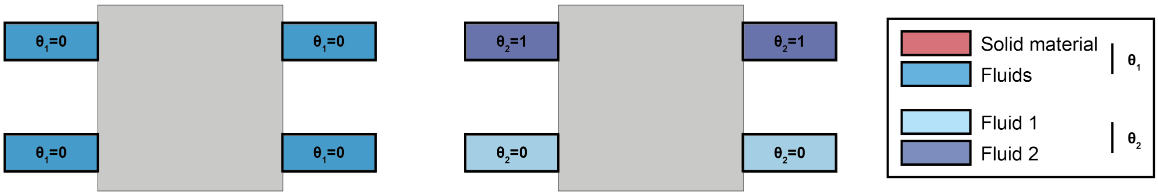

(a) Constant values for the design variables θ_1 and θ_2 in all passive regions used in the first type of design domain.

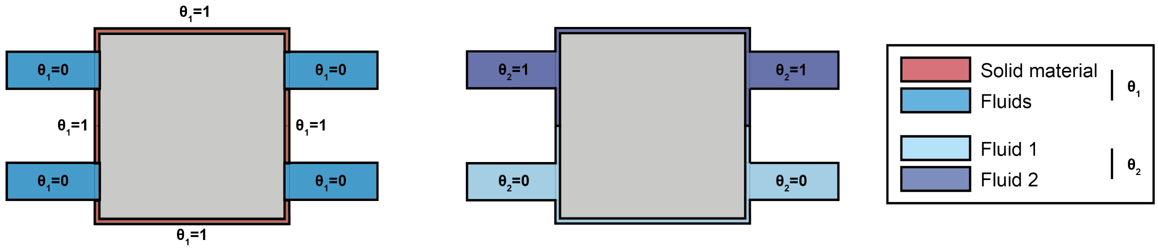

(b) Constant values for the design variables θ_1 and θ_2 in all passive regions used in the second type of design domain.

Figure 3.18: Values for design variables in all passive regions for both types of design domains. θ_1 distinguishes between the fluid ($\theta_1 = 0$) and solid material regions ($\theta_1 = 1$) and θ_2 distinguishes between the two fluids ($\theta_2 = 0$ for fluid 1 and $\theta_2 = 1$ for fluid 2).

3.4.4. Physical Material Parameters

To determine the material parameter values used for the materials in the optimization algorithm, a small investigation into physical material parameters is conducted. Physical material parameters means here that the material parameters selected for the material properties are based on measured material properties. If material parameters in the range of physical material parameters can be used in the optimization model, the opimization model can generate optimal designs that more accurately represent actual heat exchangers. The reason for this investigation is that depending on the material parameter values selected the optimization behaviour can alter significantly. Physical materials can have material properties with values spread over a wide range. Interpolating over a large value range can lead to large regions with intermediate values. These regions with intermediate values do not describe the physics accurately and should be minimized. To some extent this can be improved by a parameter continuation on the slope parameters (β) in the projection functions and increasing the exponents (p) in the interpolation functions. However, both proposed methods to reduce the regions with intermediate values can lead to poor convergence behaviour.

The collected measured material properties are provided in Table 3.3. Even though the material parameters are derived from measured material properties, the material parameters used in the optimization model are temperature independent. In actual heat exchangers the material properties do depend on the temperature of the materials. The temperature at which the temperature depending properties are evaluated and the corresponding references are provided with the data in Table 3.3. The material parameter values are derived from water for the coolant, engine oil for the to be cooled fluid and aluminium for the solid material. In the optimization model the inflow temperature of the coolant is set to 293 [K], therefore the material properties of water are collected at a temperature of approximately 293.15 [K]. For the material properties of engine oil, the material properties at specific temperatures depend on the type of engine oil selected. The data of all material properties corresponding to a specific engine oil are not as widely available, therefore the material properties used in this report are a combination of the available data. Based on the available material properties the inflow temperature of the to be cooled fluid is set to 333 [K]. To determine the specific heat ratio of an engine oil both the specific heat capacity at a constant pressure (c_p) and at a constant volume (c_v) are needed. The specific heat ratio of engine (SAE) oils depends on the chemical composition and mass ratio of each compound in the oil. Depending on the type of SAE oil it can be mineral, semi-synthetics or synthetic, which also has an influence on the mass ratio of each compound. The c_p value for some SAE oils can be found, but the c_v was not found. Since this topic on itself requires further research and this is not in the scope of this thesis project, the specific heat ratio of the engine oil is set to 1.

The investigation into material properties is conducted for a scenario with different fluids, since actual heat exchangers often have different fluids. Having different fluid also requires interpolation between the fluids, which is a topic to investigate to determine the robustness of the optimization model. If a different fluids optimization scenario is selected, water is used as a coolant and oil is used as the to be cooled fluid. In the optimization scenarios with identical fluids, the material properties of both fluids is set to that of water. An optimization scenario with identical fluid is less realistic, since both fluids will have material properties evaluated at 293.15 [K] and the to be cooled fluid flows into the design domain at 333 [K].

Material Property	**Fluid 1, coolant (water)**	**Fluid 2, to be cooled fluid (oil)**	**Solid (aluminium)**
Density [kg/m^3]	998.2 (at 293.15 [K]) [21]	865 (SAE 10W-30) (313.15 [K]-373.15 [K]) [20]	2700 (at 296.15 [K]) [2]
Dynamic viscosity [N s m^2]	1.0042E-3 (at 293.15 [K]) [23]	0.02 (SAE 10W) (at 323.15 [K]) [22]	
Heat capacity (c_p) [J/(kg K)]	4182 (at 293.15 [K]) [24]	2306.12 (SAE 20W-50) (at 323.15 [K]) [26]	935 (at 296.15 [K]) [2]
Thermal conductivity [W/(m K)]	0.598 (at 293.15 [K]) [19]	0.135 (SAE 50) (at 328.15 [K]) [28]	244 (at 296.15 [K]) [2]
Specific Heat Ratio [-]	1.007 (at 293.15 [K]) [25]	1	

Table 3.3: Parameters used in the optimization algorithm.

3.4.5. Parameter Continuation

In the optimization model parameter continuation is used to sharpen the projection function and thereby decrease the intermediate material regions during the optimization process. The parameters used in the continuation scheme are the slope control parameters β_1, β_2 and β_3. The initial value selected for the slope control parameters is selected low to allow for more design freedom in the early phase of the optimization process. The β values are increased every n iterations, where n is a pre-specified number. The value for n is selected based on the number of iterations needed for the objective value to stabilize with the updated slope control parameters. In the set-up phase of the optimization model it was determined that around 20 iterations are needed for the objective value to stabilize. In all optimization scenarios in this report the value of n is set to 20. Fig. 3.19b shows the effect of the β increments on the shape of the interpolated thermal conductivity, the value of the slope control parameters is increased from 2 to 50. In every β increment the value of β_1, β_2 and β_3 is identical. The plot shows the normalized thermal conductivity interpolated for an optimization scenario with two different fluids. The same initial design is used as shown in Fig. 3.8a. The thermal conductivity in Fig. 3.19b is normalized with the thermal conductivity of the solid material 244 [W/(m K)]. A logartihmic y-scale is used to clearly distinguish between the thermal conductivity of the two different fluids. The normalized thermal conductivity is evaluated at the white line in Fig. 3.19a. The plot shows the reduction of the intermediate material regions with β increments, with every β increment the design becomes more discrete.

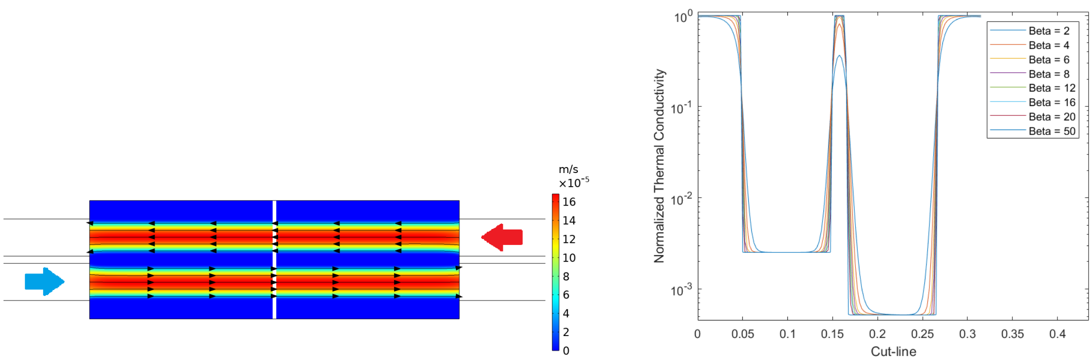

(a) Velocity field of an initial design with two straight fluid channels.

(b) The plot shows the normalized thermal conductivity, normalized with 244 [W/(m K)], evaluated at the white line in Fig. 3.19a for β values increased from 2 to 50.

Figure 3.19: The figure shows the normalized thermal conductivity evaluated in a two straight channel initial design for β values increased from 2 to 50. The values of β_1, β_2 and β_3 are identical in every β increment.

To find a suitable maximum β value for the projection filters, the objective and the pressure drop values of a discrete design are compared with the same values of an interpolated design. A discrete design is a design without material interpolation, filtering and projection. The design domain of the discrete and interpolated design has the same design domain size, mesh structure, mesh size, boundary conditions and makes use of identical material parameters. Fig. 3.20a and 3.20b show the temperature field of the discrete design (left) and the interpolated design (right) for $\beta_1 = \beta_2 = \beta_3 = 4$. In the parameter sweep the β values are increased from 4 to 100. In each β increment all slope control parameters have the same value $\beta_1 = \beta_2 = \beta_3$. The normalized objective and normalized pressure drop values corresponding to each β increment are plotted in Fig. 3.20c. The objective and pressure drop values are normalized with the corresponding objective and pressure drop values of the discrete design. The normalized objective and pressure drop values of the discrete design are also provided as a reference.

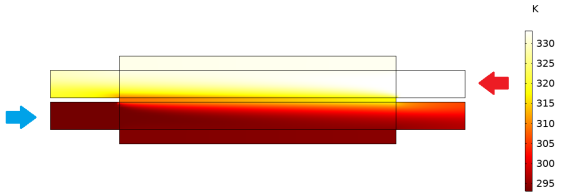

(a) Temperature field of the discrete design (reference design).

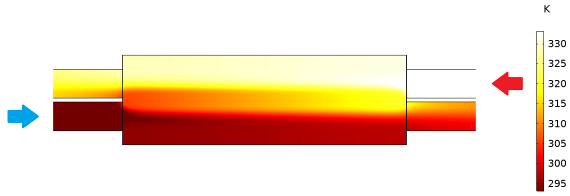

(b) Temperature field of the density=based design with $\beta_1 = \beta_2 = \beta_3 = 4$.

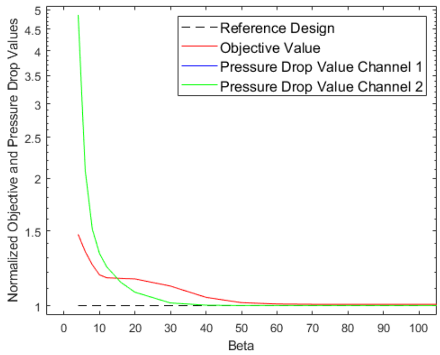

(c) Plot of objective value for different values of β compared to the reference objective. The blue line representing the pressure drop in channel 1 is not visible, since it is identical to the pressure drop in channel 2 and the green line therefore completely overlaps with the blue line.

Figure 3.20: Method to estimate a maximum β value that describes the physics accurately enough.

The physics of the discrete design significantly differ from the interpolated design for lower β values. However, for $\beta_1 = \beta_2 = \beta_3 > 60$, the objective and pressure drop values of the interpolated design approach the corresponding values of the discrete design. For $\beta_1 = \beta_2 = \beta_3 = 100$, the difference between the objective and pressure drop values of the discrete and the interpolated design becomes barely visible. The plot also shows that for lower β values, the physics are more sensitive for β increments. This means that the incremental scheme used for the slope control parmaeters should have a smaller step size for lower β value to ensure that the optimization algorithm remains stable while converging to an optimum. For higher β values the increments can have larger steps with less risk of convergence problems. The parameter continuation scheme needed for a stable convergence behaviour requires fine-tuning depending on the parameter values, design domain and boundary conditions used. The maximum β value (β_{max}), where $\beta_1 = \beta_2 = \beta_3 = \beta_{max}$, can be based on an acceptable difference between the discrete and interpolated design. If the number of iterations per β increment n, the β_{max} value and the step size of the β increments are determined, the total number of iterations can then be expressed as the amount of β increments multiplied with n.

3.4.6. Objective & Constraint Functions

In the variety of different optimization scenarios two objective functions are used. The first objective function is the boundary objective function found in literature [14]:

$$J_{temperature}(\Gamma_{in}, \Gamma_{out}) = \int_{\Gamma_{in}} (T(\mathbf{u}\cdot\mathbf{n}))d\Gamma_{in} - \int_{\Gamma_{out}} (T(\mathbf{u}\cdot\mathbf{n}))d\Gamma_{out}, \tag{3.28}$$

where T_{in} and T_{out} are the temperture distributions of the to be cooled fluid evaluated at the in- and outflow boundaries , u_{in} and u_{out} are the normal in- and outflow of the to be cooled fluid evaluated at the in- and outflow boundaries and Γ_{in} and Γ_{out} are the boundary integrals at the in- and outflow boundaries. The boundary objective function maximizes the normal velocity flow and temperature drop between the in- and outlet of the to be cooled fluid. Fig. 3.21 shows the boundaries where the boundary integrals Γ_{in} and Γ_{out} are evaluated. The boundary integrals are evaluated in the same locations in design domain types 1 and 2. The locations of Γ_{in} and Γ_{out} are flipped from left to right and vice versa, depending on the heat exchanger configuration selected, parallel- or counter-flow.

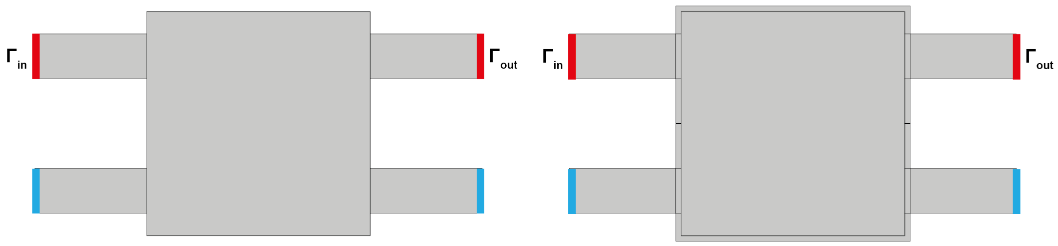

Figure 3.21: Boundaries where the boundary integralsΓ_{in} and Γ_{out} are evaluated. The locations of these boundaries are identical for design types 1 (left) and 2 (right).

The second objective function is a domain objective function found in the set-up phase of the optimization model:

$$J_{thermal}(\Omega) = \int_{\Omega} (k(\hat{\hat{\theta}}_1, \hat{\hat{\theta}}_2, \hat{\hat{\theta}}_3)(||\nabla T||)^2 + \rho_1 c_{p1} T(||\mathbf{u}_1|| \cdot ||\nabla T||) + \rho_2 c_{p2} T(||\mathbf{u}_2|| \cdot ||\nabla T||)) d\Omega, \tag{3.29}$$

where the first term is the conductive heat transfer term depending on the interpolated thermal conductivity $k(\hat{\hat{\theta}}_1, \hat{\hat{\theta}}_2, \hat{\hat{\theta}}_3)$ and temperature gradients ∇T. The second and third term are the convective heat transfer terms corresponding to fluid 1 and fluid 2. Each convective heat transfer term depends on the density ρ, heat capacity c_p, temperature field T, temperature gradients and flow velocity field $\mathbf{u}$ corresponding to the same fluid. An integral is taken of the three heat transfer terms in the active part of the design domain denoted with Ω. The domain objective function maximizes the conductive and convective heat transfer in the design domain. The details on the origin of the objective function and expansion in terms are provided in Appendix A. The domain objective function is evaluated in the active part of the design domain. Fig. 3.22 shows the active part of the design domain in both design domain types.

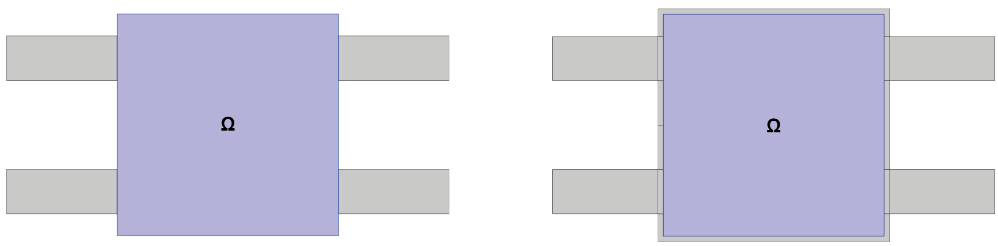

Figure 3.22: The domains where the domain objective function is evaluated is denoted with Ω in design types 1 (left) and 2 (right).

The boundary objective function is used in Chapter 4 and 5, while the domain objective function is used in Chapter 6, Chapter 7, Appendix B, Appendix C and Appendix D. The objective function formulation used in all optimization scenarios is a minimization formulation. The objective functions are normalized before being inverted:

$$\min_{\Omega \subset D} \qquad J(\Omega) = \left(\frac{J(\Omega)}{J_0(\Omega)} \right)^{-1}, \tag{3.30}$$

where $J(\Omega)$ is the boundary or domain objective function and $J_0(\Omega)$ is the reference objective value used for normalization. The value of $J_0(\Omega)$, in all optimization scenarios, is the objective function corresponding to $J(\Omega)$ evaluated in the initial design.

To limit the mechanical losses and constrain the optimization problem, pressure drop constraints are used. Two pressure drop constraints are used one for each fluid channel. The pressure drop constraint are formulated as inequality constraints:

$$g := \frac{|p_{in} - p_{out}|}{p_0 \cdot C_2} - 1 \leq 0, \tag{3.31}$$

where p_{in} and p_{out} are the average pressure values at the in- and outflow region of the design domain corresponding to the same fluid field. The absolute value of the difference in pressure drop between the in- and outlet is used in the constraint, so both a parallel- and counter-flow heat exchanger configuration can be used with the same constraint formulation. p_0 is the reference pressure drop used to normalize the constraint and is defined in the following manner:

$$p_0 = |p_{in} - p_{out}|, \tag{3.32}$$

where p_{in} and p_{out} are the average pressure values of a discrete design with straight fluid channels, as shown in Fig. 3.23. The average pressure values are evaluated at the boundaries as provided in Fig. 3.24. The absolute value of the average pressure difference is taken, so the formulation is valid for both a parallel- and counter-flow heat exchanger configuration. The reference pressure drop p_0 is defined with two straight fluid channels in every optimization scenario.

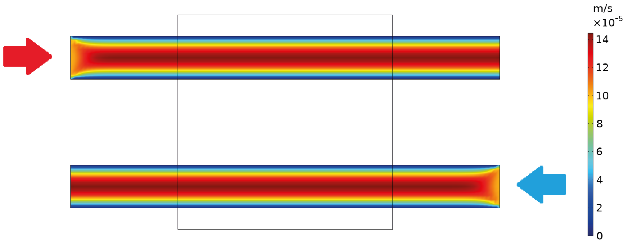

Figure 3.23: The reference design used to determine the values of $p_{0,1}$ (fluid 1) and $p_{0,2}$ (fluid 2).

C_2 is a parameter used to scale the maximum allowable pressure drop. Each constraint has a different scaling parameter $C_{2,1}$ for fluid channel 1 and $C_{2,2}$ for fluid channel 2, so the maximum allowable pressure drop can be controlled separately for each fluid channel. The average pressure value p_{in} and p_{out} are evaluated at the same boundaries in design domain types 1 and 2. Fig. 3.24 shows the boundaries where all average pressure values are evaluated in design domain type 1 (left) and design domain type 2 (right).

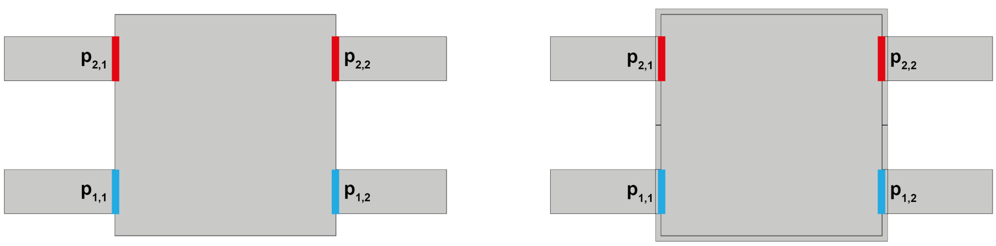

Figure 3.24: The boundaries where the average pressure value are evaluated in design domain types 1 (left) and 2 (right).

The optimization problem with all response functions is formulated in the following manner:

$$\begin{aligned} \min_{\Omega \subset D} \quad & J(\Omega) = \left(\frac{J_{thermal}(\Omega)}{J_0(\Omega)}\right)^{-1} \\ & g_1 := \frac{|p_{1,1} - p_{1,2}|}{C_{2,1} \cdot p_{0,1}} - 1 \leq 0 \\ & g_2 := \frac{|p_{2,1} - p_{2,2}|}{C_{2,2} \cdot p_{0,2}} - 1 \leq 0. \end{aligned} \tag{3.33}$$

The stopping criteria is a maximum number of iterations based on the β continuation scheme used. The maximum number of iterations can be computed as the total number of β values multiplied with the number of iterations in every β increments (n).

3.4.7. Software, Sensitivities & Update Method

The entire optimization model including the physics is created in Comsol and all results are generated with Comsol versions 5.6 and 6.0. During the thesis project Comsol was updated from version 5.6 to 6.0 and the license for version 5.6 was discontinued, therefore not all result could be generated with the same Comsol version. The sensitivities are computed by Comsol based on the response functions, filters and the field values of the physics. For the computation of the gradients the continuous adjoint method is used and the update method used is the gradient based globally convergent Method of Moving Asymptotes (MMA) [29]. For each outer iteration a single inner iteration is computed and the maximum number of iterations depends on the parameter continuations scheme selected.

4

2D Heat Exchanger: Non-Mixing Constraint

This chapter is dedicated to the verification of the optimization model and the proposed non-mixing constraint. In Section 4.1 the need for solid passive material regions enclosing the active part of the design domain is explained. In Section 4.2 the function used to approximate the filter radius R_3 with the minimum wall-thickness t_{min} is verified. In Section 4.3 the forming of a variable wall-thickness by the optimizer is elaborated on.

4.1. Passive Solid Material Regions

In both this chapter and Chapter 5 passive solid material regions are used to enclose the active part of the design domain, see Secton 3.4.3. The reason that these passive regions are used is to prevent the forming of fluid islands corresponding to one fluid within the fluid channel of the other fluid. An example of such a design is provided on the left-side in Fig. 4.1. Table 4.1 shows the values used for the dimensions of the design domain as shown in Fig. 3.14, the values used for the filtering and projection parameters and the values of the remaining parameters. During the optimization process, the value for β_1 and β_2 is increased from 8 to 80 and β_3 is increased from 2 to 80. By setting the initial value of β_3 to 2, the non-mixing region is gradually introduced into the design during the optimization process. The lower limit for β_1 and β_2 is set to 8, since these parameters have less influence on the shape of the non-mixing region. The upper limit, β_{max}, for β_1, β_2 and β_3 is set to 80 based on the method to estimate a suitable β_{max} value as provided in Section 3.4.5. The incremental schemes used are $\beta_1 = \beta_2 = 8, 8, 8, 8, 10, 12, 14, 16, 18, 20, 24, 28, 32, 36, 40, 50, 60, 70, 80$ and $\beta_3 = 2, 4, 6, 8, 10, 12, 14, 16, 18, 20, 24, 28, 32, 36, 40, 50, 60, 70, 80$. The β parameters are updated every 20 iterations ($n = 20$).

Dimensional Parameters	Values	Filter and Projection Parameters	Values	Parameters	Values
L1	1 [m]	R_1	0.03 [m]	h	0.01 [m]
L2	0.315[m]	β_1	8-80 [-]	$T_{in,f1}$	293.15 [K]
L3	0.05 [m]	R_2	0.03 [m]	$T_{in,f2}$	333.15 [K]
L4	0.1 [m]	β_2	8-80 [-]	Re_1	10 [-]
L5	0.015 [m] (t_{min})	t_{min}	0.015 [m]	Re_2	10 [-]
L6	0.25 [m]	β_3	8-80 [-]	C_1	500 [-]
L7 (only with passive - solid material regions)	0.025 [m]			C_2	3 [-]

Table 4.1: Parameter values used in optimization scenarios.

The enclosed fluid region is visible in Fig. 4.1c and 4.1e (upper boundary left of the vertical centerline in the design domain). The non-mixing constraint will separate the two different fluids in all location of the design domain with a non-mixing region, thus the fluid region is separated from the fluid channel corresponding to the other fluid with the minimum wall-thickness (t_{min}). The flow velocity field shows that the enclosed fluid region is stagnant, see Fig. 4.1a. Even though the non-mixing constraint prevents the forming of mixing heat exchanger designs, the enclosed fluid regions are undesirable since they are difficult to manufacture. Such a heat exchanger design requires the placement of a fluid in an enclosed hollow solid material volume during or after manufacturing of the heat exchanger. The enclosed fluid regions are formed at the adiabatic boundaries during the optimization process when the optimization algorithm starts generating a new material region at these adiabatic boundaries. Instead of forming a completely solid material region with the first design variable $\hat{\tilde{\theta}}_1$, it generates a fluid region corresponding to the other fluid that is then separates with the non-mixing filter ($\hat{\tilde{\theta}}_3$).

The forming of these enclosed fluid regions was only noticed at the adiabatic boundaries and can be compensated for using passive solid material regions enclosing the active part of the design domain. These passive solid material regions prevent the forming of enclosed fluid regions at the adiabatic boundaries, but the optimization algorithm can still form these enclosed fluid regions in other regions in the active part of the design domain. The same optimization scenario as used to create the optimal design on the left-side in Fig. 4.1 is also computed with the passive solid material regions surrounding the active part of the design domain and is provided on the right-side in Fig. 4.1. The optimal design generated with the passive solid material regions does not have enclosed fluid regions at the boundaries. The forming of these enclosed fluid regions never occured in other regions of the design domain. The enclosed fluid regions are likely not formed since they do not contribute in an advantageous manner to the optimization objective. The fluid regions are stagnant, so the heat transfer in these regions is only conductive heat transfer. The thermal conductivity of the fluids is lower than that of the solid material. The total heat transfer in a design with a completely solid material region instead of an enclosed fluid region is higher.

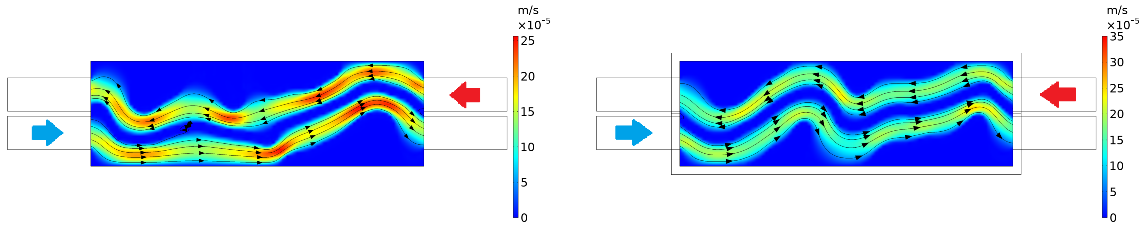

(a) Velocity field without passive solid regions. (b) Velocity field with passive solid regions.

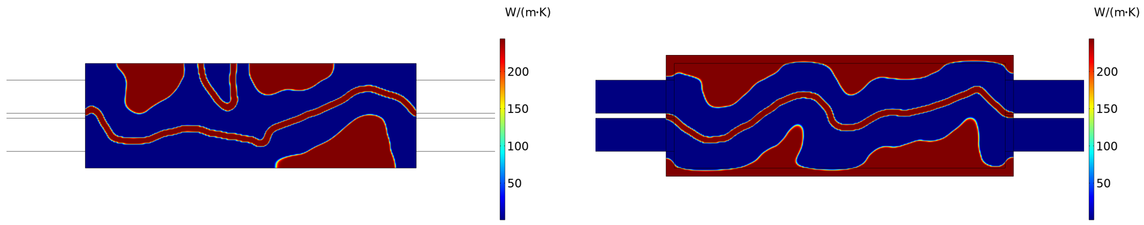

(c) Thermal Conductivity field without passive solid regions. (d) Thermal Conductivity field with passive solid regions.

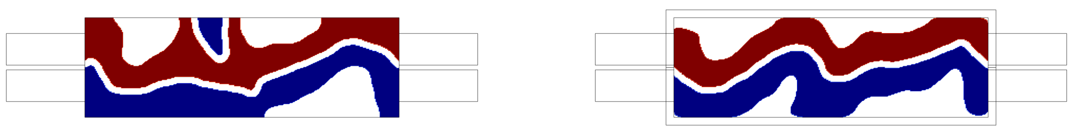

(e) Fluid regions corresponding to each fluid without passive solid regions. Fluid 1 is presented in blue and fluid 2 is presented in red. (f) Fluid regions corresponding to each fluid with passive solid regions. Fluid 1 is presented in blue and fluid 2 is presented in red.

Figure 4.1: Optimal design with enclosed fluid region formed within the fluid channel of the other fluid.

The enclosed fluid regions were only formed with the boundary objective function (Eq. 3.28) and the passive solid material regions are therefore only used in the optimization scenarios with the boundary objective function. The forming of these enclosed fluid regions could originate from the gradient information taken into account. The boundary objective function only integrates over the in- and outflow boundaries of the to be cooled fluid, the local gradient information at the adiabatic boundaries is indirectly taken into account. The domain objective function (Eq. 3.29) integrates over the entire active part of the design domain including the adiabatic boundaries, the local gradient information at the adiabatic boundaries is therefore directly taken into account.

4.2. Minimum Wall-Thickness

In this section the minimum wall-thickness t_{min} is varied to determine its influence on the optimization process. In addition, the pre-set t_{min} value and the actual minimum wall-thickness generated by the optimizer are compared. For this optimization problem two identical fluids, water, are used with a counter-flow heat exchanger configuration. Table 4.2 shows the values used for the dimensions of the design domain as shown in Fig. 3.14, the values used for the filtering and projection parameters and the values of the remaining parameters. During the optimization process, the value for β_1 and β_2 is increased from 8 to 80 and β_3 is increased from 2 to 80. By setting the initial value of β_3 to 2, the non-mixing region is gradually introduced into the design during the optimization process. The lower limit for β_1 and β_2 is set to 8, since these parameters have less influence on the shape of the non-mixing region. The upper limit, β_{max}, for β_1, β_2 and β_3 is set to 80 based on the method to estimate a suitable β_{max} value as provided in Section 3.4.5. The incremental schemes used are $\beta_1 = \beta_2 = 8, 8, 8, 8, 10, 12, 14, 16, 18, 20, 24, 28, 32, 36, 40, 50, 60, 70, 80$ and $\beta_3 = 2, 4, 6, 8, 10, 12, 14, 16, 18, 20, 24, 28, 32, 36, 40, 50, 60, 70, 80$. The β parameters are updated every 20 iterations ($n = 20$). For the minimum wall-thickness (t_{min}) a parameter sweep is performed with the values 0.015 [m], 0.020 [m] and 0.025 [m]. The reason for selecting these values for the minimum wall-thickness is that the difference between the t_{min} values is large enough to be visible in the designs. The flow penalization scaling term C_1 is set to 500. The value for the flow penalization scaling term is determined with an approach to verify the robustness of the non-mixing consteraint as provided in Appendix B.

Dimensional Parameters	**Values**	**Filter and Projection Parameters**	**Values**	**Parameters**	**Values**
L1	1 [m]	R_1	0.03 [m]	h	0.01 [m]
L2	0.315[m]	β_1	8-80 [-]	$T_{in,f1}$	293.15 [K]
L3	0.05 [m]	R_2	0.03 [m]	$T_{in,f2}$	333.15 [K]
L4	0.1 [m]	β_2	8-80 [-]	Re_1	10 [-]
L5	0.015 [m] (t_{min})	t_{min}	0.015 [m]	Re_2	10 [-]
L6	0.25 [m]	β_3	2-80 [-]	C_1	500 [-]
L7	0.025 [m]			C_2	3 [-]

Table 4.2: Parameter values used in optimization scenarios.

Fig. 4.2 shows the velocity fields of the optimal results generated with $t_{min} = 0.015$ [m] (Fig. 4.2a), $t_{min} = 0.020$ [m] (Fig. 4.2b) and $t_{min} = 0.025$ [m] (Fig. 4.2c).

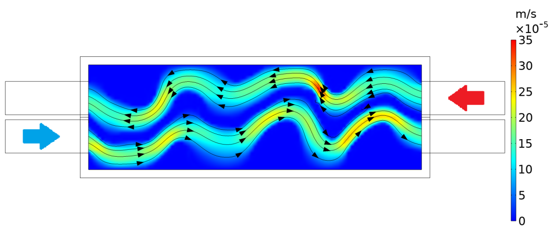

(a) Velocity field of the optimal design generated with $t_{min} = 0.015$ [m].

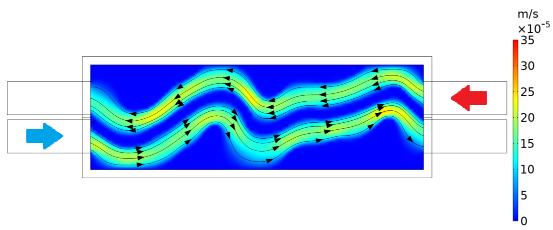

(b) Velocity field of the optimal design generated with $t_{min} = 0.020$ [m].

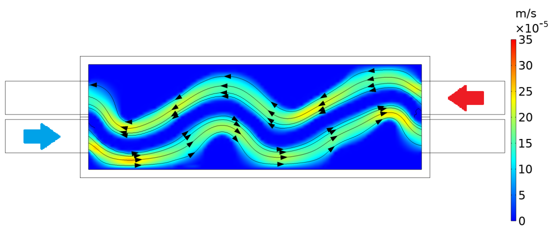

(c) Velocity field of the optimal design generated with $t_{min} = 0.025$ [m].

Figure 4.2: Velocity fields of the optimal designs generated with $t_{min} = 0.015$ [m], $t_{min} = 0.020$ [m] and $t_{min} = 0.025$ [m].

In all scenarios a tortuous fluid channel is generated to elongate the fluid channels and improve the heat transfer. The non-mixing constraint separates the fluid channels with a solid material region in all optimal designs. The optimization algorithm did not generate a variable wall-thickness in any of the optimal designs, this can be explained by the fact that a thin wall allows for a more advantageous heat transfer in this optimization scenario. The legends all have the same lower and upper limit to compare the velocity fields. The velocity magnitude in the fluid channels is similar in all the optimal designs, with a slightly increased flow velocity in and near the curved sections of the fluid channels. The optimal design generated with t_{min} = 0.015 [m] has fluid channels with an on average smaller diameter and the fluid channels are further elongated within the design domain. The optimal designs generated with t_{min} = 0.020 [m] and t_{min} = 0.025 [m] have a similar fluid channel geometry and velocity fields. Selecting a lower value for t_{min} allows for more design freedom, since the non-mixing region will occupy a smaller portion of the design domain. Fig. 4.3 shows the thermal conductivity fields corresponding to the same optimal designs. The thermal conductivity fields are used to more clearly show the material regions of the fluids (blue regions with $k = 0.598$ [W/(mK)]) and the solid material (red regions with $k = 244$ [W/(mK)]).

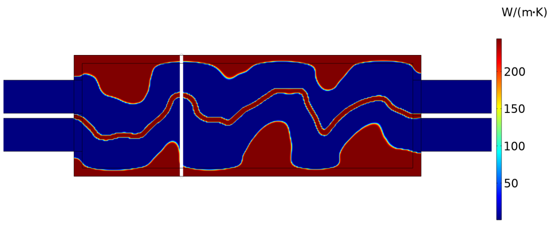

(a) Thermal conductivity field of the optimal design generated with t_{min} = 0.015 [m].

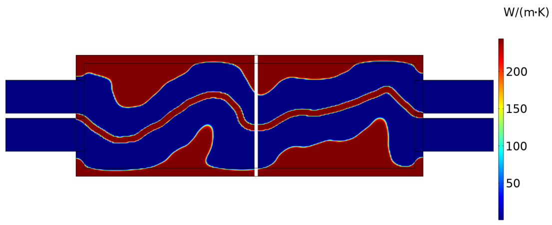

(b) Thermal conductivity field of the optimal design generated with t_{min} = 0.020 [m].

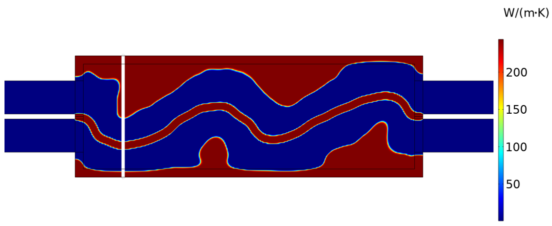

(c) Thermal conductivity field of the optimal design generated with t_{min} = 0.025 [m].

Figure 4.3: Thermal conductivity fields of the optimal designs generated with t_{min} = 0.015 [m], t_{min} = 0.020 [m] and t_{min} = 0.025 [m].

To determine if the actual minimum wall-thickness generated by the optimizer is increased with an increased t_{min} value and if the generated wall-thickness is near the t_{min} value, the minimum wall-thickness is evaluated in the design domain. Fig. 4.4 shows the cross-sections of the non-mixing regions evaluated at the white lines in the corresponding optimal designs provided in Fig. 4.3. The non-mixing constraint allows for a variable wall-thickness generated with the first design variable ($\hat{\tilde{\theta}}_1$) combined with the minimum wall-thickness generated with the non-mixing variable ($\hat{\tilde{\theta}}_3$). To determine the location where the wall-thickness is the minimum wall-thickness, the locations where only the non-mixing variable is active should be evaluated. The fluid channels in all three optimal designs are separated with only the minimum wall-thickness generated with the non-mixing variable. Since the non-mixing region consists of a solid material region generated with the non-mixing variable only, the non-mixing region can be sliced in all location in the design domain to determine the generated minimum wall-thickness. The non-mixing region has to be sliced perpendicular to the centre line of the non-mixing region generated with the non-mixing variable to measure the actual minimum wall-thickness. Determining the location where to slice the non-mixing region for the cross-section is done manually, since the computation of the thickness of the non-mixing region is not included in the optimization model. This can influence the accuracy of the measurement. Fig. 4.4a shows the cross-section of the optimal design generated with t_{min} = 0.015 [m] evaluated at the white line in Fig. 4.3a. The measured minimum wall-thickness is 0.0168 [m]. Fig. 4.4b shows the cross-section of the optimal design generated with t_{min} = 0.020 [m] evaluated at the white line in Fig. 4.3b. The measured minimum wall-thickness is 0.0206 [m]. Fig. 4.4c shows the cross-section of the optimal design generated with t_{min} = 0.025 [m] evaluated at the white line in Fig. 4.3c. The measured minimum wall-thickness is 0.0247 [m].

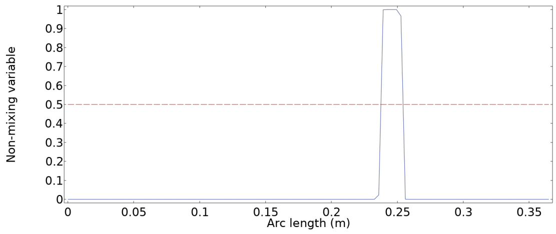

(a) Cross-section of the non-mixing region generated with t_{min} = 0.015 [m] evaluated at white line in Fig. 4.3a. The measured minimum wall-thickness is 0.0168 [m].

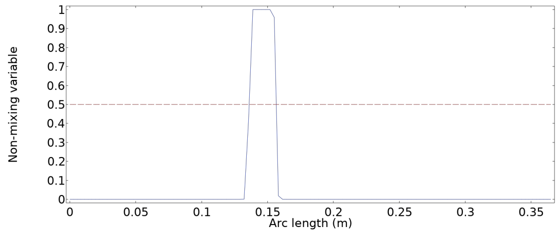

(b) Cross-section of the non-mixing region generated with t_{min} = 0.020 [m] evaluated at white line in Fig. 4.3b. The measured minimum wall-thickness is 0.0206 [m].

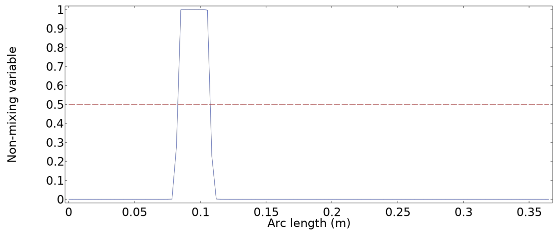

(c) Cross-section of the non-mixing region generated with t_{min} = 0.025 [m] evaluated at white line in Fig. 4.3c. The measured minimum wall-thickness is 0.0247 [m].

Figure 4.4: Cross-sections of the non-mixing regions defined with $\hat{\hat{\theta}}_3$.

The pre-set minimum wall-thicknesses selected for t_{min} and the measured minimum wall-thicknesses have values that are quite close. The difference between the pre-set and measured values can be explained by manually determining the location where the non-mixing region is sliced for a cross-section and manual measurement of the non-mixing region. It is also visible that increasing t_{min} will result in designs with an increased minimum wall-thickness. However, when the minimum wall-thickness is altered the region available for folding the fluid channels is also altered. To some extent this is expected since a design with a wall-thickness thinner than the minimum wall-thickness cannot be generated, therefore when the wall-thickness is increased the previous design can not be generated.

4.3. Variable Wall-Thickness

In this section the approach applied by the optimization algorithm to generate a variable wall-thickness with the non-mixing constraint is examined. A solid domain can be defined with the first design variable $\hat{\hat{\theta}}_1$ as the regions where $\hat{\hat{\theta}}_1 = 1$ or as the regions where the non-mixing filter is active and $\hat{\hat{\theta}}_3 = 1$. A wall with a variable thickness ($t_{wall} > t_{min}$) seperating the two fluids is thus constructed by adding solid material ($\hat{\hat{\theta}}_1 = 1$) around the minimum wall-thickness generated by the non-mixing constraint ($\hat{\hat{\theta}}_3 = 1$).

To show the approach the optimizer uses to generate a variable wall-thickness, an optimization scenario is analysed where a variable wall-thickness is clearly visible. The heat exchanger configuration used in this optimization scenario is a counter-flow configuration with two identical fluids, both fluids are water. The coolant flows into the design domain on the right-side, while the to be cooled fluid flows into the design domain on the left-side. Table 4.3 shows the values used for the dimensions of the design domain as shown in Fig. 3.14, the values used for the filtering and projection parameters and the values of the remaining parameters. During the optimization process the value for β_1, β_2 and β_3 are increased from 8 to 80. The lower limit for β_1, β_2 and β_3 is set to 8, because the bandpass projection function is active between 0 and 1 for $\beta_3 \geq 8$ (see Section 3.3.1). The upper limit, β_{max}, for β_1, β_2 and β_3 is set to 80 based on the method to estimate a suitable β_{max} value as provided in Section 3.4.5. The incremental scheme used for the β parameters is $\beta_1 = \beta_2 = \beta_3 = 8, 10, 12, 14, 16, 18, 20, 24, 28, 32, 36, 40, 50, 60, 70, 80$. The β parameters are updated every 20 iterations ($n = 20$).

Dimensional Parameters	Values	Filter and Projection Parameters	Values	Parameters	Values
L1	0.5 [m]	R_1	0.015 [m]	h	0.005 [m]
L2	0.5 [m]	β_1	8-80 [-]	$T_{in,f1}$	293.15 [K]
L3	0.05 [m]	R_2	0.015 [m]	$T_{in,f2}$	333.15 [K]
L4	0.1 [m]	β_2	8-80 [-]	Re_1	5 [-]
L5	0.2 [m]	t_{min}	0.05 [m]	Re_2	5 [-]
L6	0.25 [m]	β_3	8-80 [-]	C_1	500 [-]
L7	0.025 [m]			C_2	2 [-]

Table 4.3: Parameter values used in optimization scenarios.

Fig. 4.5 shows an optimal design with a variable wall-thickness. The variable wall-thickness allows for further elongation of the fluid channels as is visible on the left-side above the inflow boundary of the coolant in Fig. 4.5b. The total solid material region is provided in Fig. 4.5b, the solid material region is here expressed with the thermal conductivity. The solid material region shows a variable wall-thickness separating the two fluids. The solid regions generated with $\hat{\tilde{\theta}}_1$ are shown in Fig. 4.5c and the solid region generated with $\hat{\tilde{\theta}}_3$ (non-mixing variable) is shown in Fig. 4.5d. The figures show that $\hat{\tilde{\theta}}_3$ guarantees the minimum wall-thickness between the fluids and $\hat{\tilde{\theta}}_1$ can generated overlapping or touching solid material regions to form the variable wall-thickness.

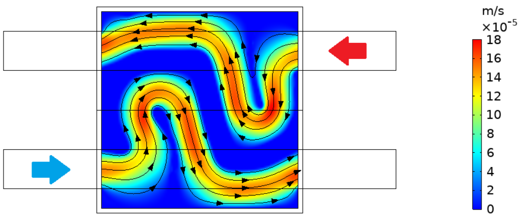

(a) Velocity field optimal design.

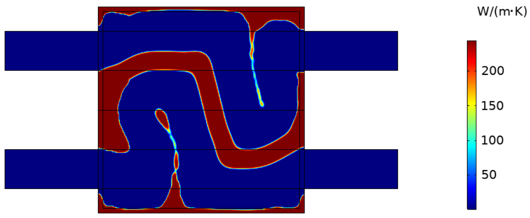

(b) Total region of solid material expressed with the thermal conductivity.

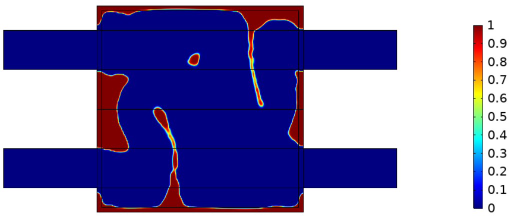

(c) Solid region generated by the first design variable ($\hat{\tilde{\theta}}_1$).

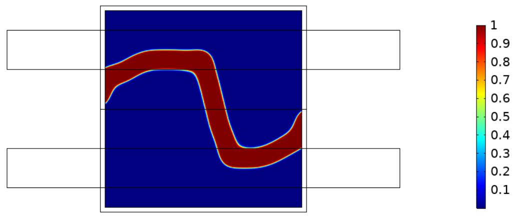

(d) Solid region generated by the non-mixing design variable ($\hat{\tilde{\theta}}_3$).

Figure 4.5: The interpolation functions allow the wall-thickness to vary, while a minimum wall-thickness is guaranteed.

The small solid island, floating near the center of the design domain, in Fig. 4.5c is a remainder from a solid region that was initially connected to the solid region on the right side of the island. The non-mixing constraint generates a solid region in the same location as the solid island, thereby connecting the solid island to the other solid regions, see Fig. 4.5b.

In the set-up phase of the optimization algorithm it was noticed that the optimizer can form a variable wall-thickness more easily if in the initial design a solid material region defined with $\hat{\tilde{\theta}}_1$ is available surrounding the non-mixing region defined with $\hat{\tilde{\theta}}_3$. Fig. 4.6 shows a similar initial design as used in the previous optimization scenario (Fig. 4.5), where the variable wall-thickness is formed. The initial solid region defined with θ_1 is shown in Fig. 4.6a and the initial solid region defined with $\hat{\tilde{\theta}}_3$ is shown in Fig. 4.6b (non-mixing region). In such an optimization scenario, the initial design has a solid region between the fluids that is larger than the minimum wall-thickness ($t_{wall} > t_{min}$).

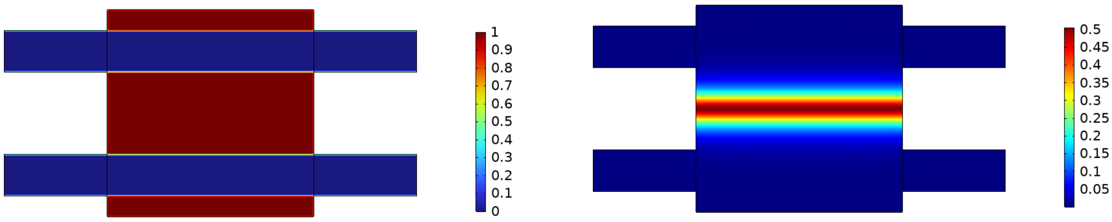

(a) Initial design for θ_1 used with approach 1, where the solid region is marked in red and the fluid regions marked in blue.

(b) Initial region defined with $\hat{\hat{\theta}}_3$ with $\beta = 2$.

Figure 4.6: Optimizer perference for approach 1 to generate variable wall-thickness.

In an optimization scenario where the initial design is defined as $t_{wall} < t_{min}$, the optimizer has a preference for forming design with a minimum wall-thickness. Fig. 4.7 shows such an initial design. The solid material region defined with θ_1 is shown in Fig. 4.7a, while the solid region defined with $\hat{\hat{\theta}}_3$ is shown in Fig. 4.7b. Similar initial design were used in the results in Section 4.2, where the optimizal designs show a wall-thickness near the pre-set minimum wall-thickness.

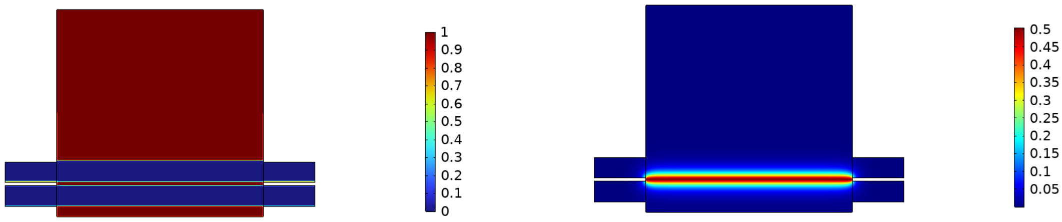

(a) Initial design for θ_1 used with approach 1, where the solid region is marked in red and the fluid regions marked in blue.

(b) Initial region defined with $\hat{\hat{\theta}}_3$ with $\beta = 2$.

Figure 4.7: Optimizer perference for approach 1 to generate variable wall-thickness.

The optimizer seems to add or remove solid material defined with $\hat{\hat{\theta}}_1$ more easily if initially solid material regions defined with $\hat{\hat{\theta}}_1$ are available. The same optimization scenarios are also computed with the domain objective function as provided in Eq. 3.29, these optimal results and analysis of the results are provided in Appendix C.

5

2D Heat Exchanger: Interpolation Functions

In this chapter, the interpolation functions used in the proposed optimization model are compared to the interpolation functions used by Papazoglou (2015) [14].

5.1. Interpolation Functions

The proposed interpolation functions have similar terms as the interpolation functions from literature. In this section the proposed interpolation functions are compared to the interpolation functions from literature. The interpolation functions used in literature are provided in Eq. 5.1 and 5.2.

$$\alpha_1(\hat{\hat{\theta}}_1, \hat{\hat{\theta}}_2) = a_{1,max}\left(1 - (1 - \hat{\hat{\theta}}_1^p)(1 - \hat{\hat{\theta}}_2^p)\right), \tag{5.1}$$

$$\alpha_2(\hat{\hat{\theta}}_1, \hat{\hat{\theta}}_2) = a_{2,max}\left(1 - (1 - \hat{\hat{\theta}}_1^p)(1 - (1 - \hat{\hat{\theta}}_2)^p)\right). \tag{5.2}$$

The proposed interpolation functions are already provided in Section 3.3.2, but are provided here in Eq. 5.3 and 5.4 for comparison with the interpolation functions from literature.

$$\alpha_1(\hat{\hat{\theta}}_1, \hat{\hat{\theta}}_2, \hat{\hat{\theta}}_3) = a_{1,max}\left(1 - (1 - \hat{\hat{\theta}}_1^p)(1 - \hat{\hat{\theta}}_2^p)(1 - \hat{\hat{\theta}}_3^p)\right), \tag{5.3}$$

$$\alpha_2(\hat{\hat{\theta}}_1, \hat{\hat{\theta}}_2, \hat{\hat{\theta}}_3) = a_{2,max}\left(1 - (1 - \hat{\hat{\theta}}_1^p)(1 - (1 - \hat{\hat{\theta}}_2)^p)(1 - \hat{\hat{\theta}}_3^p)\right), \tag{5.4}$$

The drawback of the interpolation functions found in literature is that a zero wall-thickness can be generated. The proposed interpolation functions guarantee a minimum wall-thickness, while also being able to generate a variable wall-thickness in a similar manner. The interpolation function for the thermal conductivity in literature:

$$k(\hat{\hat{\theta}}_1) = k_f + k_s\hat{\hat{\theta}}_1^p, \tag{5.5}$$

does not distinguish between two different fluids. Both two identical and different fluids are used in this chapter, therefore the two different fluid thermal conductivity interpolation function is used in all optimization scenarios:

$$k(\hat{\hat{\theta}}_1, \hat{\hat{\theta}}_2, \hat{\hat{\theta}}_3) = k_1 + (k_s - k_1)\hat{\hat{\theta}}_1^p + (k_s - k_1)(1 - \hat{\hat{\theta}}_1^p)\hat{\hat{\theta}}_3^p + (k_2 - k_1)(1 - \hat{\hat{\theta}}_1^p)(1 - \hat{\hat{\theta}}_3^p)\hat{\hat{\theta}}_2^p. \tag{5.6}$$

In the optimization scenarios with the interpolation functions from literature, the non-mixing variable $\hat{\hat{\theta}}_3$ is set to 0 and the interpolation function used for the thermal conductivity simplifies to:

$$k(\hat{\hat{\theta}}_1, \hat{\hat{\theta}}_2) = k_1 + (k_s - k_1)\hat{\hat{\theta}}_1^p + (k_2 - k_1)(1 - \hat{\hat{\theta}}_1^p)\hat{\hat{\theta}}_2^p. \tag{5.7}$$

The goal of this chapter is to determine if the proposed interpolation functions alter the optimization behaviour significantly. In both optimization problems a counter-flow heat exchanger configuration is used.

The coolant flows into the design domain at the left-side, while the to be cooled fluid flows into the design domain at the right-side. Table 5.1 shows the values used for the dimensions of the design domain as shown in Fig. 3.14, the values used for the filtering and projection parameters and the values of the remaining parameters. During the optimization process, the value for β_1 and β_2 is increased from 8 to 80 and β_3 is increased from 2 to 80. By setting the initial value of β_3 to 2, the non-mixing region is gradually introduced into the design during the optimization process. The lower limit for β_1 and β_2 is set to 8, since these parameters have less influence on the shape of the non-mixing region. The upper limit, β_{max}, for β_1, β_2 and β_3 is set to 80 based on the method to estimate a suitable β_{max} value as provided in Section 3.4.5. The incremental schemes used are $\beta_1 = \beta_2 = 8, 8, 8, 8, 10, 12, 14, 16, 18, 20, 24, 28, 32, 36, 40, 50, 60, 70, 80$ and $\beta_3 = 2, 4, 6, 8, 10, 12, 14, 16, 18, 20, 24, 28, 32, 36, 40, 50, 60, 70, 80$. The β parameters are updated every 20 iterations ($n = 20$). The two sets of interpolation functions are compared for an optimizaiton scenario with two identical fluids and two different fluids.

Dimensional Parameters	**Values**	**Filter and Projection Parameters**	**Values**	**Parameters**	**Values**
L1	1 [m]	R_1	0.03 [m]	h	0.01 [m]
L2	0.315[m]	β_1	8-80 [-]	$T_{in,f1}$	293.15[K]
L3	0.05 [m]	R_2	0.03 [m]	$T_{in,f2}$	333.15[K]
L4	0.1 [m]	β_2	8-80 [-]	Re_1	10 [-]
L5	0.015 [m] (t_{min})	t_{min}	0.015 [m]	Re_2	10 [-]
L6	0.25 [m]	β_3	2-80 [-]	C_1	500 [-]
				C_2	3 [-]

Table 5.1: Parameter values used in optimization scenarios.

5.1.1. Two Identical Fluid Optimization

In the identical fluids optimization scenario, both fluids derive their material properties from water. The optimal results generated with the interpolation functions from literature are compared to the optimal results generated with the proposed interpolation functions in Fig. 5.1. The fields of the optimal design generated with the interpolation functions from literature are provided on the left-side in Fig. 5.1 (5.1a, 5.1c and 5.1e). The optimal design has a geometry with fluid channels that are not separated with a solid material region in the entire design domain. If such an optimal design would be manufactured the fluids would mix. The objective and thermal efficiency value of the optimal design are $1.0191E-4$ [m^2 K/s] and 26.941%. The fields of the optimal design generated with the proposed interpolation functions are provided on the right-side in Fig. 5.1 (Fig. 5.1b, 5.1d and 5.1f). The non-mixing constraint prevents mixing of the two fluids as shown in Fig. 5.1f. The wall-thickness has an almost constant thickness in the entire design domain apart from the folded non-mixing region near the center of the design domain. To investigate the locally generated wall-thickness, a cross-section of the non-mixing region is analysed. The local wall-thickness in the optimal design is evaluated at the white line in Fig. 5.1b and has a wall-thickness of approximately 0.0159[m], which is near to the pre-set minimum wall-thickness $t_{min} = 0.015$[m]. The design has to be sliced perpendicular to the centerline of the non-mixing region to accurately measure the wall-thickness. This operation is performed manually and could give slight deviations between the measured and actual wall-thickness. The objective and thermal efficiency value of the optimal design are $1.1428E-4$ [m^2 K/s] and 30.128%.

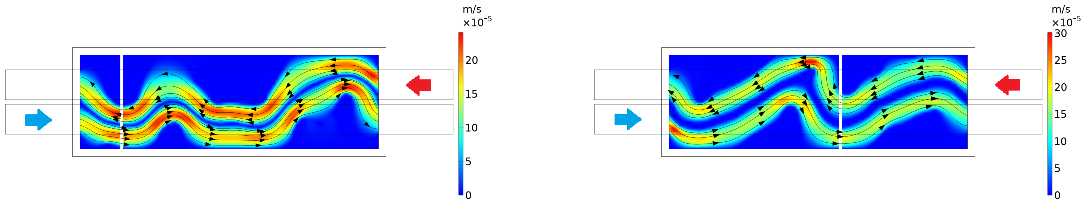

(a) Velocity field (interpolation functions from literature).

(b) Velocity field (proposed interpolation functions).

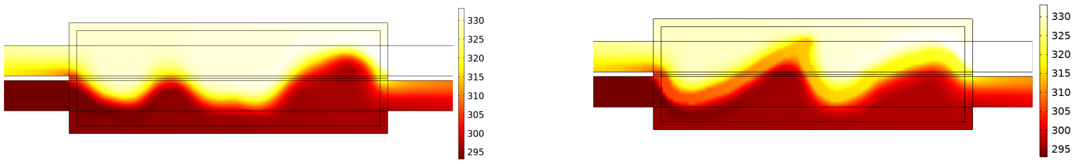

(c) Temperature field, with an objective value of $1.0191E-4$ [m^2 K/s] and a thermal efficiency value of 26.941% (interpolation functions from literature).

(d) Temperature field, with an objective value of $1.1428E-4$ [m^2 K/s] and a thermal efficiency value of 30.128% (proposed interpolation functions).

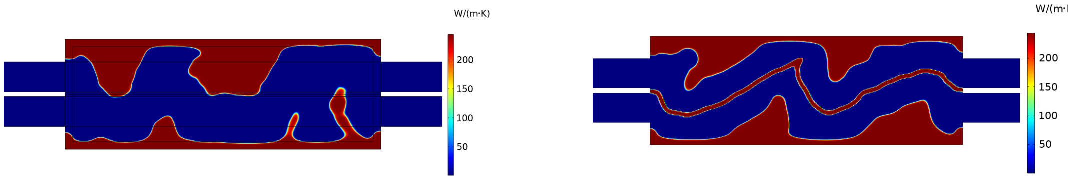

(e) Thermal conductivity field (interpolation functions from literature).

(f) Thermal conductivity field (proposed interpolation functions).

Figure 5.1: Optimal results generated with the two sets of interpolation functions. The fields of the optimal result generated with the interpolation functions from literature are provided on the left-side, while the fields of the optimal result generated with the proposed interpolation functions are provided on the right-side.

To check if the fluid flow is correctly penalized, the normalized velocity fields of both fluids are plotted in Fig. 5.2. The velocity fields are evaluated at the white line in Fig. 5.1a and 5.1b. Fig. 5.2a shows the plot of the normalized velocity fields generated with the interpolation functions from literature. Fig. 5.2b shows the plot of the normalized velocity fields generated with the proposed interpolation functions. In both plots the normalized thermal conductivities are also plotted to show the solid material regions. Both Fig. 5.2a and 5.2b show optimal designs that have small overlapping material regions. The overlapping material regions in the non-mixing region are relatively large compared to the total size of the non-mixing region. The reason for the relatively large overlapping regions is the small minimum wall-thickness. For a t_{min} value in the range of the filter radii size of R_1 and R_2, the region with intermediate values is relatively large compared to the total size of the non-mixing region when the wall-thickness approaches the minimum wall-thickness t_{min}. The size of the overlapping material regions can be reduced by further increasing the β values.

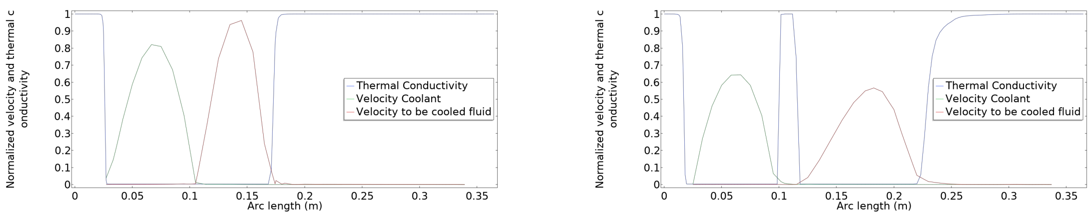

(a) Normalized cross-section of the design generated with the interpolation functions from literature. The velocity fields are normalized with $2.41E-4$[m/s] (maximum flow velocity) and the thermal conductivity is normalized with 244[W/mK] (thermal conductivity of the solid material k_s).

(b) Normalized cross-section of the design generated with the proposed interpolation functions. The velocity fields are normalized with $3.01E-4$[m/s] (maximum flow velocity) and the thermal conductivity is normalized with 244[W/mK] (thermal conductivity of the solid material k_s).

Figure 5.2: Comparing overlapping regions in the designs generated with the two sets of interpolation functions.

The optimal designs generated with each set of interpolation functions show that the proposed non-mixing constraint prevents the forming of a mixing heat exchanger design, while a mixing heat exchanger design could be preferred by the optimization algorithm. The non-mixing constraint forces the optimization algorithm to form different design and the proposed non-mixing constraint therefore significantly alters the optimization behaviour.

5.1.2. Two Different Fluids Optimization

In the different fluids optimization scenario, the coolant has material properties in the range of water and the to be cooled fluid has material properties in the range of oil. The optimal results generated with the interpolation functions from literature are compared to the optimal results generated with the proposed interpolation functions in Fig. 5.3. The fields of the optimal design generated with the interpolation functions from literature are provided on the left-side in Fig. 5.3 (Fig. 5.3a, 5.3c and 5.3e). The optimal result generated with the interpolation functions from literature shows a design with expanded fluid channels that are narrowed on the right-side of the design domain. The fluid channels are placed next to each other in the entire design domain apart from a small solid island on the right-side of the design domain as shown in Fig. 5.3e. The objective and thermal efficiency value of the optimal design are $1.3506E-4$ [m^2 K/s] and 36.282%. The fields of the optimal design generated with the proposed interpolation functions are provided on the right-side in Fig. 5.3 (Fig. 5.3b, 5.3d and 5.3f). The non-mixing constraint prevents mixing of the two fluids with a non-mixing region that has an almost constant thickness. To investigate the locally generated wall-thickness, a cross-section of the non-mixing region is analysed. The local wall-thickness in the optimal design is evaluated at the white line in Fig. 5.3b and has a wall-thickness of approximately 0.0149[m], which is near to the pre-set minimum wall-thickness $t_{min} = 0.015$[m]. The evaluated wall thickness deviates from the pre-set minimum wall-thickness of $t_{min} = 0.015$[m]. The reason for the deviation from the pre-set minimum wall-thickness can to some extent be explained by the manual measuring of the non-mixing region. The objective and thermal efficiency value of the optimal design are $1.1786E-4$ [m^2 K/s] and 31.970%.

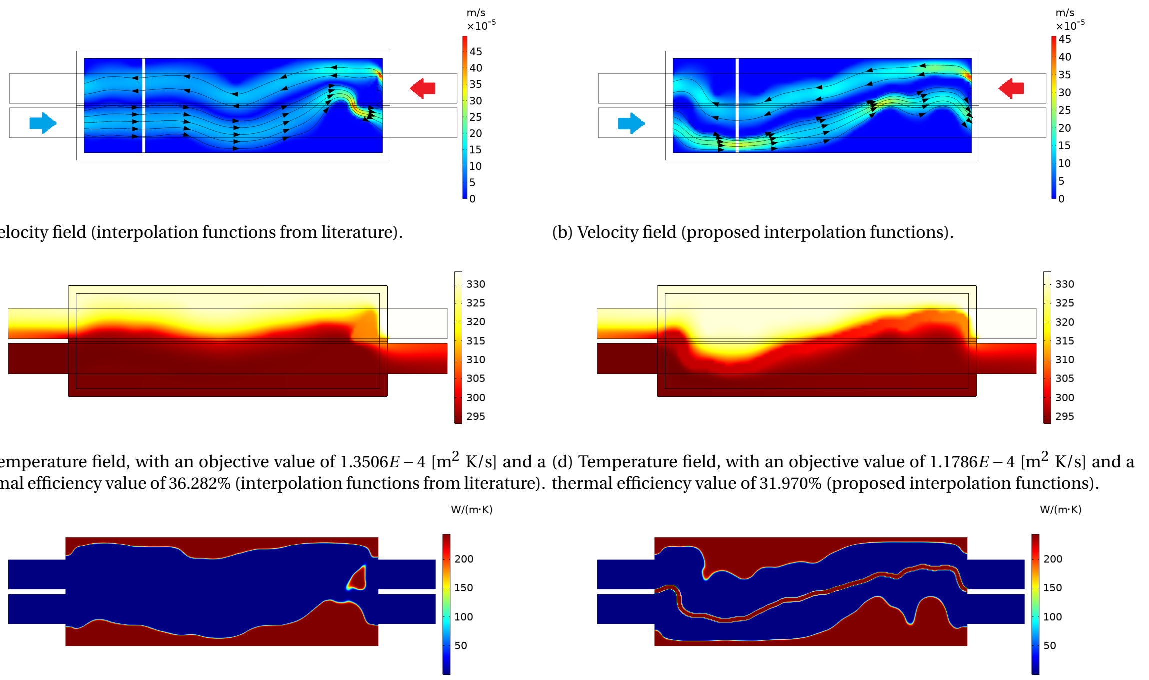

(a) Velocity field (interpolation functions from literature).

(b) Velocity field (proposed interpolation functions).

(c) Temperature field, with an objective value of $1.3506E-4$ [m^2 K/s] and a thermal efficiency value of 36.282% (interpolation functions from literature).

(d) Temperature field, with an objective value of $1.1786E-4$ [m^2 K/s] and a thermal efficiency value of 31.970% (proposed interpolation functions).

(e) Thermal conductivity field (interpolation functions from literature).

(f) Thermal conductivity field (proposed interpolation functions).

Figure 5.3: Optimal results generated with the two sets of interpolation functions. The fields of the optimal result generated with the interpolation functions from literature are provided on the left-side, while the fields of the optimal result generated with the proposed interpolation functions are provided on the right-side.

Similar to the identical fluids scenario, the velocity magnitude is evaluated on the white lines as shown in Fig. 5.3a and 5.3b. Fig. 5.4 shows the normalized velocity magnitude in the optimal designs generated with each set of interpolation functions. Fig. 5.4a shows the plot of the normalized velocity fields generated with the interpolation functions from literature. Fig. 5.4b shows the plot of the normalized velocity fields generated with the proposed interpolation functions. In the results generated with the interpolation functions from literature, the overlapping regions are visible in the solid regions and between the fluids. In the results generated with the proposed interpolation functions, the overlapping regions are visible in the solid material regions including the non-mixing region. The same holds here as in the identical fluids scenario, further increasing the β values will reduce the size of the overlapping regions.

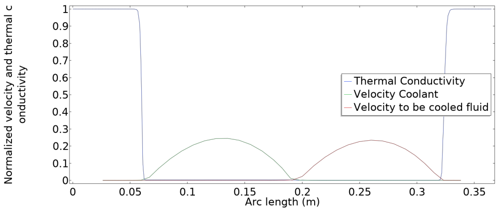

(a) Normalized cross-section of the design generated with the interpolation functions from literature. The velocity fields are normalized with $4.97E-4$[m/s] (maximum flow velocity) and the thermal conductivity is normalized with 244[W/mK] (thermal conductivity of the solid material k_s).

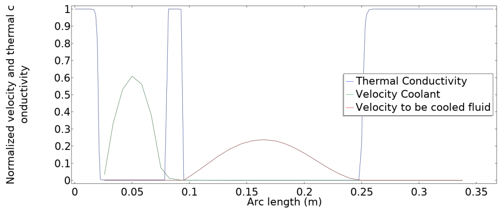

(b) Normalized cross-section of the design generated with the proposed interpolation functions. The velocity fields are normalized with $4.59E-4$[m/s] (maximum flow velocity) and the thermal conductivity is normalized with 244[W/mK] (thermal conductivity of the solid material k_s).

Figure 5.4: Comparing overlapping regions in the designs generated with the two sets of interpolation functions.

Similar to the two identical fluids optimization scenario, the proposed non-mixing constraint prevents the forming of a mixing heat exchanger design and by doing so alters the optimization behaviour significantly. The same optimization scenarios are also computed with the domain objective function as provided in Eq. 3.29. The optimal results and analysis of the results are provided in Appendix D.

6

2D Heat Exchanger: Material parameters

One of the material parameters that influences the interpolation behaviour is the thermal conductivity. The thermal conductivity of the materials will determine the interpolation range and therefore the optimization behaviour. In this chapter, the effect of the thermal conductivity on the optimization behaviour is investigated. Since a wide variety of materials can be used as solid material in a heat exchanger, the values for the thermal conductivity can also vary significantly. The large difference between the thermal conductivity of the fluids and the solid material creates a large interpolation range. Large interpolation ranges can lead to erroneous behaviour of the physics, since in these interpolation regions the material properties have intermediate values and therefore do not represent the physics correctly. An example of such an erroneous behaviour occurs in material regions with a thermal conductivity in the range of solid materials with a non negligible velocity field. The region with intermediate material properties influences the optimization behaviour and therefore the generated optimal design. By varying the thermal conductivity of the solid material the interpolation region is altered and the effect on the optimization behaviour can be investigated.

6.1. Thermal Conductivity

The used thermal conductivity value for the solid material was 244 [W/(mK)], which is in the range of aluminium. To investigate a large range of thermal conductivity values, two materials with a thermal conductivity lower than 244 [W/(mK)] and two materials with a thermal conductivity higher than 244 [W/(mK)] are compared. The thermal conductivity values selected for the solid material, apart from aluminium, are in the range of stainless steel (AISI 310), carbon steel (AISI 8630), silver and diamond. Table 6.1 shows the material properties of all solid materials used. The physical material values are retrieved from CES Edupack 2019 [1]. The values in CES Educpack are provided in ranges and a value in this range is selected. The values of the thermal conductivity and heat capacity are evaluated at 296.15K. Silver and diamond are materials not likely used in a heat exchanger due to the material costs or manufacturability. These two materials are selected for the high thermal conductivity value, which can be used to determine the optimization behaviour for relatively large interpolation ranges. The fluids used both have a thermal conductivity value of 0.6 [W/(m K)] in all scenarios.

Material Property	**AISI 310, wrought**	**AISI 8630**	**Aluminium**	**ASTM Standard B742-90: Fine Silver**	**Diamond, pure**
Density (ρ_s) [kg/m^3]	8000	7800	2700	10500	3500
Heat capacity ($c_{p,s}$) [J/(kg K)]	510	470	935	235	510
Thermal conductivity (k_s) [W/(m K)]	14	50	244	420	1000

Table 6.1: Solid materials used in the optimization algorithm.

The heat exchanger has a counter-flow configuration, with two identical fluids. The coolant flows into the design domain at the left-side, while the to be cooled fluid flow into the design domain at the right-side. Table 6.2 shows the values used for the dimensions of the design domain as shown in Fig. 3.14, the values used for the filtering and projection parameters and the values of the remaining parameters. During the optimization process, the values for β_1 and β_2 are increased from 8 to 100. The value for β_3 is increased from 2 to 100. For lower β_3 values the non-mixing region is not fully defined as elaborated on in Section 3.3.1. By setting the initial value of β_3 to 2, the non-mixing region is gradually introduced into the design during the optimization process. The lower limits for β_1 and β_2 are set to 8, since these parameters have less influence on the shape of the non-mixing region. The upper limit, β_{max}, for β_1, β_2 and β_3 is set to 100 based on the method to estimate a suitable β_{max} value as provided in Section 3.4.5. The incremental schemes used are $\beta_1 = \beta_2 = 8, 8, 8, 8, 10, 12, 14, 16, 18, 20, 24, 28, 32, 36, 40, 50, 60, 70, 80, 90, 100$ and $\beta_3 = 2, 4, 6, 8, 10, 12, 14, 16, 18, 20, 24, 28, 32, 36, 40, 50, 60, 70, 80, 90, 100$. The β parameters are updated every 20 iterations ($n = 20$).

Dimensional Parameters	**Values**	**Filter and Projection Parameters**	**Values**	**Parameters**	**Values**
L1	1 [m]	R_1	0.03 [m]	h	0.01 [m]
L2	0.315[m]	β_1	8-100 [-]	$T_{in,f1}$	293.15 [K]
L3	0.05 [m]	R_2	0.03 [m]	$T_{in,f2}$	333.15 [K]
L4	0.1 [m]	β_2	8-100 [-]	Re_1	10 [-]
L5	0.015 [m] (t_{min})	t_{min}	0.015 [m]	Re_2	10 [-]
L6	0.25 [m]	β_3	2-100 [-]	C_1	500 [-]
L7	0.025 [m]			C_2	2 [-]

Table 6.2: Parameter values used in optimization scenarios.

Fig. 6.1 shows the optimal results for each solid material scenario. The results in Fig 6.1 are provided in the same order as the materials in Table 6.2, with an increasing thermal conductivity from 14 [W/(m K)] to 1000 [W/(m K)]. To express the performance of the heat exchanger, the thermal efficiency and objective value are provided with the optimal result in Fig 6.1. The results show that even though the design domain is small, the optimal designs have significantly different channel shapes. In all optimal designs the non-mixing region is completely generated with the non-mixing filter ($\hat{\hat{\theta}}_3$) and has the minimum wall-thickness (t_{min}) in the entire design domain. In the scenarios, except the scenario with $k_s = 14$ [W/(mK)], the optimizer creates tortuous channel shapes to elongate the fluid channels within the design domain and improve the heat transfer. The objectives values of the corresponding optimal designs show an increasing objective value with an increasing thermal conductivity in the solid material regions. This optimization behaviour is logical since the objective function maximizes the heat exchange in the design domain and a higher thermal conductivity in the solid region allows for a better overall heat exchange. The differences between the heat exchanger performances is relatively small, similar to the differences between the objective values. The heat exchanger performance has an increasing trend with an increasing thermal conductivity in the solid material regions. The only deviation from the trend is the optimal design with the thermal conductivity of diamond ($k = 1000$ [W/(mK)]), which has a performance slightly lower than that of silver ($k = 420$ [W/(mK)]). This deviation from the trend could originate from the objective function used. The objective function does not optimize for a maximum temperature difference between the inlet and outlet of the to be cooled fluid, but maximizes the heat exchange in the design domain. This could explain the deviation from the trend since the objective values do increase consistently with an increased thermal conductivity in the solid material regions. Since the differences in heat exchanger performances are relatively small it is difficult to make a general conclusion based on these results only.

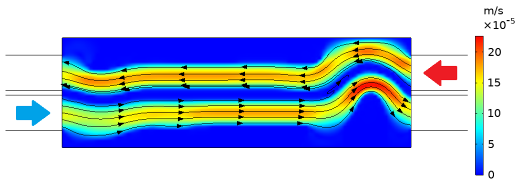

(a) Velocity field final result AISI310 ($k = 14[W/(mK)]$).

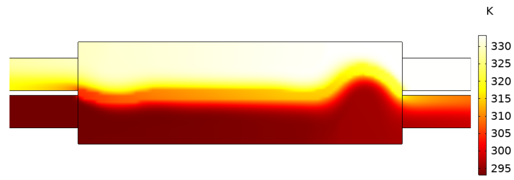

(b) Temperature field final result AISI310 with an efficiency of 25.173% and an objective value of 5.6585E6 [kg m K/s^3].

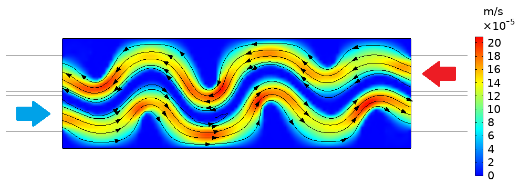

(c) Velocity field final result AISI8630 ($k = 50[W/(mK)]$).

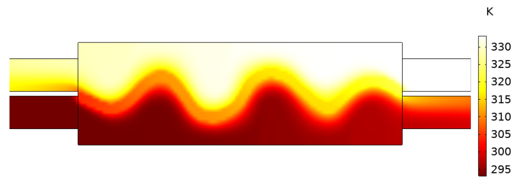

(d) Temperature field final result AISI8630 with an efficiency of 26.553% and an objective value of 6.1802E6 [kg m K/s^3].

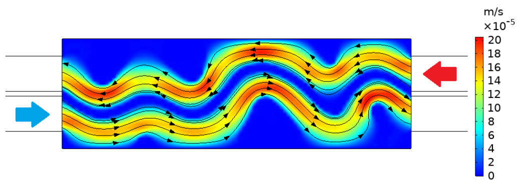

(e) Velocity field final result aluminium ($k = 244[W/(mK)]$).

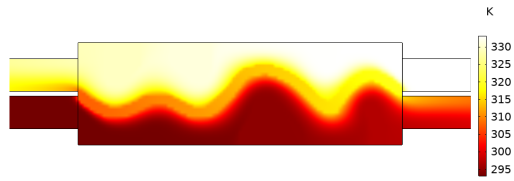

(f) Temperature field final result aluminium with an efficiency of 26.603% and an objective value of 6.2903E6 [kg m K/s^3].

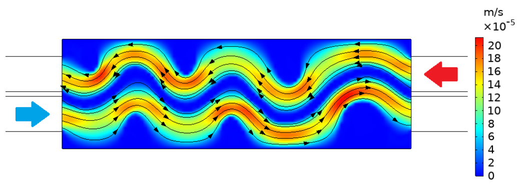

(g) Velocity field final result silver ($k = 420[W/(mK)]$).

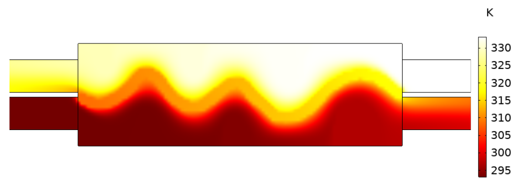

(h) Temperature field final result silver with an efficiency of 26.732% and an objective value of 6.3893E6 [kg m K/s^3].

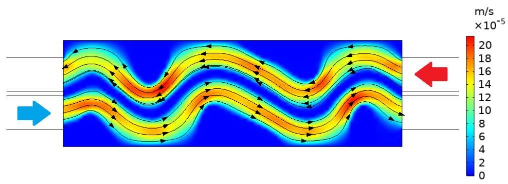

(i) Velocity field final result diamond ($k = 1000[W/(mK)]$).

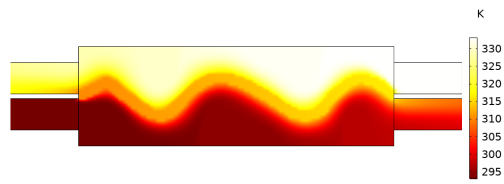

(j) Temperature field final result diamond with an efficiency of 26.705% and an objective value of 6.4685E6 [kg m K/s^3].

Figure 6.1: Final results of the different solid materials used to determine the interpolation and optimization behaviour.

To further investigate this topic different optimization scenarios could be applied with different fluids, design domains and boundary conditions. For the lowest thermal conductivity value (14 [W/(m K)]), the optimizer stopped improving the design halfway through the optimization process (at approximately $\beta_1 = \beta_2 = \beta_3 = 24$). For relatively small interpolation ranges the intermediate density regions diminish for lower β values compared to larger interpolation ranges. To show the effect of the β increments on the design changes for different interpolation ranges, the β increments are plotted against the objective values in a similar approach as provided in Section 3.4.5. In this approach a discrete design is compared with an identical density-based design on which a β sweep is performed. The β sweep performed increases the β values from 4 to 150. The design domain, boundary conditions and (material) parameter settings are identical for all optimization scenarios as provided in Table 6.2 apart from the solid material properties. The material properties of the solid material are varied between AISI310, aluminium and diamond as provided in Table 6.1. The objective values of the interpolated designs are normalized with an objective value of a discrete design computed with the same material parameters. Fig. 6.2 shows the normalized objective values of interpolated designs with AISI310, aluminium and diamond as solid materials.

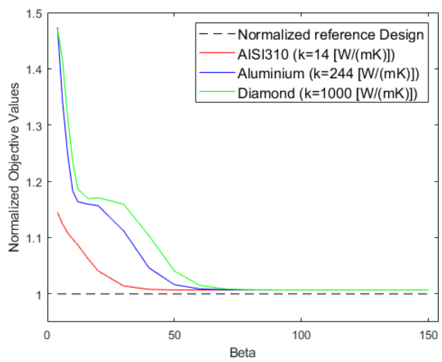

Figure 6.2: Plot of normalized objective values for a β sweep performed on designs with AISI310, aluminium and diamond as solid materials.

The plot shows that the thermal conductivity interpolation range does influence the β value needed for stabilization of the objective value. For smaller interpolation ranges, the objective values stabilize for a lower β value compared to larger interpolation ranges. In other words the β_{max} value could be selected lower for smaller thermal conductivity interpolation ranges, since the objective value stabilizes for a lower β value. This behaviour explains the stopping of the design improvements halfway through the β continuation scheme with a thermal conductivity of AISI310 ($k = 14$ [W/(mK)]).

The thermal conductivity of the solid material (k_s) does not influence the fluid flow, since the inverse permeability interpolation functions (Eq. 3.21 and 3.22) are independent of the thermal conductivity k_s. From the same β sweep as performed on the three solid material scenarios the pressure drop values of both channels are plotted against the β values. Fig. 6.3 shows the plot of the normalized pressure drop values for each corresponding β value. The plot shows that all normalized pressure drop values, of both the fluid channels, are identical for every corresponding β value and are independent of the solid material properties used.

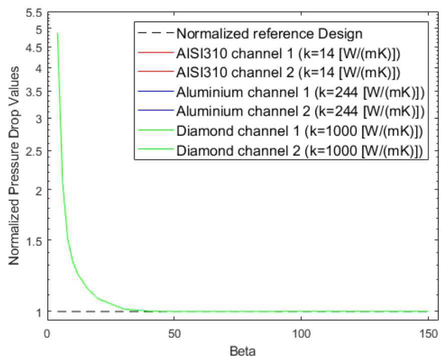

Figure 6.3: Plot of normalized pressure drop values for a β sweep performed on designs with AISI310, aluminium and diamond as solid materials.

To prevent the optimization algorithm from running without further improving the design (for β_{max} value selected too high) or prematurely stopping of the optimization algorithm (the β_{max} value selected too low), the β_{max} value should be selected based on the parameter values used in concerning optimization scenario. To determine a suitable β_{max} value, the β_{max} estimation method as provided in Section 3.4.5 can be used.

7
3D Heat Exchanger: Non-Mixing Constraint

In this chapter the proposed non-mixing constraint is used in a 3D optimization scenario. The reason for setting up a 3D model is to determine if the non-mixing constraint correctly seperates the two fluids in a 3D design domain and to investigate the optimization behaviour. This chapter is the only chapter that makes use of a 3D design domain, therefore all details related to the optimization set-up are provided within this chapter.

7.1. 3D Counter-Flow Heat Exchanger

The definition of the non-mixing constraint is identical in 2D and 3D, but the physics and design variable fields have an additional spatial component. The shape of the 3D design domain used with the corresponding dimensional parameters are provided in Fig. 7.1. The dimensions of the in- and outflow regions are identical on both sides of the design domain and are placed at the same height on the left- and right-side of the design domain.

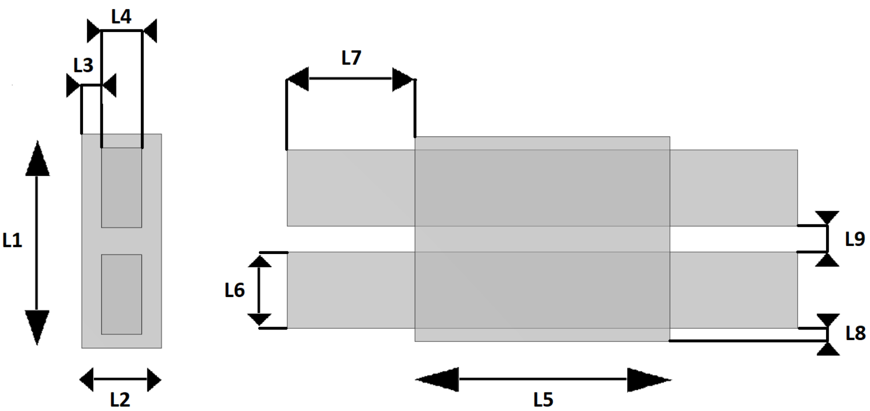

Figure 7.1: Design domain and dimensional parameters used in the 3D optimization scenario.

Similar to the mesh used in the 2D optimization scenarios a structured mesh is used in the 3D optimization scenario. The mesh element shape used is a cubic mesh element with identical lengths $h_x x h_y x h_z$. The structured mesh is provided in Fig. 7.2. A relatively course mesh is used compared to the 2D optimization scenarios to limit the computational power.

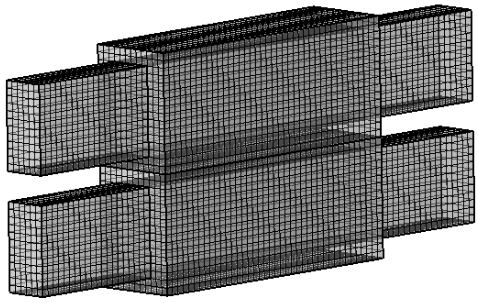

Figure 7.2: The structured mesh used in the 3D optimization scenario.

In the 3D optimization scenarios passive regions are only used for the second design variable θ_2, see Fig. 7.3. The first design variable is only defined in the active part of the design domain, the active part of the design domain is denoted with Ω in Fig. 7.3. The objective function used is the domain objective function provided in Eq. 3.29. The domain integral in the objective function is evaluated in the active part of the design domain Ω. Similar to the 2D optimization scenarios, two pressure drop constraints are used one for each fluid channel. The formulation of the pressure drop constraints is identical to formulation used in the 2D optimization scenarios, see Eq. 3.31. The average pressure values $p_{1,1}$, $p_{1,2}$, $p_{2,1}$ and $p_{2,2}$ are now evaluated at the in- and outflow surfaces corresponding to the active part of the design domain, see Fig. 7.3.

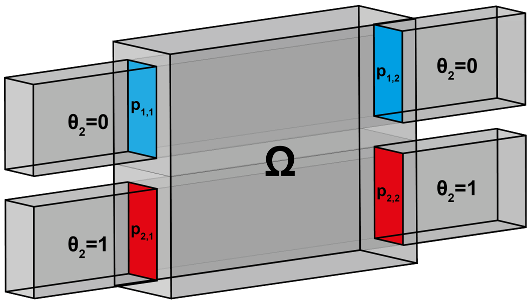

Figure 7.3: Passive regions in the design domain defined for the second design variable θ_2.

In the 3D optimization scenarios a counter-flow heat exchanger is used with identical fluids, with material properties of water. The coolant flows into the design domain on the right-side of the design domain and the to be cooled fluid flows into the design domain on the left-side of the design domain. Table 7.1 provides the values of design domain dimensions as indicated in Fig. 7.1. Table 7.1 also includes the values for the filtering and projection parameters and the values of the remaining parameters. During the optimization process, the values of β_1, β_2 and β_3 are increased from 8 to 100. The lower limit for β_1, β_2 and β_3 is set to 8, because the bandpass projection function is active between 0 and 1 for $\beta_3 \geq 8$ (see Section 3.3.1). The upper limit, β_{max}, for β_1, β_2 and β_3 is set to 100 based on the method to estimate a suitable β_{max} value as provided in Section 3.4.5. The incremental scheme used for the β parameters is $\beta_1 = \beta_2 = \beta_3 = 8, 10, 12, 16, 20, 24, 28, 32, 36, 40, 45, 50, 60, 70, 80, 90, 100$. The β parameters are updated every 20 iterations ($n = 20$). The thermal conductivity value for the solid material is lowered from 244 [W/(mK)] to 10 [W/(mK)] to force the channels to move towards each other with less iterations. A lower solid thermal conductivity value is disadvantageous for the heat transfer between the solid regions and the fluids. As a result the gradient information is favorable for moving the fluid channels closer to each other for a better heat transfer.

Dimensional Parameters	Values	Filter and Projection Parameters	Values	Parameters	Values
L1	0.8 [m]	R_1	0.05 [m]	h	0.025 [m]
L2	0.3 [m]	β_1	8-100 [-]	$T_{in,f1}$	293.15 [K]
L3	0.075 [m]	R_2	0.05 [m]	$T_{in,f2}$	353.15 [K]
L4	0.15 [m]	β_2	8-100 [-]	Re_1	10 [-]
L5	1 [m]	t_{min}	0.025 [m]	Re_2	10 [-]
L6	0.3 [m]	β_3	8-100 [-]	C_1	500 [-]
L7	0.5 [m]			C_2	10 [-]
L8	0.05 [m]				
L9	0.1 [m]				

Table 7.1: Parameter values used in the 3D optimization scenario.

Fig. 7.4 shows the initial design and optimal design generated with the 3D optimization model. The non-mixing constraint separates the fluids and allows for the forming of a variable wall-thickness in a similar manner as in the 2D optimization scenarios. The optimal design has two fluid channels curved towards eachother with a decreased cross-section. During the optimization process, the optimizer improved the design in an almost symmetrical manner resulting in two almost identical fluid channels. The symmetrical optimization behaviour likely stems from the symmetric design domain and boundary conditions. The lowered thermal conductivity of the solid material forced the optimizer to move the fluid channels towards each other in an early stage of the optimization process.

(a) Initial design side view.

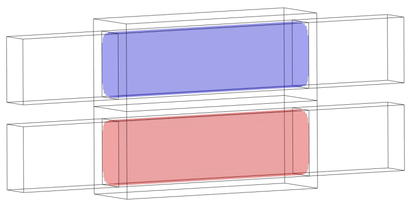

(b) Initial design angled view.

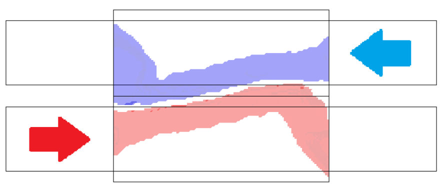

(c) Optimal design side view.

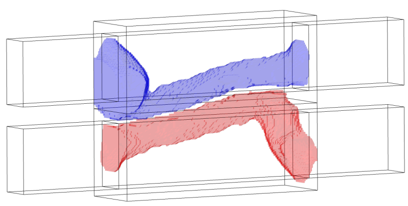

(d) Optimal design angled view.

Figure 7.4: Optimal design generated with a counter-flow configuration.

The optimizer generated an optimal design with a variable wall-thickness. The minimum wall-thickness is guaranteed with $\hat{\hat{\theta}}_3$, while the other solid material region surrounding the minimum wall-thickness is generated with $\hat{\hat{\theta}}_1$. To show the contribution of $\hat{\hat{\theta}}_1$ and $\hat{\hat{\theta}}_3$ to the total solid material region, the solid material region corresponding to $\hat{\hat{\theta}}_1$ and $\hat{\hat{\theta}}_3$ is plotted seperately and combined. The solid material region corresponding to $\hat{\hat{\theta}}_1$ is shown in Fig. 7.5a, while the solid material region corresponding to $\hat{\hat{\theta}}_3$ is shown in Fig.7.5b. The total solid material region is provided in Fig. 7.5c.

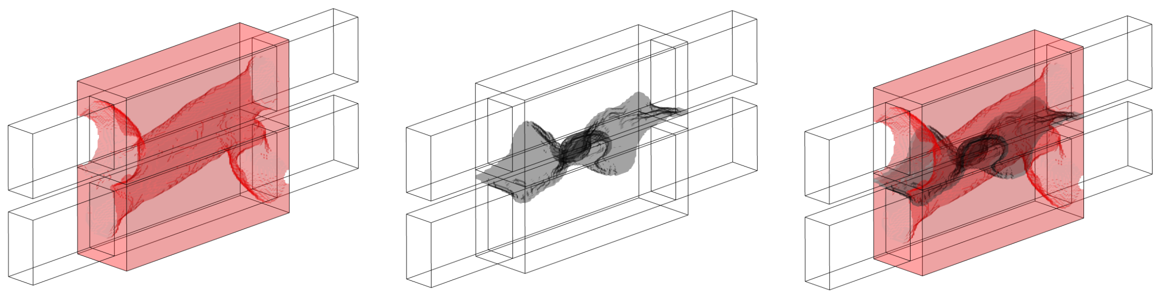

(a) Solid material region corresponding to $\hat{\hat{\theta}}_1$.

(b) Solid material region corresponding to $\hat{\hat{\theta}}_3$.

(c) Total solid material region generated with the non-mixing constraint.

Figure 7.5: Variable wall-thickness generated with non-mixing constraint.

To determine if the actual generated minimum wall-thickness is also enforced accurately with t_{min} in 3D, the generated minimum wall-thickness is measured in a similar manner as in 2D. The minimum wall-thickness is determined with a line evaluation in the 3D design domain. The generated minimum wall-thickness defined with $\hat{\hat{\theta}}_3$ is evaluated at the line intersecting with the minimum wall-thickness. Fig. 7.6a shows the minimum wall-thickness generated with the non-mixing constraint and the black line used to evaluate the non-mixing variable $\hat{\hat{\theta}}_3$. Fig. 7.6b shows the non-mixing variable ($\hat{\hat{\theta}}_3$) evaluated at the black line in Fig. 7.6a. The minimum wall-thickness (t_{min}) is 0.025 [m] and the measured minimum wall-thickness is 0.0251 [m]. The difference between t_{min} and the measured minimum wall-thickness can be explained by the manually determined location of the evaluation line.

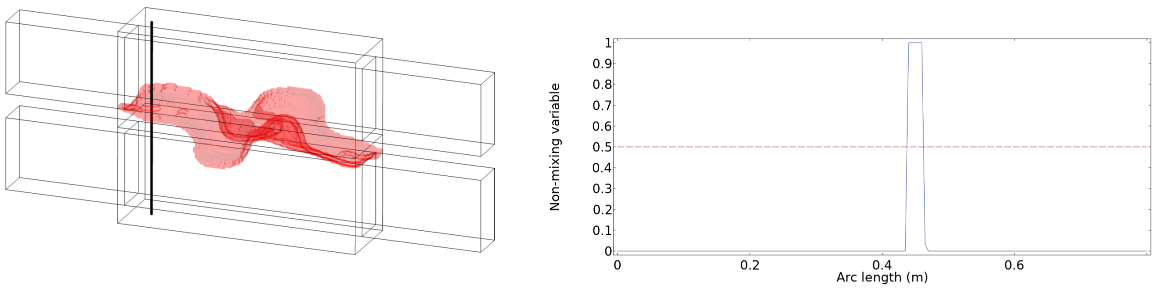

(a) Solid material region corresponding to $\hat{\hat{\theta}}_3$ with $t_{min} = 0.025$ [m].

(b) Non-mixing variable evaluated at the black line in Fig. 7.6a. The measured minimum wall-thickness is 0.0251 [m].

Figure 7.6: Evaluation of the generated minimum wall-thickness for comparison with t_{min}.

To investigate the optimization behaviour in a two different fluids optimization scenario, the material properties of the to be cooled fluid are set to engine oil. The mesh is refined with h being set to 0.0125 [m]. The heat exchanger configuration and initial design used are identical to the previous optimization scenario. Table 7.2 shows the values used for the dimensions of the design domain as shown in Fig. 7.1, the values used for the filtering and projection parameters and the values of the remaining parameters. The β values are increased from 8 to 28 and the β values are increased every 10 iterations, $n = 10$. The lower limit for β_1, β_2 and β_3 is set to 8, because the bandpass projection function is active between 0 and 1 for $\beta_3 \geq 8$ (see Section 3.3.1). The upper limit, β_{max}, for β_1, β_2 and β_3 is set to 28. The different fluids optimization scenario is computed to show that the 3D optimization model functions correctly with two different fluids, it is therefore not needed to increase the β_{max} value to 100. The β_{max} value is lowered from 100 to 28 to reduce the total computation time. The incremental scheme used for the β parameters is $\beta_1 = \beta_2 = \beta_3 = 8, 10, 12, 16, 20, 24, 28$. The thermal conductivity of the solid material is set to 6.7 [W/mK], which is the thermal conductivity of laser melted Grade 23 titanium [17]. The thermal conductivity of laser melted Grade 23 titianium is selected because Selective Laser Melting (SLM) is an additive manufacturing method that can be used to manufacture complex amorphous geometries. SLM could be a manufacturing method to actually produce the heat exchanger designs generated with topology optimization.

Dimensional Parameters	Values	Filter and Projection Parameters	Values	Parameters	Values
L1	0.8 [m]	R_1	0.025 [m]	h	0.0125 [m]
L2	0.3 [m]	β_1	8-28 [-]	$T_{in,f1}$ (water)	293.15 [K]
L3	0.075 [m]	R_2	0.025 [m]	$T_{in,f2}$ (oil)	353.15 [K]
L4	0.15 [m]	β_2	8-28 [-]	Re_1	1 [-]
L5	1 [m]	t_{min}	0.025 [m]	Re_2	0.018 [-]
L6	0.3 [m]	β_3	8-28 [-]	C_1	500 [-]
L7	0.5 [m]			C_2	3 [-]
L8	0.05 [m]				
L9	0.1 [m]				

Table 7.2: Parameter values used in the 3D optimization scenario.

Fig. 7.7 shows the initial design and the optimal design generated with the different fluids optimization scenario. The optimal design shows a non-mixing region with a variable wall-thickness separating the two fluid channels. To show that the optimal design has two different fluids, the thermal conductivity values in the fluid channels are plotted.

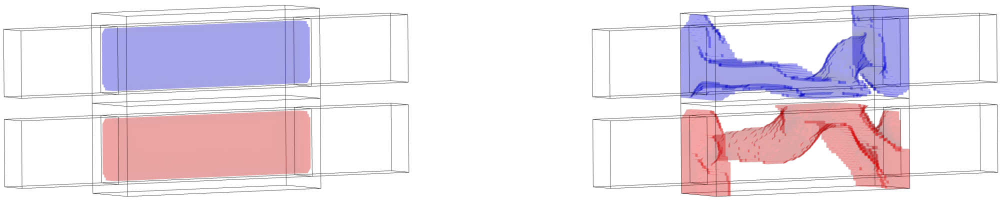

(a) Initial design.

(b) Optimal design.

Figure 7.7: Optimal design generated with a counter-flow configuration and different fluids.

Fig. 7.8 shows the plotted thermal conductivity values in the fluid channels. The top channel corresponds to the coolant (water) with a pres-set thermal conductivity of 0.6 [W/mK], while the bottom channel corresponds to the to be cooled fluid with a pres-set thermal conductivity of 0.1233 [W/mK]. The thermal conductivity values in the fluid channels match the corresponding pre-set values. The optimal design generated with the two different fluids optimization scenario was post-processed and 3d-printed. The details on the post-processing steps needed to create a mesh-file and the printing method used are provided in Appendix E.

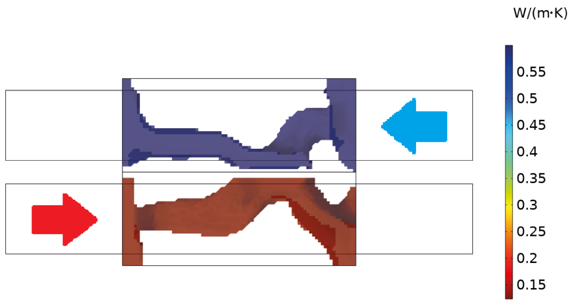

Figure 7.8: Value of the thermal conductivity in the fluids regions.

8 Discussion

This chapter is divided into two sections. In the first section the generated results are discussed and possible improvements to the optimization model are suggested. In the second section topics for further research are proposed.

8.1. Results

During the set-up phase of the optimization model and the analysis of the generated optimal results, four topics for improvement of the optimization model were noticed and will be elaborated on in this section. The first topic for improvement is about approximating the bandpass projection shape. The second and third topic are related to the boundary conditions used and passive solid material regions enclosing the design domain. The fourth topic is about fine-tuning of the β continuation scheme based on the material properties used.

To approximate the bandpass projection shape, the value for t_{min} has to be selected larger than one mesh element. The approximated bandpass projection shape will become more accurately approximated (more continuous), the more mesh elements used. In some of the optimization scenarios the minimum wall-thickness is close to the mesh element size $t_{min} \approx h$. In optimization scenarios with $t_{min} \approx h$ the bandpass projection shape will generate a non-mixing region, but will not represent the heat transfer accurately within the non-mixing region. Using a t_{min} value equal to four or five mesh elements with sufficiently high β values will improve the approximation of the heat transfer in the non-mixing region.

In all optimization scenarios the boundaries of the design domains are adiabatic, this boundary condition is commonly used in literature related to heat exchanger topology optimization. However, the concept of a perfectly insulated heat exchanger is not very realistic. Heat exchange with the environment would help generating more realistic heat exchanger designs. Testing conditions could also be easier to recreate. If a design generated with adiabatic boundaries would be manufactured and tested, the test would require a perfectly insulated heat exchanger to end up with comparable results. Allowing for heat transfer with the environment at an environment temperature similar to the actual application environment, would likely be easier to recreate for testing. Depending on the type of heat exchanger optimization scenario, heat transfer at the boundaries could further improve the efficiency of the optimal designs. In some applications heat exchangers are placed in an environment that is advantageous for the heat transfer to further improve the efficiency. If such a heat exchanger would be implemented within the proposed optimization model, interaction with the environment should also be implemented. With heat transfer at the outer boundaries of the design domain, passive solid material regions surrounding the design domain are required to prevent direct contact between the fluids and the environment. Another reason these passive regions around the design domain could be useful is for post-processing of an optimal design for manufacturing, see Appendix E. For a design with fluids touching the boundaries to be actually used, a solid material region has to placed around the design domain to enclose the fluid regions at the boundaries.

A side-effect of the boundary conditions that was noticed during the optimization process and is visible in the optimal results, is sticking of the fluid channels to the boundaries of the design domain. The side-effect is visible in Fig. C.5b (all corners), C.6b (bottom and right boundary), D.1g (left top corner and right bottom corner), D.1h (top and bottom boundary), D.3g (top and bottom boundary) and D.3h (top and bottom boundary). Sticking of the fluid channels to the outer boundaries originates from the transition between the active design domain and the adiabatic outer boundaries of the design domain. If the fluid regions are moved to have direct contact with the outer boundary of the design domain, the interpolation region completely disappears. The interpolation functions generate regions with intermediate values (interpolation regions) and thereby gradient information for the optimizer. When these interpolation regions disappear, the gradients in this region will become zero. These newly generated zero-gradient regions can not be altered by the optimization algorithm if no new gradient information becomes available in these regions. Sticking of fluid regions to the boundaries can be prevented by placing a passive solid region around the active design domain. By placing a passive solid boundary around the active part of the design domain, the interpolation region between the fluids and solid is guaranteed in the entire active part of the design domain. In Chapter 4 and 5 the passive solid material regions are implemented and the fluid channels do not stick to the boundaries of the design domain. With the passive solid material regions implemented, the optimizer can more easily generate solid material in the corners of the design domain.

In chapter 6, the material properties of the solid material are varied in the range of realistic material parameters. This topic is investigated to determine the influence of the solid material properties on the interpolation and optimization behaviour. The optimal results showed that the interpolation range of the thermal conductivity alters the interpolation behaviour, in optimization scenarios where the other parameter values and β continuation scheme are identical. Fine-tuning the β continuation scheme for a specific set of parameter settings can be advantageous for the optimization behaviour. While the material properties of the solid material is altered, the material properties of the fluids remains the same. The interpolation range of the thermal conductivity depends on both the thermal conductivity value of the fluids and solid material. Depending on the fluid selected the interpolation range can become larger. The material parameters used in the current optimization set-ups have values in the range of liquids. The thermal conductivity of gasses can be significantly lower than that of the liquids currently used. Optimization scenarios with thermal conductivity values in the range of gasses could provide further insights into the interpolation behaviour and fine-tuning of the β continuation scheme.

8.2. Further Research

In this section seven topics that might be interesting for further research are elaborated on. The first topic for further research is the threshold values used in the bandpass projection function. The second and third research topic are about approximating the physics and physical material parameters. The fourth topic is related to the solver settings and the fluid mechanics. The fifth research topic is about verification of designs generated with topology optimization. The sixth and seventh research topic are related to post-processing the optimal designs for manufacturing and validation tests with manufactured optimal designs.

The threshold values of η_3 and η_4 are fixed at $\eta_3 = 0.1$ and $\eta_4 = 0.9$ in all optimization scenarios. The expression for the minimum wall-thickness is thus only verified for these threshold parameter values. To further investigate if the expression used to set the minimum wall-thickness accurately approximates the generated minimum wall-thickness for a variety of η_3 and η_4 values, a similar verification can be performed with a variety of η_3 and η_4 values.

To accurately approximate the physics in the fluid mechanics a minimum number of mesh elements is needed in the diameter of a fluid channel. To accurately approximate the physics of the heat transfer a minimum number of mesh elements is needed in the non-mixing region separating the fluids. The minimum number of mesh elements needed to describe a laminar fluid flow in a fluid channel was not investigated in the literature survey of this thesis project. So it is unknown to me if there is a specific guideline for the minimum number of mesh elements needed to describe a laminar fluid flow in a fluid channel. This topic requires further investigation, since finding an acceptable number of mesh elements has to be verified with actual test results. An actual test with measurement of the physics with an identical design will show the actual under- or overestimation of the physics with FEA. A straight channel design with a constant diameter can be used for verification. The proposed varification will only hold for the straight channel initial design. During the optimization process, the optimizer can locally decrease the diameter of the fluid channels based on the maximum allowable pressure drop. The generated optimal designs can have fluid channels with less then the preferred minimum number of mesh elements and a poor approximation of the physics based on the maximum allowable pressure drop selected. The minimum number of mesh elements needed in the non-mixing region is elaborated on in Section 3.3.1.

The interpolation range of the thermal conductivity depends on both the thermal conductivity of the fluids and the solid. The fluids used have material properties in the range of liquids in all optimization scenarios and both fluids are identical. The thermal conductivity of gasses can be lower than that of liquids. If a two-fluid heat exchanger optimization with gasses would be performed, the interpolation range would further increase. To further extent the research on the effect of using different material parameters, scenarios with two different fluids should be investigated and the effect of using fluids with material properties in the range of gasses.

In the optimization scenarios provided in this report, relatively low Reynolds numbers are used. In the set-up phase of the optimization model Reynolds numbers up to 70 were used in the 2D optimization scenarios. For Reynolds numbers higher then 70, the forward analysis of the fluid flow could not converge to a solution. The convergence issues could be independent of the proposed non-mixing constraint and more related to the solver settings. The convergence issues were not further investigated, since it was not required to use higher Reynolds number to determine if the non-mixing constraint performed adequately. However, a wide variety of two-fluid heat exchangers have flow characteristics with higher Reynolds numbers also in the turbulent regime. Solving the fluid flow for higher Reynolds numbers in the laminar regime can become significantly more difficult and further improving of the solver settings is required. To determine the performance of the non-mixing constraint for a wider range of heat exchanger optimization scenarios, a turbulence model could be added to the physics of the fluid flow. Adding a turbulence model could even further increase the difficulties in converging to a solution, but if implemented correctly could allow for the design of more realistic two-fluid heat exchangers with the proposed non-mixing constraint.

One of the aspects that was not investigated is verification of optimal designs generated with topology optimization. The optimal designs generated with a density-based method are often non-discrete as a result of the filters and material interpolation functions needed to define the material properties in the different material regions and make the optimization problem well-posed. The intermediate material regions do not represent material properties correctly and therefore the physics are not represented correctly. To verify an interpolated design, the interpolated design can be filtered to a discrete design and the forward analysis of the physics can be re-computed with the discrete design. With such a verification test the under- or overestimation of the physics in the optimization model can be determined. A verification test can also give insights into possible improvements to the parameter settings such as: further increasing the β values, smaller filter radii or different coefficient values in the interpolation functions. Even though a verification test could help improve the optimization model it can not provide information on the actual performance of the generated heat exchanger designs. To determine the actual performance of the optimal designs, these designs should be manufactured and tested for validation.

For an optimal design to be tested or even used in an actual product, the design has to be manufactured. Depending on the manufacturing method selected a different file format is needed. Apart from the file format needed, the optimization model might have to be altered to take production limits into account. Some properties that could pose production limitations are the materials available, the minimum wall-thickness that can be manufactured or the structure overhang angle. Since the designs generated with topology optimization are often amorphous, additive manufacturing could be a fitting manufacturing method. In Appendix E one of the 3D optimal designs is post-processed to a mesh-file that can be manufactured with additive manufacturing. Even though this appendix provides an outline for transforming a point cloud to a mesh-file (.STL), this approach is not very efficient. The provided approach requires a lot of manual operations and might not be as effective for all heat exchanger designs. An interesting research topic might be finding a method to create a mesh-file for manufacturing from an optimal design that requires a minimum number of manual operations, that is partially automated or fully automated. A manufacturing method like additive manufacturing could be ideal for prototyping, but could be less ideal for mass-production. Apart from prototyping for testing further research into mass-production of these amorphous optimal designs could be investigated. The two-fluid heat exchanger designs generated with topology optimization can only be used in actual products, if the designs can be manufactured with the production volume needed for application. The ideal manufacturing method for mass-production could be selected based on for example the materials that can be used with a manufacturing method, the production time and production costs. All the different aspects that have to be taken into account for mass-production should be investigated.

If the generated heat exchanger designs can be manufactured, the actual performance of the two-fluid heat exchangers can be verified with validation tests. The investigation into production and validation of a design generated with topology optimization has already been performed in [15]. The optimization algorithm they used is proprietary and the details are not available, so it is difficult to determine what type of parameter settings and non-mixing constraint are used. They manufactured their optimal design with stereolithography (SLA) using the plastic UMA 90 (urethane methacrylate). The performance of the manufactured optimal design is compared to a reference design also manufactured with SLA in a validation test. The test results can also be compared to the optimal designs generated within the computational framework to determine the under- or overestimation of the computational framework used. Two-fluid heat exchanger designs created with topology optimization have already been manufactured in plastic. An interesting topic for further research is looking into manufacturing a two-fluid heat exchanger design generated with topology optimization made from a metal. An additive manufacturing method that allows for the production of complex amorphous shapes in metal is Selective Laser Melting (SLM). Appendix E provides a 3D heat exchanger design manufactured with SLM. The manufactured design can not be used for testing, but does show potential. If this topic is further investigated, the designs generated with topology optimization could be manufactured for validation. It could be a step closer to the use of topology optimizated two-fluid heat exchanger designs in existing products.

9 Conclusion

In this chapter the conclusions drawn from the generated results in the previous chapters are presented. The conclusions are provided in the order of the corresponding chapters. In the final part of this conclusion the research question is answered.

In Chapter 4 the performance of the non-mixing constraint is investigated. In the first optimal designs generated with the boundary objective function (Eq. 3.28), the optimization algorithm generates enclosed stagnant fluid region at the adiabatic boundaries. The optimization algorithm generates these enclosed fluid regions at the adiabatic boundaries where the gradients have completely been removed and a new solid material region is generated. Instead of generating a completely solid material region a fluid region corresponding to the other fluid is introduced and the non-mixing filter generates a non-mixing region between the fluids. The forming of these enclosed fluid regions can be prevented by using passive solid material regions surrounding the active design domain. These passsive solid material regions prevent the gradients at the boundaries of the active design domain from being removed and thereby the forming of the enclosed fluid regions. Even though the forming of the enclosed fluid regions only occurred with the boundary objective function, the complete removal of the gradients at the boundaries can also occur with the domain objective function (Eq. 3.29). The forming of enclosed fluid regions did not occur with the domain objective function, so it could be that the preference for the enclosed fluid regions originates from the gradient information taken into account with the boundary objective function.

To verify if the expression used to set the minimum wall-thickness (Eq. 3.16) accurately approximates the actual generated minimum wall-thickness a parameter sweep on t_{min} is performed and the generated wall-thickness is measured. Three different values for t_{min} are selected and applied in the same optimization scenario (the other parameter values are kept identical), so the non-mixing region in each scenario can be clrearly distinguished. The three generated optimal designs show the minimum wall-thickness defined in the entire design domain. The actual generated wall-thickness is sufficiently close approximated for higher β values ($\beta_1 = \beta_2 = \beta_3 \geq 80$).

In the results concerning the verification of the expression used to define the minimum wall-thickness, the optimization algorithm only forms designs with a constant wall-thickness (t_{min}). Depending on the optimization scenario selected it is advantageous to have the minimum wall-thickness in the entire design domain. However, to show that the non-mixing constraint allows for the forming of a variable wall-thickness an optimization scenarios is selected where a larger wall thickness than t_{min} has to be formed. In such optimal designs it was shown that the non-mixing constraint guarantees the minimum wall-thickness between the two fluids, while the first design variable ($\hat{\tilde{\theta}}_1$) is used to generate solid material regions around the minimum wall-thickness. The solid material regions generated with the first design variable ($\hat{\tilde{\theta}}_1$) and the non-mixing variable ($\hat{\tilde{\theta}}_3$) are combined to form a solid material region separating the two fluids with a variable wall-thickness.

Depending on the initial design used it was found that the optimization algorithm is more or less likely to create walls with a thickness larger than t_{min}. If solid material regions defined with $\hat{\tilde{\theta}}_1$ are initially not present between the two fluids, the optimization algorithm is less likely to generate solid material regions between the fluids with $\hat{\tilde{\theta}}_1$. To form a variable wall-thickness, solid material regions have to be defined with both $\hat{\tilde{\theta}}_1$ and $\hat{\tilde{\theta}}_3$. In an initial design without solid material regions defined with $\hat{\tilde{\theta}}_1$ between the fluids, a variable wall-thickness will likely not be formed. The reason is that if no solid regions are defined with $\hat{\tilde{\theta}}_1$ between the fluids, the derivatives with respect to this design variable are zero in these regions (zero-gradient regions).

In Chapter 5 the proposed interpolation functions are compared to the original interpolation functions from literature [14]. Both non-mixing constraints prevent the fluid flow of the first fluid in the region of the second fluid and vice versa. Both non-mixing constraints can form a variable wall-thickness between the two fluids. However, while the non-mixing constraint from literature allows for the forming of a zero wall-thickness, the proposed non-mixing constraint guarantees a minimum wall-thickness that can be pre-defined with t_{min}. In two-fluid heat exchangers it can be advantageous for the heat transfer between the fluids to have direct contact between the fluids. If there is no constraint on the minimum wall-thickness between the fluids, the optimization algorithm can completely remove the solid region between the fluids to maximize the heat transfer. The goal of non-mixing constraints in the design of non-mixing two-fluid heat exchangers is that an actual non-mixing heat exchanger design is generated. For the designs generated with the original interpolation functions to qualify as non-mixing heat exchangers, post-processing of the designs is needed for placement of a non-mixing region between the fluids. Adding features in an optimal design in the post-processing phase will alter the physics in the heat exchanger and re-computing of the physics might be needed to verify the effect of the added features. Placing a wall in the post-processing phase means that the effect of the wall is not taken into accounted in the optimization process, the newly created design could be suboptimal.

In Chapter 6 a parameter sweep is performed on the thermal conductivity of the solid material to determine the effect on the optimization behaviour. The thermal conductivity of the solid material is varied, while the other parameter settings are fixed. The thermal conductivity of the solid material is selected since it has most influence on the interpolation range of the thermal conductivity and the interpolation range will determine the intermediate material region. Since only the thermal conductivity of the solid material is varied, only the heat transfer in the solid and intermediate material regions is altered. The non-mixing constraint guarantees a solid material region between the fluids and the heat transfer in this solid material region is directly affected by the corresponding thermal conductivity. A higher thermal conductivity value means that a higher heat transfer can be attained within the same material region, which is a trend that is also visible in the generated optimal designs. The results showed that the combination of the interpolation range and the parameter continuation scheme used on the β values significantly influence the optimization behaviour. If the interpolation range is smaller, the intermediate densities deminish for lower β values than for larger interpolation ranges. In an optimization scenario with a smaller interpolation range, the design stops improving with lower β values. To prevent unnecessary computation time, the β continuation scheme should fine-tuned for the interpolation range of the thermal conductivity.

In Chapter 7 the 2D optimization model is extended to 3D to verify if the non-mixing constraint performs adequately in 3D. The 3D optimal designs show that the non-mixing constraint separates the fluids in a similar manner as in the 2D optimization scenarios. In both optimization scenarios a variable wall-thickness is generated. The non-mixing constraint separates the two fluid channels with the minimum wall-thickness (t_{min}) generated with the non-mixing variable $\hat{\tilde{\theta}}_3$, while the other solid material regions are generated with the first design variable $\hat{\tilde{\theta}}_1$. The actual generated minimum wall-thickness has a similar deviation from t_{min} compared to the 2D optimization scenarios. The interpolation functions used to handle both an identical and different fluids optimization scenario have been verified to also correctly define the material properties in the corresponding material regions in the 3D optimization model.

Based on the conclusions drawn from the generated results, the research question is answered. The research question is here provided:

> *Can a non-mixing constraint for density-based two-fluid topology optimization be created that guarantees a minimum wall-thickness and also allows for a wall-thickness larger than the minimum implemented within a finite element computational framework?*

The proposed non-mixing constraint is integrated in a density-based topology optimization method. The non-mixing constraint guaranteed a minimum wall-thickness in all optimization scenarios preventing the forming of mixing designs. A wall-thickness larger than the minimum wall-thickness can be generated to form a variable wall-thickness between the two fluids. The non-mixing constraint is implemented within a finite element computational framework. The research question can therefore be answered with yes, but specific settings must be used. To accurately approximate the interpolation shape of the bandpass projection function, the size of the minimum wall-thickness t_{min} should be set to at least two mesh elements. The higher the number of mesh elements used within t_{min}, the more accurate the bandpass projection shape is approximated. For minimum wall-thicknesses of three mesh elements and less, the intermediate material regions within the non-mixing region are relatively large compared to the total non-mixing region even for higher β_3 values ($\beta_3 < 50$). The size of the intermediate material regions within the non-mixing region is depending on the β_3 value, assuming a sufficiently high β_2 value is used ($\beta_2 \geq 50$). The total size of the non-mixing region depends on the value of t_{min}. If t_{min} is increased with the same β_3 value the total size of the non-mixing region is increased, while the size of the intermediate material regions remains the same. Increasing t_{min}, while β_3 remains the same, means that a relatively smaller part of the non-mixing region has intermediate material regions.The intermediate material regions lead to erroneous behaviour, meaning that the intermediate material regions within the non-mixing region do not accurately represent the physics. Therefore it is recommended to select a t_{min} value with a size of four or more mesh elements. To reduce the size of the intermediate material regions, a parameter continuation scheme on the β projection parameters is needed that is fine-tuned for the parameter settings used. The parameter continuation scheme also reduces the size of the region with slightly lowered flow penalization values if the condition $R_2 > t_{min}$ is used. Both an accaptable intermediate material regions and flow penalization region should be taken into account when selecting a β_{max} value. A maximum flow penalization value α_{max} must be selected to sufficiently penalize the flow in the solid material region and the fluid region corresponding to the other fluid. Passive material regions must be used in the in- and outflow regions of the fluid channels to guarantee that the non-mixing constraint can separate the fluid channels in the entire design domain with a non-mixing region. Passive solid material regions surrounding the active part of the design domain are recommended to prevent the forming of enclosed fluid regions. Two pressure drop constraints must be used to prevent the fluid channel diameter from becoming to narrow to be able to approximate the fluid flow in the fluid channels.

A

Comparing Objective Functions

In this appendix the domain boundary function used in the report is elaborated on. The domain objective function was implemented in the set-up phase of the thesis project and derived from a domain objective function from literature [6]. The objective function used in this report is different from the one in literature, but was verified to also maximize the total heat transfer in the design domain. The objective function was discovered by accident, but after applying the objective function in different optmization scenarios the effect did not show disadvantages. In the next section the domain objective function from literature and the derived objective function are expanded to show that they are different.

A.1. Domain Objective Functions

Eq. A.1 and A.2 show the domain objective function from literature and the expansion in terms:

$$J^{\mathbf{lit}}_{thermal}(\Omega) = \int\limits_{\Omega} (k(\nabla T)^2 + \rho_1 c_{p1} T(\mathbf{u}_1 \cdot \nabla T) + \rho_2 c_{p2} T(\mathbf{u}_2 \cdot \nabla T))d\Omega, \tag{A.1}$$

$$J^{\mathbf{lit}}_{thermal}(\Omega) = \int\limits_{\Omega} (k(T^2_{,x} + T^2_{,y}) + \rho_1 c_{p1} T(u_1 T_{,x} + v_1 T_{,y}) + \rho_2 c_{p2} T(u_2 T_{,x} + v_2 T_{,y}))d\Omega. \tag{A.2}$$

Eq. A.3, A.4 and A.5 show the derived objective function and the expansion in terms:

$$J_{thermal}(\Omega) = \int\limits_{\Omega} (k(||\nabla T||)^2 + \rho_1 c_{p1} T(||\mathbf{u}_1|| \cdot ||\nabla T||) + \rho_2 c_{p2} T(||\mathbf{u}_2|| \cdot ||\nabla T||))d\Omega. \tag{A.3}$$

$$\begin{aligned} J_{thermal}(\Omega) = \int\limits_{\Omega} (k(T^2_{,x} + T^2_{,y}) &+ \rho_1 c_{p1} T(\sqrt{u_1^2 + v_1^2}\sqrt{T^2_{,x} + T^2_{,y}}) \\ &+ \rho_2 c_{p2} T(\sqrt{u_2^2 + v_2^2}\sqrt{T^2_{,x} + T^2_{,y}}))d\Omega. \end{aligned} \tag{A.4}$$

$$\begin{aligned} J_{thermal}(\Omega) = \int\limits_{\Omega} (k(T^2_{,x} + T^2_{,y}) &+ \rho_1 c_{p1} T(\sqrt{u_1^2 T^2_{,x} + \underline{u_1^2 T^2_{,y}} + \underline{v_1^2 T^2_{,x}} + v_1^2 T^2_{,y}}) \\ &+ \rho_2 c_{p2} T(\sqrt{u_2^2 T^2_{,x} + \underline{u_2^2 T^2_{,y}} + \underline{v_2^2 T^2_{,x}} + v_2^2 T^2_{,y}}))d\Omega. \end{aligned} \tag{A.5}$$

Even though the term representing the thermal conductivity, first term in each objective function, is identical the complete objective functions are different. The difference is visible in the expanded convective heat transfer terms in Eq. A.2 and A.5. Where the contribution of the density, heat capacity and temperature are identical in each objective function, the contributions of the flow velocity and temperature gradients are different. The differences between the objective functions can be seen in the convective heat transfer terms. The derived objective function has additional cross terms, these cross terms are underlined in Eq. A.5. The cross terms represent the temperature gradients multiplied with the flow velocity perpendicular to the temperature gradients. The effect this has is that for a maximization formulation of the objective function, the heat transfer perpendicular to the flow velocity is also maximized. All flow velocity temperature gradient terms are squared and can never be negative. The total value of the objective function can therefore also not have a negative value. In a maximization formulation, the squared flow velocity temperature gradient terms will be maximized independent of the sign of the flow velocity temperature gradients. All convective terms corresponding to the same fluid field are added up and the squareroot is taken. The squareroot does not alter the sign of each term, but only scales the terms corresponding to the same fluid field. The derived objective function was discovered in the set-up phase of the project and was compared to the boundary objective function (Eq. A.6). The optimal results generated with each objective function showed similar improvements of the initial design. The derived objective functions was tried in a variety of optimization scenarios and improved the heat exchanger performance compared to the initial/reference designs in each scenario.

The cross terms in the derived objective function do not have a physical meaning, therefore further investigation is needed to determine if the objective function will perform consistently in all heat transfer optimization scenarios. It can be argued that the derived objective function is not valid due to the non-physical terms in the objective function. A possible argument against the derived objective function can be separated from the proposed non-mixing constraint. The non-mixing constraint always guarantees a minimum wall-thickness independent of the objective function used, since the non-mixing filter is a combined blurring- and projection-operation that is always performed on the second design variable. Depending on the objective function used, different gradient information is taken into account in the update algorithm and a wall with a larger thickness than the minimum wall-thickness can be generated. The objective function can not restrict the non-mixing constraint from forming a non-mixing region, it can only decide to locally generate more solid material around the minimum wall-thickness.

The derived objective function is also compared to the boundary objective function from literature [14] (Eq. A.6) in Appendix C Section C.1.

$$J_{temperature}(\Gamma_{in},\Gamma_{out}) = \int\limits_{\Gamma_{in}} (T(\mathbf{u}\cdot\mathbf{n}))d\Gamma_{in} - \int\limits_{\Gamma_{out}} (T(\mathbf{u}\cdot\mathbf{n}))d\Gamma_{out}, \tag{A.6}$$

B

Impossible Design

In this appendix a 2D crossing channels design is used to determine the robustness of the non-mixing constraint. The design flips the outlet of the coolant with the inlet of the to be cooled fluid, so the channels will cross in the design domain. Since a 2D design domain is used the forward analysis of the physics, specifically the velocity and pressure field, can not be accurately represented if the flow penalization and non-mixing constraint function properly. The only solution that can be found is one where one of the fluids flows through the fluid channel of the other fluid.

B.1. 2D Crossing Channels Heat Exchanger

In an optimization scenario where the in- and outlet on one side of the design domain are flipped, the fluids have to cross somewhere in the design domain. Physically this should not be possible, as one fluid has to leak through two non-mixing regions and the other fluid. Leakage is here defined as one fluid flowing in the solid regions or in the region of the other fluid even though the fluid flow is penalized. To some extent leakage is acceptable, since the flow is not penalized to zero. However, two crossing channels should not be able to connect in a 2D design domain. The heat exchanger has a counter-flow configuration, with two identical fluids. Table B.1 shows the values used for the dimensions of the design domain as shown in Fig. 3.14, the values used for the filtering and projection parameters and the values of the remaining parameters. During the optimization process, the values for β_1, β_2 and β_3 are increased from 8 to 100.

Dimensional Parameters	Values	Filter and Projection Parameters	Values	Parameters	Values
L1	1 [m]	R_1	0.03 [m]	h	0.01 [m]
L2	1 [m]	β_1	8-100 [-]	$T_{in,f2}$	293.15 [K]
L3	0.05 [m]	R_2	0.03 [m]	$T_{in,f1}$	333.15 [K]
L4	0.1 [m]	β_2	8-100 [-]	Re_1	10 [-]
L5	0.015 [m] (t_{min})	t_{min}	0.015 [m]	Re_2	10 [-]
L6	0.25 [m]	β_3	8-100 [-]	C_1	100,500 and 1000 [-]
				C_2	2 [-]

Table B.1: Parameter values used in optimization scenarios.

In all previous optimization scenarios one fluid has an in- and outlet in the bottom of the design domain at the same height, and the other fluid has both the in- and outlet at a pre-specified distance from the bottom channel on top of it. For a heat exchanger with crossing channels the inlet and outlet on one side of the domain have to be flipped. Fig B.1 shows the fluid region corresponding to the coolant and the to be cooled fluid. The coolant flows into the design domain at the bottom left and flows out of the domain at the top right (Fig. B.1a), while the to be cooled fluid flows into the design domain at the bottom right and flows out of the domain at the top left (Fig. B.1b).

(a) Design domain available for the coolant.

(b) Design domain available for the the to be cooled fluid.

Figure B.1: Fluid regions corresponding to the coolant (water) and to be cooled fluid (oil).

An initial design that connects both channels in a 2D heat exchanger with crossing channels can not be provided. Instead to allow the optimization to start an initial design with intermediate values has to be used. Fig B.2 shows the initial design used for each design variable.

(a) Field values used in initial design for the field of θ_1, denoting the solid region with $\theta_1 = 1$ and the fluid region with $\theta_1 = 0$.

(b) Field values used in the initial design for the field of θ_2, denoting the coolant with $\theta_2 = 0$ and the to be cooled fluid with $\theta_2 = 1$).

Figure B.2: Field values used in initial designs for both design variables.

The first optimal design is generated with flow penalization parameter C_1 set to 100 as shown in Fig. B.3. Even though the materials are defined correctly in the corresponding material regions and the non-mixing constraint places a non-mixing region between the fluids, the physics can still be solved. The reason this velocity field can still be solved is because the flow is not penalized to 0, but to a flow velocity that is significantly lower than that in the non-penalized fluid regions. To show the leakage behaviour the normalized flow velocity of both fluids is plotted together with the normalized thermal conductivity to show the solid regions, see Fig. B.3b. The three field are evaluated at the black centerline shown in Fig. B.3a. The flow field shows that the coolant is leaking through the non-mixing constraints and other fluid. Fig. B.3c shows that even though one fluid is leaking through the other fluid, the pressure drop constraint is barely violated. During the optimization process the pressure drop switched between violated and not violated for a projection sharpness of $\beta \geq 60$.

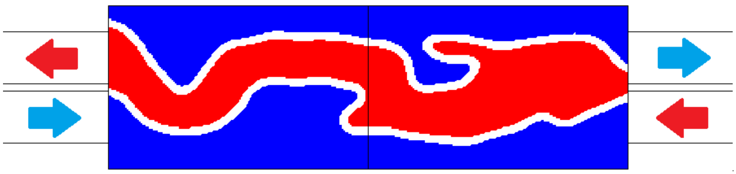

(a) Fluid regions with the coolant in blue and the to be cooled fluid in red.

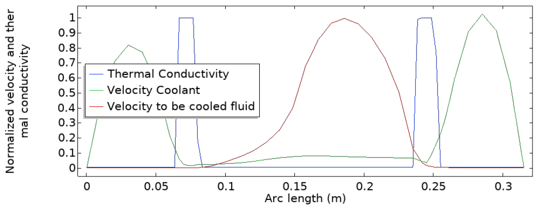

(b) Fluid leakage in the design domain.

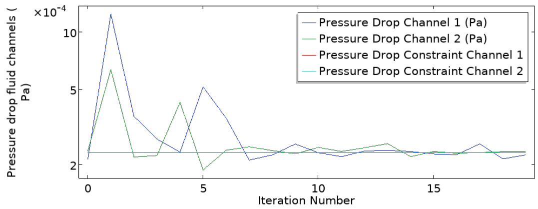

(c) Pressure drop with maximum allowable pressure drop as a reference.

Figure B.3: Crossing channel design generated with $C_1 = 100$ and $\beta = 100$.

In the next optimization the value for C_1 is increased to 500. The results show that the coolant is still leaking through the non-mixing constraints and other fluid. At least one of the pressure drop constraints is violated for $\beta \geq 40$. The pressure drop violation is significantly larger than with $C_1 = 100$.

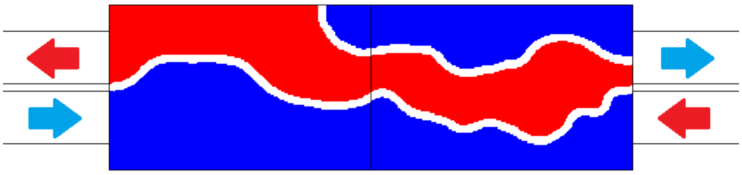

(a) Fluid regions with the coolant in blue and the to be cooled fluid in red.

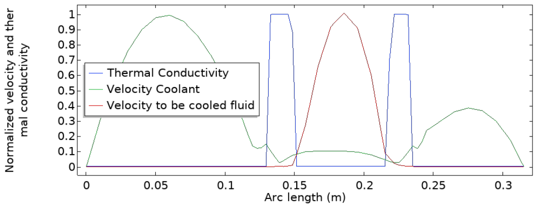

(b) Fluid leakage in the design domain.

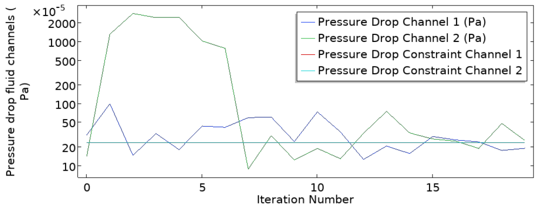

(c) Pressure drop with maximum allowable pressure drop as a reference.

Figure B.4: Crossing channel design generated with $C_1 = 500$ and $\beta = 100$.

By further increasing the C_1 value to a 1000, the penalization value is high enough to guarantee failure of the forward analysis. The optimization algorithm fails to solve the physics for $\beta = 14$. The result shown in Fig. B.5 is the last result generated with $\beta = 12$. Fig. B.5c shows that both pressure drop constraints are violated, even more so than with C_1 is equal to 100 and 500.

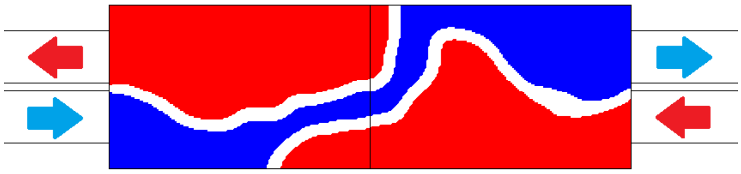

(a) Fluid regions with the coolant in blue and the to be cooled fluid in red.

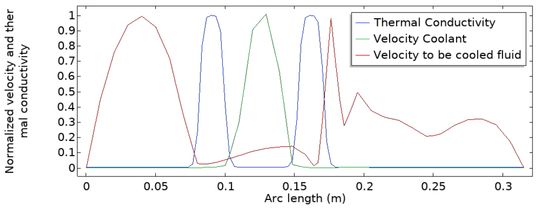

(b) Fluid leakage in the design domain.

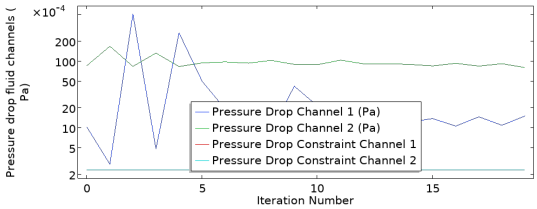

(c) Pressure drop with maximum allowable pressure drop as a reference.

Figure B.5: Crossing channel design generated with $C_1 = 1000$ and $\beta = 12$.

The two essential parameters that determine the leakage behaviour are the value selected for C_1 and the value selected for C_2. The value for C_2 determine what the maximum allowable pressure drop is and therefore the violation criteria. Thus, depending on the value for the scaling term of the maximum allowable pressure drop (C_2), a fitting value for the penalization scaling term (C_1) should be selected. What a fitting value for C_1 is depends on the accuracy with which the physics should be described. In other words, a too low value for C_1 allows for to much leakage and the physics will not be described accurately. A value for C_1 selected too high could lead to poor convergence behaviour. Selecting the fitting value for C_1 therefore requires some fine-tuning. It has to be mentioned that a 2D crossing channel heat exchanger forces the fluids to leak through the solid regions and the region of the other fluid. With similar 2D optimization set-up, where the fluids are not forced to flow through one-another, this leaking behaviour occurs significantly less, see Section D.1. In these scenarios the fluid channels start separated and there is no necessity for one fluid to flow through the other fluid channel. The optimizer improves the design by elongating the fluid channels with the same maximum allowable pressure drop. To determine the accuracy of the physics a forward analysis of a discrete version of the optimal design can be performed. If the discrete design is compared with the optimal design generated by the optimization algorithm, the differences in the physics will show the accuracy of the optimal design. A forward analysis with a discrete design can only be performed with a feasible design, since a crossing channels

2D design is not feasible an accuracy check of the physics can not be performed.

In the final stage of the project this Chapter was revised and the passive regions were implemented. To verify if passive regions improve the flow penalization behaviour, the crossing channels design is re-computed with $C_1 = 500$ and the in- and outflow regions now passive. Fig. B.6 shows the regions defined as passive regions. The blue regions correspond to the coolant and the red regions correspond to the to be cooled fluid.

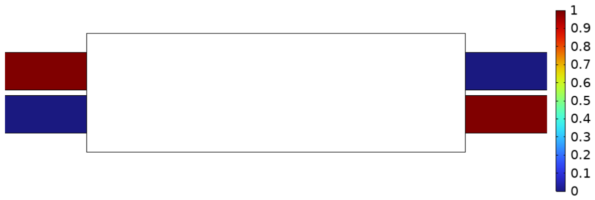

Figure B.6: Regions defined as passive regions in the optimization algorithm.

Fig. B.7 shows the optimal design generated with the passive regions and $C_1 = 500$. Even though the optimization settings apart from the passive regions are identical to the settings used in Fig. B.4, the pressure drop constraints are violated from the initial β value ($\beta = 8$) up to $\beta = 100$. The pressure drop constraint violations are now higher than without passive regions. In other words the passive regions improve the flow penalization behaviour and are therefore recommended to use with the non-mixing constraint.

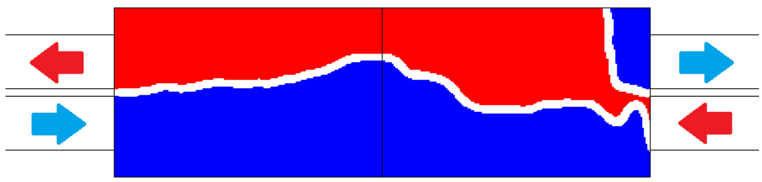

(a) Fluid regions with the coolant in blue and the to be cooled fluid in red.

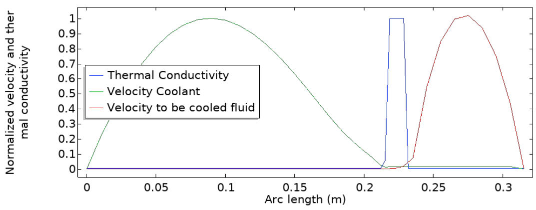

(b) Fluid leakage in the design domain.

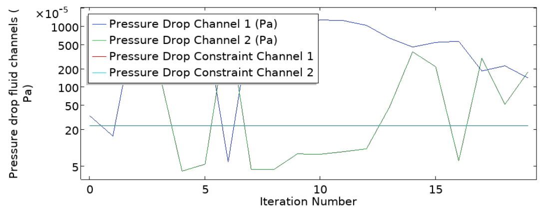

(c) Pressure drop with maximum allowable pressure drop as a reference.

Figure B.7: Crossing channel design generated with $C_1 = 500$, $\beta = 100$ and passive regions.

The optimization set-up with the crossing channels design could never generate feasible designs, therefore it is only used to investigate the penalization behaviour and the robustness of the non-mixing constraint. For the optimization algorithm to start, an intermediate design has to be used as an initial design. The optimization behaviour depends here strongly on the value selected for the penalization scaling term (C_1). If C_1 is selected too low the fluids are not penalized enough and can still flow freely even if the fluid flow in that region is penalized. The fluids can therefore easily leak through the non-mixing regions and other fluid without violating the pressure drop constraints. If the value for C_1 is selected high enough two types of behaviour were noticed. The first is a constant violation of at least one of the pressure drop constrainst from a certain β value on, but the optimization algorithm does not fail to solve the physics. The reason the optimizer can solve the physics is that C_1 is selected to penalize the flow enough, but not completely. In the region where one of the fluids is penalized the velocity field of this same fluid is not 0, but an extremely low value. With these extremely low flow velocities the velocity and pressure field can be computed, but at least one of the pressure drop constraints is violated. The second behaviour is failure in computing the velocity and pressure field leading to stopping of the optimization process. Further increasing the C_1 values can minimize the flow velocity of a fluid in the penalized regions. However, if a C_1 value is selected too high, the fluids are forced apart in the regions with intermediate values for larger filter radii and low β values. When the β values are increased this effect is reduced, but can lead to extreme differences in the physics with β increments and poor convergence behaviour. Using passive regions for the in- and outflow regions further improved the flow penalization behaviour and the use of passive regions is therefore recommended. Even though the selection of the maximum penalization value does not alter the concept of the non-mixing constraint, the value should selected sufficiently high to make the non-mixing constraint function properly.

C
2D Heat Exchanger: Non-Mixing Constraint

In this appendix, the optimization scenarios used in Chapter 4 are also computed with the derived domain objective function as provided in Eq. 3.29. In Section C.1 the domain objective function is compared to the boundary objective function. The investigation of the interpolation behaviour is not performed with the domain objective function, since the interpolation functions are not altered and are independent of the objective function. In Section C.2 the function used to approximate the filter radius R_3 with the minimum wall-thickness t_{min} is verified. In Section C.3 the forming of a variable wall-thickness by the optimizer is elaborated on.

C.1. Domain & Boundary Objective Function

In this section the domain and boundary objective function are compared to determine if the optimization behaviour changes significantly. Eq. C.1 shows the domain objective function and Eq. C.2 shows the boundary objective function.

$$J_{thermal}(\Omega) = \int_{\Omega} (k(\hat{\tilde{\theta}}_1, \hat{\tilde{\theta}}_2, \hat{\tilde{\theta}}_3)(||\nabla T||)^2 + \rho_1 c_{p1} T(||\mathbf{u}_1|| \cdot ||\nabla T||) + \rho_2 c_{p2} T(||\mathbf{u}_2|| \cdot ||\nabla T||)) d\Omega. \tag{C.1}$$

$$J_{temperature}(\Gamma_{in}, \Gamma_{out}) = \int_{\Gamma_{in}} (T_{in} \cdot \mathbf{u}_{in} \cdot n) d\Gamma_{in} - \int_{\Gamma_{out}} (T_{out} \cdot \mathbf{u}_{out} \cdot n) d\Gamma_{out}, \tag{C.2}$$

The objective functions are both normalized and transformed to a minimization form with the inverse approach as shown in Eq. 3.30. In this optimization scenario a counter-flow heat exchanger configuration with identical fluids (both fluids are water) is used. The coolant flows into the design domain at the left-side, while the to be cooled fluid flows into the design domain at the right-side. Table C.1 shows the values used for the dimensions of the design domain as shown in Fig. 3.14, the values used for the filtering and projection parameters and the values of the remaining parameters. During the optimization process the value for β_1, β_2 and β_3 is increased from 8 to 100.

Dimensional Parameters	Values	Filter and Projection Parameters	Values	Parameters	Values
L1	1 [m]	R_1	0.03 [m]	h	0.01 [m]
L2	0.315[m]	β_1	8-100 [-]	$T_{in,f1}$	293.15 [K]
L3	0.05 [m]	R_2	0.03 [m]	$T_{in,f2}$	333.15 [K]
L4	0.1 [m]	β_2	8-100 [-]	Re_1	10 [-]
L5	0.015 [m] (t_{min})	t_{min}	0.015 [m]	Re_2	10 [-]
L6	0.25 [m]	β_3	8-100 [-]	C_1	500 [-]
				C_2	2.5 [-]

Table C.1: Parameter values used in optimization scenarios.

The optimal design generated with the domain objective funtion is provided in Fig. C.1a. The optimal design generated with the boundary objective funtion is provided in Fig. C.1b. To investigate if adding the passive regions (see Section 3.4.3) will alter the optimization behaviour, the same scenarios are re-computed with passive regions. The optimal design generated with the domain objective function and passive regions is provided in Fig. C.1c. The optimal design generated with the boundary objective function and passive regions is provided in Fig. C.1d.

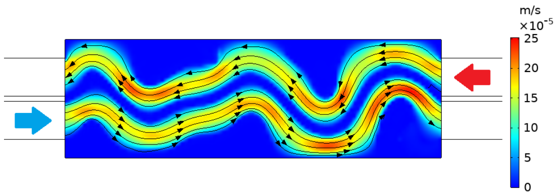

(a) Velocity field of optimal design with the domain integral objective. The thermal efficiency is 30.363%.

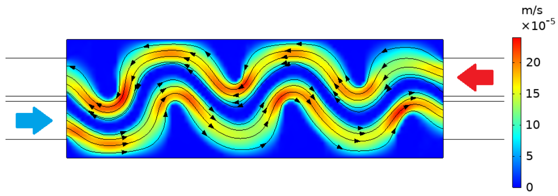

(b) Velocity field of optimal design with the boundary integral objective and passive regions. The thermal efficiency is 30.488%.

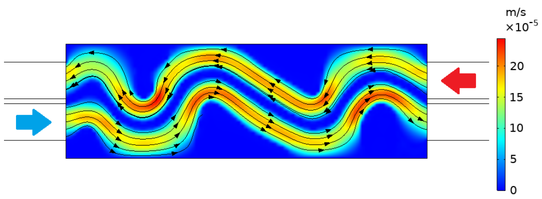

(c) Velocity field of optimal design with the domain integral objective. The thermal efficiency is 30.279%.

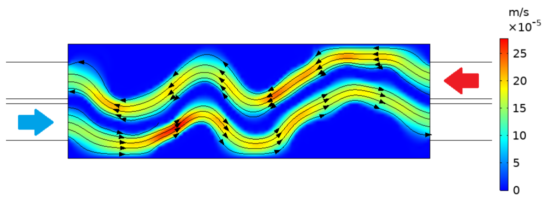

(d) Velocity field of optimal design with the boundary integral objective and passive regions. The thermal efficiency is 29.559%.

Figure C.1: Optimal desings generated with the domain and boundary integral.

The results show that boundary objective function has a performance that is slightly higher in the optimization scenario without passive regions (30.363% < 30.488%) and slightly lower in the optimization scenario with passive regions (30.279% > 29.559%). In all optimization scenarios the optimizer generated elongated tortuous fluid channels. However, the optimal designs generated with each objective function are different. The two optimal designs generated with the domain objective function show similarites near the in- and outflow regions, but the remainder of the design is mirrored over the vertical centerline of the design domain. The two optimal designs generated with the boundary objective function show no resemblance apart from the flow direction near the in- and outflow regions. The boundary objective function had convergence issues for higher β values in the optimization scenario without passive regions. The parameter continuation scheme was fine-tuned for the domain objective function, which could be the reason it did not perform in a similar manner with the boundary objective function. The convergence issues were not further investigated. Since both the domain and the boundary objective functions generated optimal designs that performed in a similar range, the domain objective function seems to perform adequately.

C.2. Minimum Wall-Thickness

In this section the minimum wall-thickness (t_{min}) is varied to determine its influence on the optimization behaviour using the domain objective function. In addition, the pre-set t_{min} value and the actual minimum wall-thickness generated by the optimizer are compared. For this optimization problem two identical fluids (both water) are used with a counter-flow heat exchanger configuration. Table C.2 shows the values used for the dimensions of the design domain, the values used for the filtering and projection parameters and the values of the remaining parameters. During the optimization process the value for β_1 and β_2 is increased from 8 to 100 and β_3 is increased from 2 to 100. For the minimum wall-thickness (t_{min}) a parameter sweep is performed with the values 0.015 [m], 0.020 [m] and 0.025 [m]. The reason for selecting these values for the minimum wall-thickness is that the difference between the t_{min} values is large enough to be visible in the optimal designs.

Dimensional Parameters	**Values**	**Filter and Projection Parameters**	**Values**	**Parameters**	**Values**
L1	1 [m]	R_1	0.03 [m]	h	0.01 [m]
L2	0.315[m]	β_1	8-100 [-]	$T_{in,f1}$	293.15 [K]
L3	0.05 [m]	R_2	0.03 [m]	$T_{in,f2}$	333.15 [K]
L4	0.1 [m]	β_2	8-100 [-]	Re_1	10 [-]
L5	0.015 [m] (t_{min})	t_{min}	0.015 [m]	Re_2	10 [-]
L6	0.25 [m]	β_3	2-100 [-]	C_1	500 [-]
				C_2	3 [-]

Table C.2: Parameter values used in optimization scenarios.

Fig. C.2 shows the optimal results generated with t_{min} set to 0.015 [m]. Since the set-up allows for a variable wall-thickness, the exact location where the wall-thickness is the minimum wall-thickness is unknown. To check if the wall-thickness does not become thinner than the minimum wall-thickness, the wall-thickness is evaluated at the location where the wall is thinnest. The location where the wall is thinnest for $t_{min} = 0.015$ [m], is shown in Fig. C.2c (white line) with a wall-thickness of 0.0153 [m]. Fig. C.3 shows the optimal result generated with $t_{min} = 0.020$ [m]. The location where the wall is thinnest for $t_{min} = 0.020$ [m], is shown in Fig. C.3c (white line) with a wall-thickness of 0.0202 [m]. Fig. C.4 shows the optimal result generated with $t_{min} = 0.025$ [m]. The location where the wall is thinnest for $t_{min} = 0.025$ [m], is shown in Fig. C.4c (white line) with a wall-thickness of 0.0261 [m].

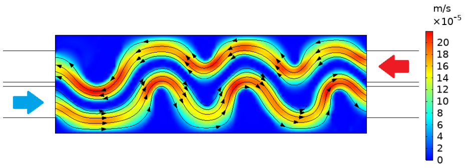

(a) Velocity field.

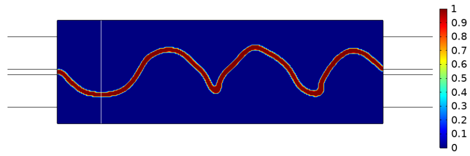

(b) Non-mixing region generated with the non-mixing variable $\hat{\theta}_3$.

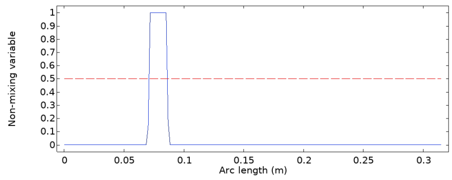

(c) Minimum wall-thickness of 0.0153 [m] evaluated at white line in Fig. C.2b.

Figure C.2: Optimal design generated with $t_{min} = 0.015$ [m].

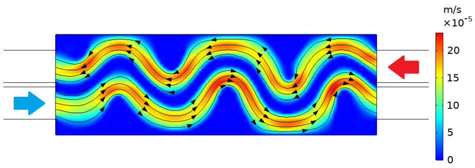

(a) Velocity field.

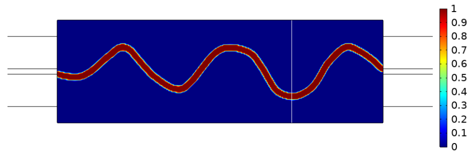

(b) Non-mixing region generated with the non-mixing variable $\hat{\theta}_3$.

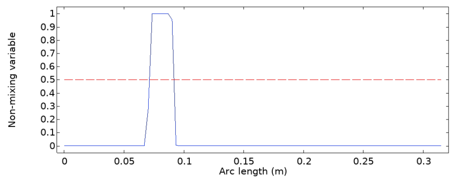

(c) Minimum wall-thickness of 0.0205 [m] evaluated at white line in Fig. C.3b.

Figure C.3: Optimal design generated with $t_{min} = 0.020$ [m].

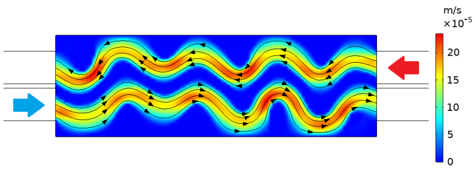

(a) Velocity field.

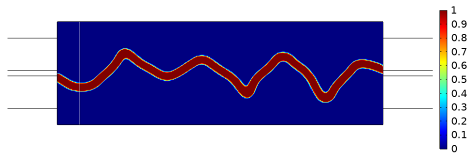

(b) Non-mixing region generated with the non-mixing variable $\hat{\theta}_3$.

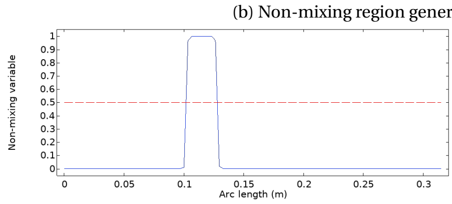

(c) Minimum wall-thickness of 0.0261 [m] evaluated at white line in Fig. C.4b.

Figure C.4: Optimal design generated with $t_{min} = 0.025$ [m].

Comparing the pre-set t_{min} values to the measured minimum wall-thicknesses, the non-mixing constraint adequately generates minimum wall-thicknesses near the pre-set t_{min} values. It is also visible that altering the minimum wall-thickness changes the optimization behaviour. In all scenarios a tortuous fluid channel is generated to elongate the fluid channels and improve the heat transfer. However, when the minimum wall-thickness is altered the region available for folding the fluid channels is also altered. A design with a wall-thickness smaller than t_{min} can not be generated. If the value for t_{min} is increased, the design previously generated with a t_{min} value that was lower can not be generated anymore.

C.3. Variable Wall-Thickness

In this section the different approaches that the optimizer can use to generate a variable wall-thickness with the non-mixing constraint are examined. A solid domain can be defined as the regions where $\hat{\hat{\theta}}_1 = 1$ or as the regions where $\hat{\hat{\theta}}_3 = 1$ (non-mixing filter is active). A wall with a variable thickness ($t_{wall} > t_{min}$) seperating the two fluids is thus constructed by adding solid material ($\hat{\hat{\theta}}_1 = 1$) around the minimum wall-thickness generated by the non-mixing constraint ($\hat{\hat{\theta}}_3 = 1$. In the set-up phase of the optimization algorithm an additional approach the optimizer could use to generate a variable wall-thickness was noticed. The optimizer generated large intermediate regions with $\hat{\hat{\theta}}_2 = 1$ that are then filtered and projected with the non-mixing filter to generate a wall with a variable thickness.

C.3.1. Variable Wall-Thickness: Approach 1

In the first approach the variable wall-thickness is constructued by adding solid material generated with the first design variable ($\hat{\hat{\theta}}_1 = 1$) to the minimum wall-thickness generated by the non-mixing filter ($\hat{\hat{\theta}}_3 = 1$). The heat exchanger configuration used in the optimizatiopn scenario to show the forming of the variable wall-thickness with the first approach is a counter-flow configuration with two identical fluids, both fluids are water. The coolant flows into the design domain on the right-side (bottom channel), while the to be cooled fluid flows into the design domain on the left-side. Table C.3 shows the values used for the dimensions of the design domain as shown in Fig. 3.14, the values used for the filtering and projection parameters and the values of the remaining parameters. During the optimization process the value for β_1, β_2 and β_3 is increased from 2 to 160.

Dimensional Parameters	Values	Filter and Projection Parameters	Values	Parameters	Values
L1	0.5 [m]	R_1	0.03 [m]	h	0.01 [m]
L2	0.5[m]	β_1	2-160 [-]	$T_{in,f1}$	293.15 [K]
L3	0.05 [m]	R_2	0.03 [m]	$T_{in,f2}$	333.15 [K]
L4	0.1 [m]	β_2	2-160 [-]	Re_1	10 [-]
L5	0.35 [m] (t_{min})	t_{min}	0.05 [m]	Re_2	10 [-]
L6	0.25 [m]	β_3	2-160 [-]	C_1	100 [-]
				C_2	3 [-]

Table C.3: Parameter values used in optimization scenarios.

Fig. C.5 shows an optimal design with a variable wall-thickness generated with the first approach. The total solid material region is provided in Fig. C.5b, the solid material region is here expressed with the thermal conductivity. The non-mixing region separating the two fluids has avariable wall-thickness. The solid regions generated with $\hat{\hat{\theta}}_1$ are shown in Fig. C.5c and the solid region generated with $\hat{\hat{\theta}}_3$ (non-mixing variable) is shown in Fig. C.5d. The figures show that the non-mixing variable $\hat{\hat{\theta}}_3$ guarantees the minimum wall-thickness between the fluids and additional solid material is generated with $\hat{\hat{\theta}}_1$ forming a varialbe wall-thickness. The solid material generated with $\hat{\hat{\theta}}_1$ can overlap with the solid material generated with $\hat{\hat{\theta}}_3$, since the interpolation functions combine the two solid material fields and compensate for the overlapping solid material regions.

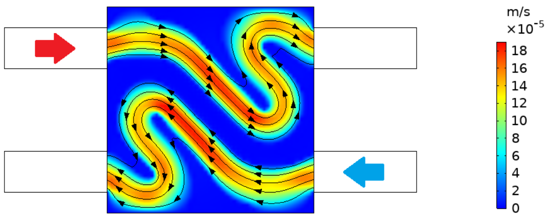

(a) Velocity field optimal design.

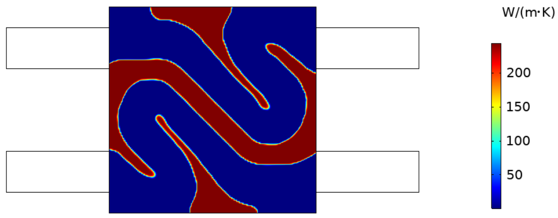

(b) Total region of solid material expressed with the thermal conductivity.

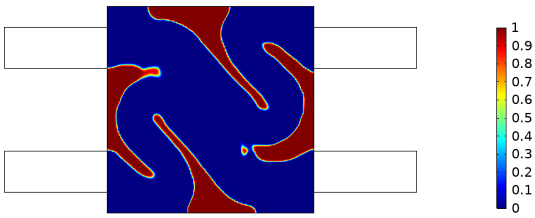

(c) Solid region generated by the first design variable ($\hat{\hat{\theta}}_1$).

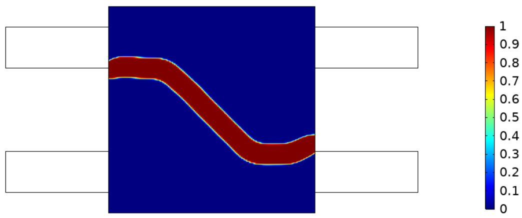

(d) Solid region generated by the non-mixing design variable ($\hat{\hat{\theta}}_3$).

Figure C.5: The interpolation functions allow the wall-thickness to vary, while a minimum wall-thickness is guaranteed.

The small solid island, floating near the center of the design domain, in Fig. C.5c is a reminant from a solid region that was initially connected to the solid region on the right side of the island. The non-mixing constraint generates a solid region in the same location as the solid island, thereby connecting the solid island to the other solid material regions, see Fig. C.5b.

C.3.2. Variable Wall-Thickness: Approach 2

The second approach to generate a variable wall-thickness is by allowing the second term of the alternative interpolation functions (Eq. 3.21 and 3.22) to generate a wall with a larger thickness than the minimum wall-thickness. The optimizer can generate these regions by generating larger intermediate material regions with $\hat{\hat{\theta}}_2$. The generated intermediate material regions are within the projection bandwidth of the bandpass-projection function and are therefore completely projected to a solid material region. The optimization scenario used has a parallel-flow heat exchanger configuration with two identical fluids, both water. Table C.4 shows the values used for the dimensions of the design domain as shown in Fig. 3.14, the values used for the filtering and projection parameters and the values of the remaining parameters. During the optimization process the value for β_1, β_2 and β_3 is increased from 2 to 20.

Dimensional Parameters	**Values**	**Filter and Projection Parameters**	**Values**	**Parameters**	**Values**
L1	1 [m]	R_1	0.03 [m]	h	0.01 [m]
L2	1[m]	β_1	2-20 [-]	$T_{in,f1}$	293.15 [K]
L3	0.05 [m]	R_2	0.03 [m]	$T_{in,f2}$	353.15 [K]
L4	0.1 [m]	β_2	2-20 [-]	Re_1	10 [-]
L5	0.015 [m] (t_{min})	t_{min}	0.015 [m]	Re_2	10 [-]
L6	0.25 [m]	β_3	2-20 [-]	C_1	100 [-]
				C_2	8 [-]

Table C.4: Parameter values used in optimization scenarios.

An optimal design that is generated with the second approach is shown in Fig. C.6. Fig. C.6b shows the total region defined as solid material. To show that the variable wall-thickness is generated with the non-mixing variable $\hat{\hat{\theta}}_3$ only, the contribution of $\hat{\hat{\theta}}_1$ and $\hat{\hat{\theta}}_3$ to the total solid material region is shown separately. The solid region generated with $\hat{\hat{\theta}}_1$ is shown in Fig. C.6c, while the solid region generated with $\hat{\hat{\theta}}_3$ is shown in Fig. C.6d. The figures show that the entire variable wall-thickness between the fluids is generated with $\hat{\hat{\theta}}_3$.

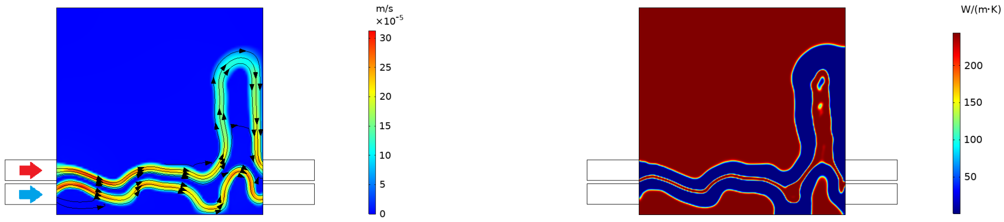

(a) Velocity field optimal design.

(b) Total region of solid material.

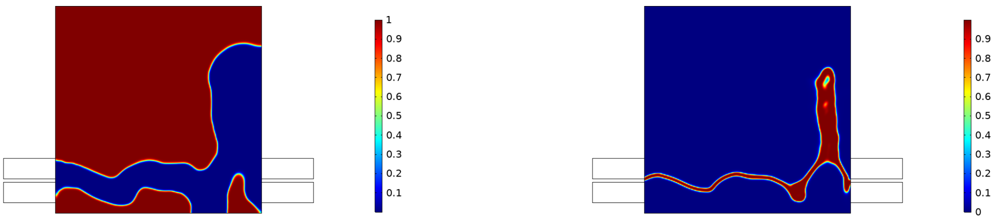

(c) Solid region generated by the first design variable ($\hat{\hat{\theta}}_1$).

(d) Solid region generated by the non-mixing design variable ($\hat{\hat{\theta}}_3$).

Figure C.6: The interpolation functions allow the wall-thickness to vary, while a minimum wall-thickness is guaranteed.

To show the origin of the non-mixing region with a variable wall-thickness, the field values of $\hat{\hat{\theta}}_2$ are checked. Fig. C.7a shows the field values of the design variable $\hat{\hat{\theta}}_2$. Fig. C.7b shows the solid region generated with $\hat{\hat{\theta}}_3$. Since $\hat{\hat{\theta}}_3$ is the filtered and projected $\hat{\hat{\theta}}_2$ variable it can be seen that the larger intermediate regions of $\hat{\hat{\theta}}_2$ result in wall-thicknesses larger than the minimum wall-thickness. The bandpass-projection function projects all intermeidate $\hat{\hat{\theta}}_2$ values in between 0.1 and 0.9 to a solid material region. If the optimizer generates larger intermediate regions with $\hat{\hat{\theta}}_2$, the solid regions will also become larger.

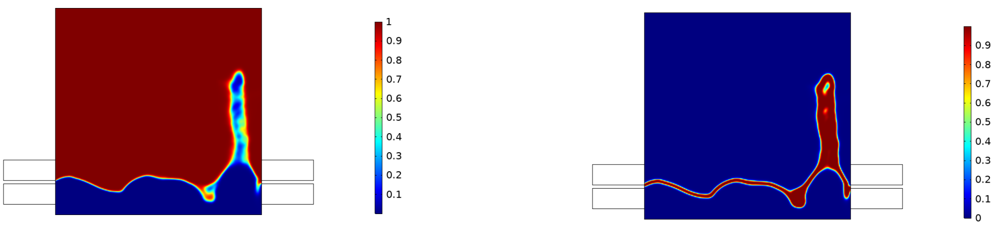

(a) Field values of $\hat{\hat{\theta}}_2$.

(b) Total region of solid material.

Figure C.7: The field values of $\hat{\hat{\theta}}_2$ used in the non-mixing filter to generate the non-mixing region.

It was not found that the additional approach to generate a variable wall-thickness had a disadvantages effect. The intermediate regions of $\hat{\hat{\theta}}_2$ are not visible in the optimal designs, since these intermediate regions are filtered and projected to more dsicrete designs with the non-mixing filter. The second approach to generate a variable wall-thickness occurs more dominantly for lower β values ($\beta < 20$), the effect decays with β increments. The second approach to generate a variable wall-thickness could originate from the objective functions used. The derived objective function has additional cross terms as explained in Appendix A.1, that could generate this effect. The effect was not seen with the boundary objective function.

D

2D Heat Exchanger: Reproducing Results

In this appendix, the optimization scenarios used in Chapter 5 are also computed with the derived domain objective function as provided in Eq. 3.29. The alternative interpolation functions are compared to the original interpolation functions from literature [14] in similar optimization scenarios. The derived objective function does not require the additonal passive solid regions surrounding the active design domain to prevent the forming of enclosed fluid regions. The passive solid regions are therefore not implemented in the optimization scenarios. The derived interpolation functions showed less convergence issues for higher β values and the β_{max} value is increased to 100 instead of 80 for more discrete optimal designs.

D.1. Density-based method

In this section the alternative interpolation functions provided in Eq. 3.21 and 3.22 are compared to the original interpolation functions from literature:

$$\alpha_1(\hat{\tilde{\theta}}_1,\hat{\tilde{\theta}}_2) = a_{1,max}\left(1-(1-\hat{\tilde{\theta}}_1^p)(1-\hat{\tilde{\theta}}_2^p)\right). \tag{D.1}$$

$$\alpha_2(\hat{\tilde{\theta}}_1,\hat{\tilde{\theta}}_2) = a_{2,max}\left(1-(1-\hat{\tilde{\theta}}_1^p)(1-(1-\hat{\tilde{\theta}}_2)^p)\right). \tag{D.2}$$

The original interpolation functions can also generate a variable wall-thickness. The drawback of the original interpolation functions is that a zero wall-thickness can be generated. The alternative interpolation functions guarantee a minimum wall-thickness, while still allowing the forming of a variable wall-thickness. Since the original interpolation function for the thermal conductivity can not distinguish between two different fluids, the extended thermal conductivity interpolation function is used as provided in Eq. 3.23. The goal here is to determine if the alternative interpolation functions alter the optimization behaviour significantly. In both optimization problems a counter-flow heat exchanger configuration is used. The coolant flows into the design domain at the left-side, while the to be cooled fluid flows into the design domain at the right-side. Table D.1 shows the values used for the dimensions of the design domain as shown in Fig. 3.14, the values used for the filtering and projection parameters and the values of the remaining parameters. During the optimization process, the values for β_1 and β_2 are increased from 8 to 100 and β_3 is increased from 2 to 100. The two sets of interpolation functions are compared in an optimizaiton scenario with two identical fluids and two different fluids.

Dimensional Parameters	**Values**	**Filter and Projection Parameters**	**Values**	**Parameters**	**Values**
L1	1 [m]	R_1	0.03 [m]	h	0.01 [m]
L2	0.315[m]	β_1	8-100 [-]	$T_{in,f1}$	293.15[K]
L3	0.05 [m]	R_2	0.03 [m]	$T_{in,f2}$	333.15[K]
L4	0.1 [m]	β_2	8-100 [-]	Re_1	10 [-]
L5	0.015 [m] (t_{min})	t_{min}	0.015 [m]	Re_2	10 [-]
L6	0.25 [m]	β_3	2-100 [-]	C_1	500 [-]
				C_2	3 [-]

Table D.1: Parameter values used in optimization scenarios.

D.1.1. Two Identical Fluid Optimization Results

Fig. D.1 shows the optimal results generated with the original and the alternative interpolation functions. The fields of the optimal design generated with the original interpolation functions are provided on the left-side in Fig. D.1 (D.1a, D.1c, D.1e and D.1g). The optimal result has a mixing fluids design, since the fluids are not separated with a solid region in the entire design domain. On the left-side in the design domain, the optimizer generated a solid region between the two fluids with a variable wall-thickness as shown in Fig. D.1e. The solid region is generated to elongate the fluid channel to improve the heat transfer as shown in Fig. D.1c, where the temperature drops visibly in the region where the solid region is generated. The objective and thermal efficiency value of the optimal design are $6.3547E6$[kg m K/s^3] and 26.574%. The fields of the optimal design generated with the alternative interpolation functions are provided on the right-side in Fig. D.1 (Fig. D.1b, D.1d, D.1f and D.1h). The non-mixing constraint prevents mixing of the two fluids as shown in Fig. D.1f. The wall-thickness has an almost constant thickness in the entire design domain. To investigate the locally generated wall-thickness, a cross-section of the non-mixing region is analysed. The local wall-thickness in the optimal design is evaluated at the white line in Fig. D.1b and has a wall-thickness of ≈ 0.015[m], which is equal to the pre-set minimum wall-thickness $t_{min} = 0.015$[m]. The objective and thermal efficiency value of the optimal design are $7.3935E6$[kg m K/s^3] and 30.179%.

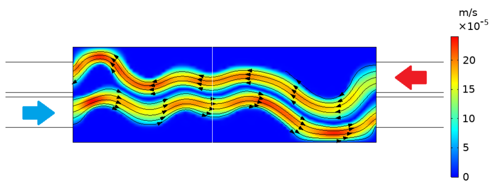

(a) Velocity field .

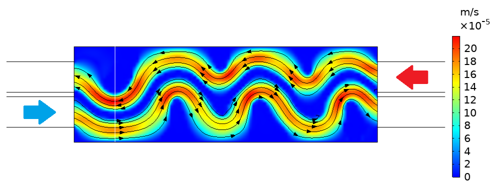

(b) Velocity field.

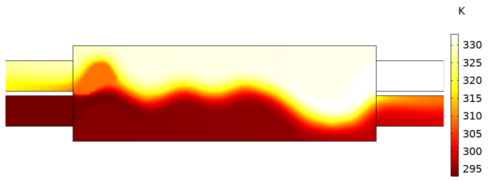

(c) Temperature field, with an objective value of $6.3547E6$ [kg m K/s^3] and a thermal efficiency value of 26.574%.

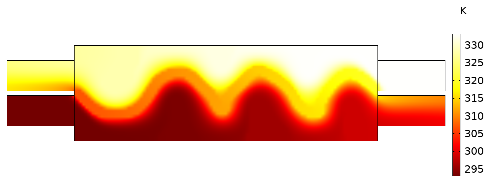

(d) Temperature field, with an objective value of $7.3935E6$ [kg m K/s^3] and a thermal efficiency value of 30.179%.

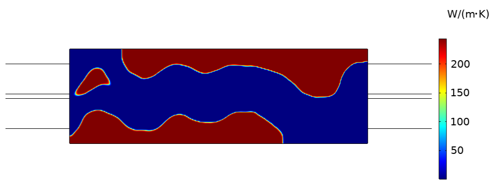

(e) Thermal conductivity field.

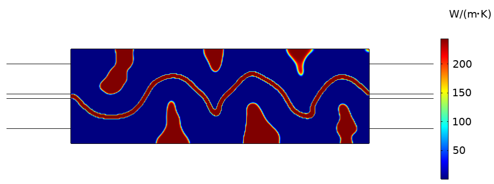

(f) Thermal conductivity field.

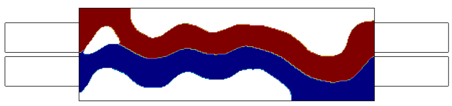

(g) Fluid regions.

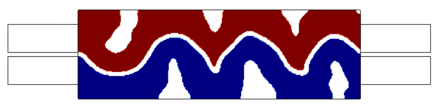

(h) Fluid regions.

Figure D.1: Optimal results generated with the original and alternative set of interpolation functions in the identical fluids scenario. The optimal results generated with the original set is provided on the left-side, while the optimal result generated with the alternative set is provided on the right-side.

It was expected that the original interpolation functions would generate a design with a higher thermal efficiency, since the fluids can be in direct contact and can therefore exchange thermal energy directly. The difference in objective value and thermal efficiency originates from the shape of the fluid channels. The set-up with the original interpolation functions generates thinner fluid channels with a slightly tortuous shape and the optimizer does not make use of the entire design domain. The set-up with alternative interpolation functions generates a tortuous design spread out over the entire design domain. Comparing the pressure drops of the optimal designs, the optimizer makes full use of the pre-set maximum allowable pressure drop. The pressure drop in the set-up with the original interpolation functions is $3.4597E-4$[dPa] for the coolant and $3.4460E-4$[dPa] for the to be cooled fluid. The pressure drop in the set-up with the alternative interpolation functions is $3.4946E-4$[dPa] for the coolant and $3.5001E-4$[dPa] for the to be cooled fluid. The maximum allowable pressure drop is identical in both optimization set-ups at $3.4653E-4$ [dPa]. There is a difference in the pressure drop values comparing the two optimization scenarios, but the pressure drop values are still in the same range. The optimal design generated with the alternative interpolation functions slightly violates the pressure drop constraints. However, this slightly higher pressure drop does not explain the large difference in heat exchanger performance. A reason for the difference in heat exchanger performance could be that the optimizer finds a local optimum with the set-up with the original interpolation functions. The gradient information is different due to the different non-mixing constraint used. It could be that in the initial phase of the optimization process a local optimum is found, which with the diminishing gradients due to the β increments can not be further improved to a global optimum. Based on these results only it is difficult to determine what the exact origin is of the large difference in final objective value and thermal efficiency. A variety of different optimization scenarios should be tried to determine if the difference in performance is consistent.

To check if the fluid flow is correctly penalized, the normalized velocity fields of both fluids are plotted. The velocity fields are evaluated at the white line in Fig. D.1a and D.1b. Fig. D.2a shows the plot of the normalized velocity fields generated with the original interpolation functions, the velocity fields are normalized with $1.95E-4$[m/s]. Fig. D.2b shows the plot of the normalized velocity fields generated with the alternative interpolation functions, the velocity fields are normalized with $2.2E-4$[m/s]. In both plots the normalized thermal conductivities are also plotted to show the solid material regions. The thermal conductivity is normalized with the thermal conductivity of the solid material 244[W/mK]. The optimal designs have small overlapping material regions. The overlapping material regions in the non-mixing region are relatively large compared to the total size of the non-mixing region. The reason for the relatively large overlapping regions is the small minimum wall-thickness. For a t_{min} value in the range of the filter radi size of R_1 and R_2, the region with intermediate values is relatively large compared to the total size of the non-mixing region when the wall-thickness approaches the minimum wall-thickness t_{min}. The size of the overlapping material regions can be reduced by further increasing the β values.

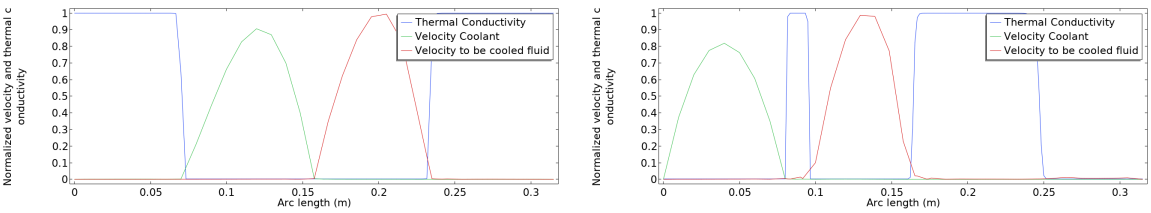

(a) Optimal design generated with the original interpolation functions.

(b) Optimal design generated with the alternative interpolation functions.

Figure D.2: Check of overlapping regions in the two sets of interpolation functions.

D.1.2. Two Different Fluids Optimization Results

Fig. D.3 shows the optimal results generated with the original and alternative interpolation functions in the two different fluids optimization scenario. The fields of the optimal design generated with the original interpolation functions are provided on the left-side in Fig. D.3 (Fig. D.3a, D.3c, D.3e and D.3g). The optimal result generated with the original interpolation functions shows a design with tortuous channels filling almost the entire design domain. The fluid channels are placed next to each other in the entire design domain without separation by a solid region. The objective and thermal efficiency value of the optimal design are $5.4590E6$[kg m K/s^3] and 32.519%. The fields of the optimal design generated with the alternative interpolation functions are provided on the right-side in Fig. D.3 (Fig. D.3b, D.3d, D.3f and D.3h). The non-mixing constraint prevents mixing of the two fluids with a non-mixing region that has an almost constant thickness. The non-mixing constraint is used in a similar manner as in the scenario with identical fluids and the alternative interpolation functions. To investigate the locally generated wall-thickness, three cross-sections of the non-mixing region are analysed. The local wall-thickness in the optimal design is evaluated in three locations, each location is marked in Fig. D.3b with a white line. The evaluated wall-thicknesses from left to right are ≈ 0.0166 [m], ≈ 0.0146 [m] and ≈ 0.0166 [m]. The evaluated wall thicknesses deviate slightly from the pre-set minimum wall-thickness of $t_{min} = 0.015$[m]. On average the wall-thickness seems to approach the t_{min} value. The design has to be sliced perpendicular to the centerline of the non-mixing region to accurately measure the wall-thickness. This operation is performed manually and could give slight deviations between the measured and actual wall-thickness. The remaining sections of the non-mixing region seem to have a wall-thickness with a similar size. The two optimal designs show more similarities compared to the optimal designs in the identical fluids scenario. Both set-ups generate tortuous channel shapes spread out over a large portion of the design domain. The objective and thermal efficiency value of the optimal design are 5.9631E6 [kg m K/s^3] and 36.794%.

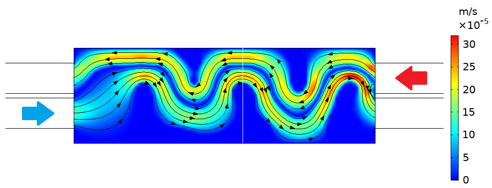

(a) Velocity field.

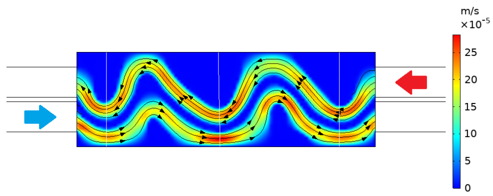

(b) Velocity field.

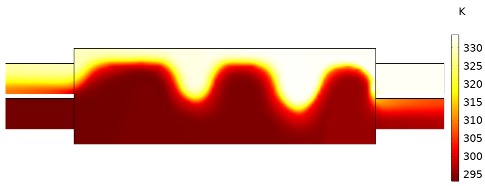

(c) Temperature field, with an objective value of 5.4590E6 [kg m K/s^3] and a thermal efficiency value of 32.519%.

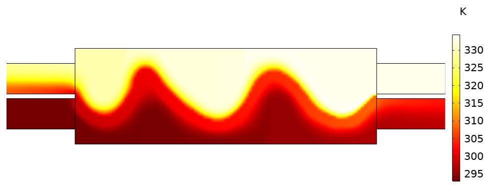

(d) Temperature field, with an objective value of 5.9631E6 [kg m K/s^3] and a thermal efficiency value of 36.794%.

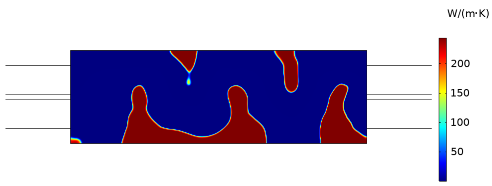

(e) Thermal conductivity field.

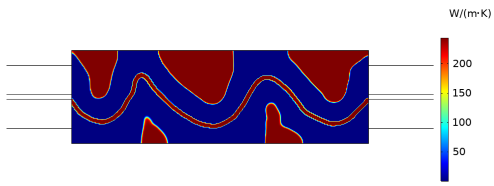

(f) Thermal conductivity field.

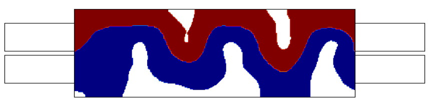

(g) Fluid regions.

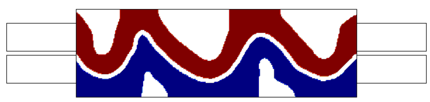

(h) Fluid regions.

Figure D.3: Optimal results generated with the original and alternative set of interpolation functions in the identical fluids scenario. The optimal results generated with the original set is provided on the left-side, while the optimal result generated with the alternative set is provided on the right-side.

Similar to the identical fluids scenario, the velocity magnitude is evaluated on the white lines as shown in Fig. D.3a and D.3b (the velocity magnitude is evaluated at the first white line). Fig. D.4 shows the normalized velocity magnitude in the optimal designs generated with each set of interpolation functions. Fig. D.4a shows the plot of the normalized velocity fields generated with the original interpolation functions, the velocity fields are normalized with $2.45E-4$[m/s]. Fig. D.4b shows the plot of the normalized velocity fields generated with the alternative interpolation functions, the velocity fields are normalized with $2.27E-4$[m/s]. In the results generated with the original interpolation functions the overlapping regions are visible in the solid regions and between the fluids. In the results generated with the alternative interpolation functions, the overlapping regions are visible in the solid material regions including the non-mixing region. The same holds here as in the identical fluids scenario, further increasing the β values will reduce the size of the overlapping regions.

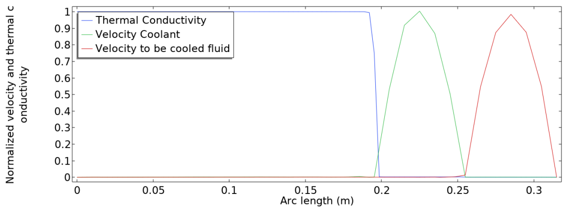

(a) Optimal design generated with the original interpolation functions.

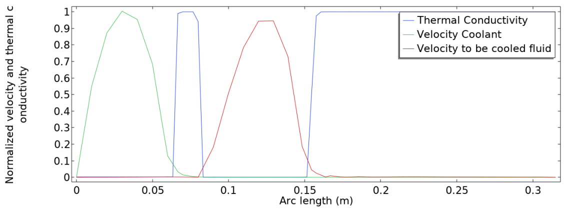

(b) Optimal design generated with the alternative interpolation functions.

Figure D.4: Check of overlapping regions in the two sets of interpolation functions.

In both the identical and different fluids scenario a significant difference in heat exchanger performance is seen comparing the optimal results generated with the original and the alternative interpolation functions. An explanation for the difference in heat exchanger performance could be that in the set-up with the original interpolation functions, the gradient information is favourable for a design with thinner fluid channels. The set-up with the alternative interpolation functions has different gradient information, since the non-mixing constraint does not allow a distance between the channels smaller than the minimum wall-thickness. The optimizer can in such a scenario further improve the design by folding the fluid channels.

E

Post Processing of Optimal Design and 3D-printing

In this appendix the 3D design generated in Section 7.1 is post-processed to create a mesh-file that can be prepared for 3D-printing. Two different printing methods are used to manufacture the 3D design. The first printing method used is fused deposition modeling (FDM) and the second printing method used is Selective Laser Melting (SLM). Each printing method required a different mesh-file preparation process. In the first section a general approach is provided to create a mesh-file from a point cloud. This general approach is used to create the mesh-file used in the FDM-process. The FDM-print is provided in the second section. The slicing software used to prepare the file for SLM required a smoother mesh-file and a different approach is used to create the mesh used in the SLM-process. Both the approach used to create the mesh-file and the SLM-print are provided in the third section.

E.1. Post-Processing

The first step towards creating a mesh-file that represents the solid regions of the heat exchanger is exporting the thermal conductivity datafield in the form of a table with coordinates and the corresponding thermal conductivity value. The smaller the distance between the coordinates, the more accurate the geometry is represented. Since the design domain does not have a solid material region enclosing (enclosure) the entire design domain, this solid material enclosure is generated separately. The enclosure datafield is also exported in the form of coordinates with corresponding thermal conductivity values. Both tables with coordinates are imported into MATLAB for filtering of the datasets. In MATLAB the cells in the tables defined as the fluid cells are filtered out of the dataset. Fig. E.1 shows a plot of the pointclouds representing the solid regions of the enclosure dataset and the optimization dataset. The pointcloud of the solid enclosure (Fig. E.1a) is dense and therefore looks like a solid block of material. The figure is provided here to show the overall shape of the solid enclosure.

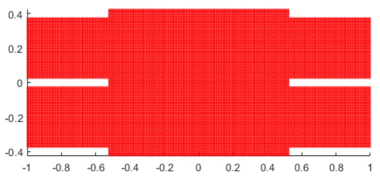

(a) Pointcloud representing the solid region of the enclsoure.

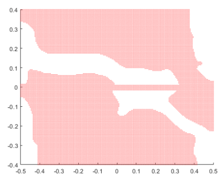

(b) pointcloud representing the solid region in the optimizationd domain.

Figure E.1: The two pointclouds used to form a solid region that represents the heat exchagner design.

In the next step the two solid regions are combined to form the total solid region. To show that the non-mixing constraint generates a variable wall-thickness, two pointclouds are generated. The first one is the total solid region and the second one is only the bottom half. To generate a boundary surface enclosing the two pointcloud sets the MATLAB boundary function is used. Fig. E.2 shows the boundary surfaces generated from

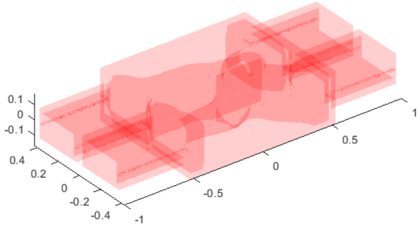

(a) Boudary surface first point cloud, complete heat exchanger.

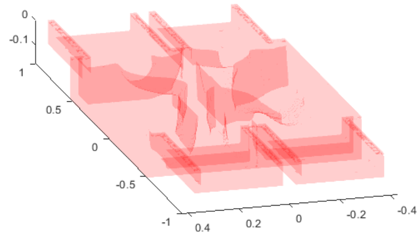

(b) Boudary surface second point cloud, bottom half heat exchanger.

Figure E.2: Plots of the two boundary surfaces created from the pointclouds.

each pointcloud. To create a surface mesh from the pointclouds the points used to generate the boundary surface are extracted. The coordinates of the extracted datapoints are exported in the form of a table (.txt file format used here). Fig. E.3 shows the datapoints used to form the boundary surfaces.

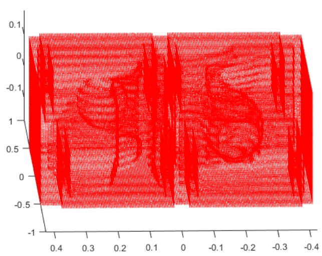

(a) Points represeting the boundary surface of the first mesh.

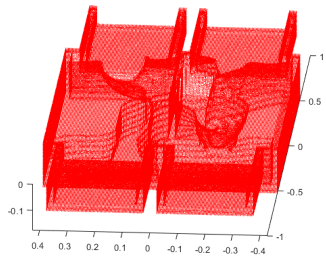

(b) Points represeting the boundary surface of the second mesh.

Figure E.3: Plots of the points representing the boundary surfaces.

To be able to generate a mesh from the datapoints representing the solid material region, the table with the coordinates is imported into Rhinoceros 7 (Rhino). In Rhino the coordinates in the table are again transformed to a pointcloud that can be manually manipulated. The redundent points in each pointcloud are removed to prevent the creation of a surface with a lot of noise. The remaining points used to form the mesh are provided in Fig. E.4. The size of the pointcloud can be scaled to the desired size and the pointcloud can be exported as a mesh format (.ply is used here).

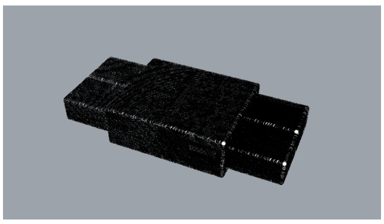

(a) Final pointcloud used for the first mesh.

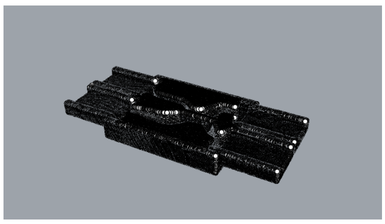

(b) Final pointcloud used for the second mesh.

Figure E.4: Pointclouds used for the creation of the mesh-files.

To generate a mesh surface from the pointclouds the ply-files are imported into Meshlab. In Meshlab the mesh surface is created with a ball pivoting filter. The filter radius is set to the distance of the nearest points in the pointcloud. To prevent the generation of large regions with inverted surfaces, sections of each pointcloud are imported and meshed separately. Even though the normal of the surfaces is consistent in most of the regions, some regions with flipped surfaces remained. Fig. E.5 shows the complete mesh of the first and the second part. Since the pivoting ball radius is selected small, the mesh still contains holes. The reason for selecting a small filter radius is to prevent the forming of degenerate surfaces. The separate meshed regions are combined in a single file and exported as a stl-file.

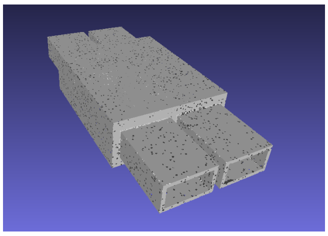

(a) Meshed surface part 1.

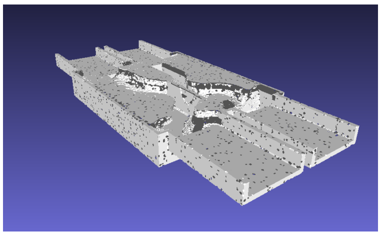

(b) Meshed surface part 2.

Figure E.5: Meshes created from filtered pointclouds.

To patch all the holes in the mesh and merge the open boundaries Netfabb Studio is used. Fig. E.6 shows the patched mesh files. The meshes here are patched ignoring the normal direction of the surfaces, therefore some regions in the closed mesh have inverted surfaces. Within Netfabb Studio the normal direction can be altered to make the mesh surfaces coherent, but in this mesh the surfaces have to be inverted manually. The inverted surfaces in the mesh-files were not manually inverted to form a coherent mesh surface, since this was not required to use these mesh-files for printing with FDM.

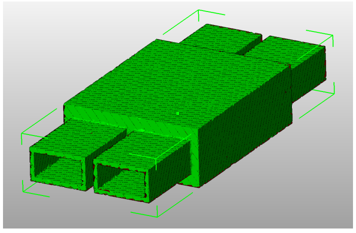

(a) Closed mesh surface part 1.

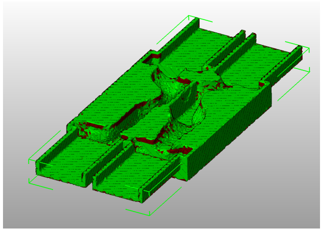

(b) Closed mesh surface part 2.

Figure E.6: Patched mesh surfaces to form a single closed mesh for each part.

A risk with generating a mesh from a pointcloud is that the mesh could become coarse for a low density pointcloud. To increase the surface quality of such a coarse mesh, a smoothing filter can be used (HC Laplacian smoothing filter used here). To reduce the file-size the number of surfaces used in the mesh surface can be reduced with a simplification filter (Quadric edge collapse decimation filter used here). The smoothing and simplifcation filters are applied in Meshlab. Fig. E.7 provides the final stl-files loaded into Cura to show that the files can be processed within a 3D-printing environment for manufacturing. The inverted surfaces did not give problems within the Cura environment to form a printing file (.gcode).

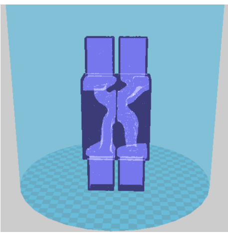

(a) Final mesh-file part 1 (X-Ray view).

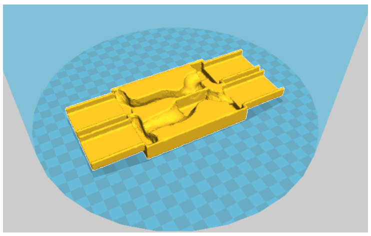

(b) Final mesh-file part 2.

Figure E.7: Final mesh-files loaded into the Cura 3D-printing environment.

E.2. FDM-Printing

To show that the created mesh-files can actually be manufactured, part 2 is 3D-printed with a FDM-printer. Part 2 is here selected because it clearly visualizes the variable wall-thickness created with the non-mixing constraint. The printing file is prepared in Cura, printed with a FDM printer from ANYCUBIC and the printing material used is PLA. Fig. E.8 provides two images of the 3D-printed part showing the bottom half of the optimal 3D design. The size of the printed part is approximately 120x51x10 [mm].

(a) First image of 3D-printed part.

(b) Second image of 3D-printed part.

Figure E.8: Images of the 3D-printed part showing the variable wall-thickness in the bottom half of the 3D heat exchanger design.

E.3. SLM-Printing

To prepare a mesh-file for SLM a software package is used that can slice the mesh-file and add support material where needed. The mesh-files created in Section E.1) could not be sliced in this software package, likely due too much noise in the mesh-file. Noise in the mesh-files could for example be double triangles, inverted triangles or open boundaries. To improve the surface quality of the mesh-file, a different approach is used to create a mesh from a pointcloud. The pointcloud provided in Fig. E.4a is manually filtered to remove the points that form the outer boundary of the heat exchanger. Fig. E.9 shows the remaining points that form the inner boundary of the heat exchanger. All operations to form the mesh surface are performed in Rhino.

(a) Side view filtered point cloud.

(b) Perspective view filtered point cloud.

Figure E.9: Points used to create an improved mesh surface.

The filtered pointcloud is used to create closed curves from sections of points within a layer. The curves are fitted through the points in the pointcloud. Fig. E.10 shows the curves used to form the inner surface of the heat exchanger. To form each closed curve, the double points in each layer are manually removed. Not all points are used to create closed curves, some of the layers with points are removed.

(a) Side view of all closed curves.

(b) Perspective view of all closed curves.

Figure E.10: Closed curves used to form the inner surface of the heat exchanger.

By forming a lofted polysurface between each closed curve, the inner surface of the heat exchanger can be created. The outer surface of the heat exchanger consists of multiple rectangular polysurfaces that are created separately. Creating the outer surface from rectangular surfaces instead of using the points in the pointcloud prevents noise in the outer surface of the heat exchanger. The inner surface of the heat exchanger is shown in Fig. E.11a, while the outer surface is shown in Fig. E.11b.

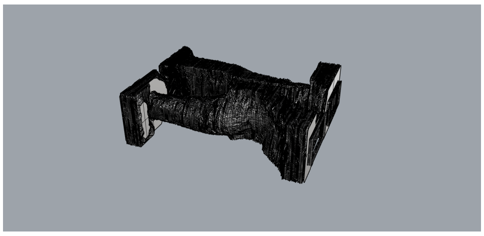

(a) Inner polysurface heat exchanger.

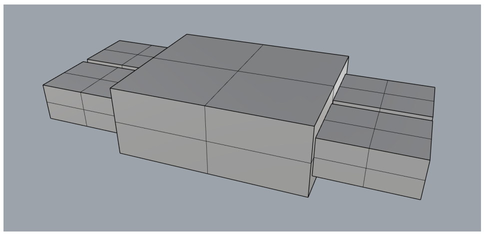

(b) Outer polysurface heat exchanger.

Figure E.11: Polysurfaces used to create the boundaries of the heat exchanger.

Each polysurface is meshed to form the meshed surface of the heat exchanger. The meshed inner surface is shown in Fig. E.12a and the meshed outer surface is shown in Fig. E.12b.

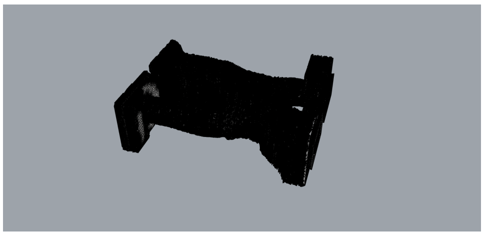

(a) Inner mesh surface heat exchanger.

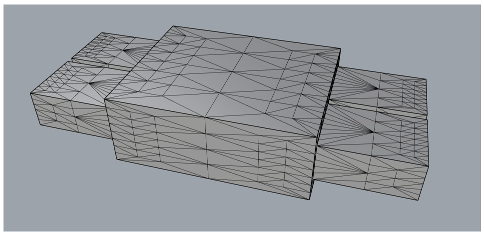

(b) Outer mesh surface heat exchanger.

Figure E.12: Mesh surfaces used to create the boundaries of the heat exchanger.

The meshed surfaces are exported in a single mesh-file (.stl). The mesh-file is imported into Netfabb Studio to stitch the open boundaries and patch the remaining holes. One of the drawbacks of this approach is that the complete mesh surface created from multiple lofted surfaces can have a sharp transition between the patched mesh surfaces. A smoother overall mesh shape is created with Meshmixer. The patched mesh-file is imported into Meshmixer, where different sculpting brushes are used to even out the mesh surface. Fig. E.13 shows the stitched, patched and smoothed mesh surface. In a similar manner as in Section E.1 Meshlab is used to reduce the size of the mesh-file.

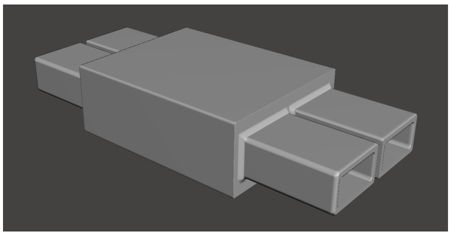

(a) Smoothed mesh surface view 1.

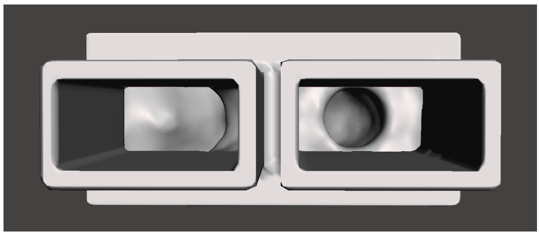

(b) Smoothed mesh surface view 2.

Figure E.13: Stitched, patched and smoothed mesh surface.

The simplified mesh-file was prepared by Blue Ocean Spine for SLM. Blue Ocean Spine printed the mesh-file twice. The size of both prints is identical and approximately $62x26x12$ [mm]. The first print was provided with the support material removed as shown in Fig. E.14.

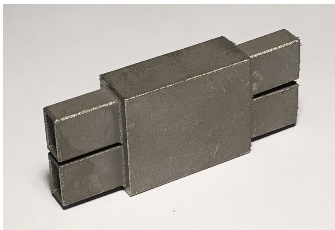

(a) Perspective view first print.

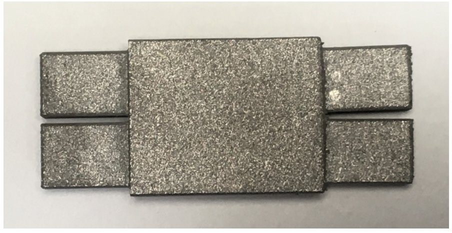

(b) Side view first print.

Figure E.14: First print manufactured by Blue Ocean Spine.

The second print still had the support material attached to the print. In the SLM-process a new material layer is deposited on top of each previously deposited material layer. After each new material layer is deposited, lasers are used to melt the material within each layer to the previously deposited material layer. The print direction in the SLM-process is in the vertical direction. The support material indicates that the prints were printed standing up, from left to right as shown in Fig. E.15b. To show that the internal geometry of the print matches the design generated with topology optimization, a milling machine was used to remove the top layer of the print. The milling process is shown in Fig. E.15c and the internal structure of the bottom half is shown in Fig. E.15d.

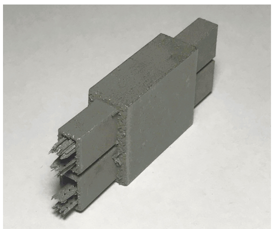

(a) Perspective view second print.

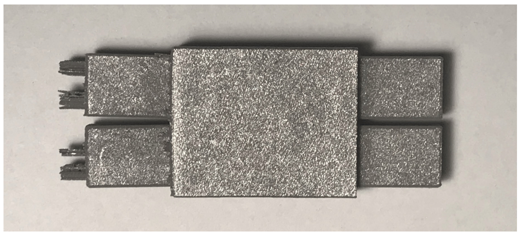

(b) Side view first print.

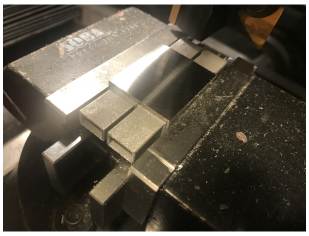

(c) Milling process, where the top layer of the print is removed.

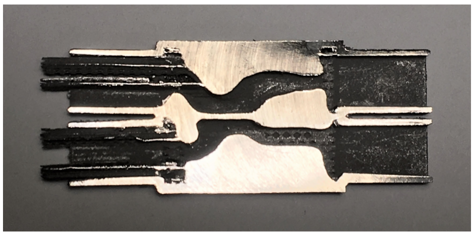

(d) Top view of the Bottom half of the second print.

Figure E.15: Second print manufactured by Blue Ocean Spine.

Bibliography

[1] CES EduPack 2019. Database: Level 3, . Accessed: 12-05-2022.

[2] CES EduPack 2019. Aluminium, commercial purity, 1-0, . Accessed: 06-05-2022.

[3] M.P. Bendsøe. Optimal shape design as a material distribution problem. *Structural optimization*, 1(4): 193–202, 1989. https://doi.org/10.1007/BF01650949.

[4] T. Borrvall and J. Petersson. Topology optimization of fluids in stokes flow. *International journal for numerical methods in fluids*, 41(1):77–107, 2003. https://doi.org/10.1002/fld.4265.

[5] A. Clausen, N. Aage, and O. Sigmund. Topology optimization of coated structures and material interface problems. *Computer Methods in Applied Mechanics and Engineering*, 290:524–541, 2015. https://doi.org/10.1016/j.cma.2015.02.011.

[6] E.M. Dede. Multiphysics topology optimization of heat transfer and fluid flow systems. In *proceedings of the COMSOL Users Conference*, 2009. https://www.comsol.dk/paper/download/44388/Dede.pdf.

[7] F. Feppon. Shape and topology optimization applied to compact heat exchangers. 2021. https://hal.archives-ouvertes.fr/hal-03207863.

[8] F. Feppon, G. Allaire, C. Dapogny, and P. Jolivet. Body-fitted topology optimization of 2d and 3d fluid-to-fluid heat exchangers. *Computer Methods in Applied Mechanics and Engineering*, 376:113–638, 2021. https://doi.org/10.1016/j.cma.2020.113638.

[9] J.H.K. Haertel. Design of thermal systems using topology optimization. 2018. https://orbit.dtu.dk/en/publications/design-of-thermal-systems-using-topology-optimization.

[10] L.C. Høghøj, D.R. Nørhave, J. Alexandersen, O. Sigmund, and C.S. Andreasen. Topology optimization of two fluid heat exchangers. *International Journal of Heat and Mass Transfer*, 163:120–543, 2020. https://doi.org/10.1016/j.ijheatmasstransfer.2020.120543.

[11] H. Kobayashi, K. Yaji, S. Yamasaki, and K. Fujita. Topology design of two-fluid heat exchange. *Structural and Multidisciplinary Optimization*, 63(2):821–834, 2021. https://doi.org/10.1007/s00158-020-02736-8.

[12] B.S. Lazarov and O. Sigmund. Filters in topology optimization based on helmholtz-type differential equations. *International Journal for Numerical Methods in Engineering*, 86(6):765–781, 2011. https://doi.org/10.1002/nme.3072.

[13] K. Maute and O. Sigmund. Topology optimization approaches: A comparative review. *Structural and Multidisciplinary Optimization*, 6, 2013. https://doi.org/10.1007/s00158-013-0978-6.

[14] P. Papazoglou. Topology optimization of heat exchangers. 2015. http://resolver.tudelft.nl/uuid:08481ec6-d6df-4162-b254-8b99eeccc6d1.

[15] K.R. Saviers, R. Ranjan, and R. Mahmoudi. Design and validation of topology optimized heat exchangers. In *AIAA Scitech 2019 forum*, page 1465, 2019. https://doi.org/10.2514/6.2019-1465.

[16] IF Solutions. Types of heat exchangers in oil and gas applications: How heat exchangers work. https://ifsolutions.com/types-of-heat-exchangers-in-oil-gas-applications-how-heat-exchangers-work/. Accessed: 23-11-2021.

[17] 3D Systems. Laserform ti gr23 (a). https://www.3dsystems.com/sites/default/files/2021-09/3d-systems-laserform-ti-gr23%28a%29-datasheet-us-a4-2021-09-20-a-print_0.pdf. Accessed: 15-08-2022.

[18] R. Tawk, B. Ghannam, and M. Nemer. Topology optimization of heat and mass transfer problems in two fluids—one solid domains. *Numerical Heat Transfer, Part B: Fundamentals*, 76(3):130–151, 2019. https://doi.org/10.1080/10407790.2019.1644919.

[19] Thermexcel. Physical characteristics of water (at the atmospheric pressure). https://www.thermexcel.com/english/tables/eau_atm.html. Accessed: 06-05-2022.

[20] Engineering ToolBox. Sae multigrade oils - viscosities and densities. https://www.engineeringtoolbox.com/sae-grade-oil-d_1208.html, . Accessed: 03-05-2022.

[21] Engineering ToolBox. Water - density, specific weight and thermal expansion coefficients. https://www.engineeringtoolbox.com/water-density-specific-weight-d_595.html, . Accessed: 03-05-2022.

[22] Engineering ToolBox. Motor oils - dynamic viscosities. https://www.engineeringtoolbox.com/dynamic-viscosity-motor-oils-d_1759.html, . Accessed: 03-05-2022.

[23] Engineering ToolBox. Water - dynamic (absolute) and kinematic viscosity vs. temperature and pressure. https://www.engineeringtoolbox.com/water-dynamic-kinematic-viscosity-d_596.html, . Accessed: 03-05-2022.

[24] Engineering ToolBox. Water - specific heat vs. temperature. https://www.engineeringtoolbox.com/specific-heat-capacity-water-d_660.html, . Accessed: 03-05-2022.

[25] Engineering ToolBox. Gases - ratios of specific heat. https://www.engineeringtoolbox.com/specific-heat-ratio-d_608.html, . Accessed: 18-02-2022.

[26] Joseph Ugochukwu, Chigbo Nwamaka, Anyadiegwu Chukwunweike Faustinus, and Olinya Christopher. Determination of the specific heat capacity of different sae 20w-50 engine oil samples using the electrical method. *JAP*, 8:33–35, 2016.

[27] F. Wang, B.S. Lazarov, and O. Sigmund. On projection methods, convergence and robust formulations in topology optimization. *Structural and Multidisciplinary Optimization*, 43(6):767–784, 2011. https://doi.org/10.1007/s00158-010-0602-y.

[28] Liu Yang, Mao Mao, Jia-nan Huang, and Weikai Ji. Enhancing the thermal conductivity of sae 50 engine oil by adding zinc oxide nano-powder: an experimental study. *Powder Technology*, 356:335–341, 2019.

[29] C. Zillober. A globally convergent version of the method of moving asymptotes. *Structural optimization*, 6(3):166–174, 1993. https://doi.org/10.1007/BF01743509.